University of Miami
Scholarly Repository

Open Access Dissertations | Electronic Theses and Dissertations

2016-06-17

Plasmon Field Effect Transistor: A Novel Sensing Platform for Biomedical Applications

Hossein Shokri Kojori
University of Miami, hoshoko@gmail.com

Follow this and additional works at: https://scholarlyrepository.miami.edu/oa_dissertations

Recommended Citation
Shokri Kojori, Hossein, "Plasmon Field Effect Transistor: A Novel Sensing Platform for Biomedical Applications" (2016). *Open Access Dissertations*. 1678.
https://scholarlyrepository.miami.edu/oa_dissertations/1678

This Open access is brought to you for free and open access by the Electronic Theses and Dissertations at Scholarly Repository. It has been accepted for inclusion in Open Access Dissertations by an authorized administrator of Scholarly Repository. For more information, please contact repository.library@miami.edu.

UNIVERSITY OF MIAMI

PLASMON FIELD EFFECT TRANSISTOR: A NOVEL SENSING PLATFORM FOR BIOMEDICAL APPLICATIONS

By

Hossein Shokri Kojori

A DISSERTATION

Submitted to the Faculty
of the University of Miami
in partial fulfillment of the requirements for
the degree of Doctor of Philosophy

Coral Gables, Florida

August 2016

©2016

Hossein Shokri Kojori

All Rights Reserved

UNIVERSITY OF MIAMI

A dissertation submitted in partial fulfillment of
the requirements for the degree of
Doctor of Philosophy

PLASMON FIELD EFFECT TRANSISTOR: A NOVEL SENSING PLATFORM FOR BIOMEDICAL APPLICATIONS

Hossein Shokri Kojori

Approved:

Sung Jin Kim, Ph.D.
Assistant Professor of
Electrical and Computer Engineering

Onur Tigli, D.Sc.
Assistant Professor of
Electrical and Computer Engineering

Michael R. Wang, Ph.D.
Professor of
Electrical and Computer Engineering

Ram Datar, Ph.D.
Associate Professor of
Pathology

Ashutosh Agarwal, Ph.D.
Assistant Professor of
Biomedical Engineering

Guillermo Prado, Ph.D.
Dean of the Graduate School

SHOKRI KOJORI, HOSSEIN (Ph.D., Electrical and Computer Engineering)
Plasmon Field Effect Transistor:
a Novel Sensing Platform for Biomedical Applications (August 2016)

Abstract of a dissertation at the University of Miami.

Dissertation supervised by Professor Sung Jin Kim.
No. of pages in text. (153)

The interest in plasmons, associated with nanostructured metals, has remarkably increased in the past decade. A Recent improvement in fabrication techniques to create well-controlled nanostructures also contributed to the rapid development of plasmonic applications, such as meta-materials, nonlinear optics, photovoltaic devices, biomedical sensors, medical therapies and spectroscopy. The surface plasmon resonance (SPR) sensor is one of the successful applications, which is widely used in biomedical research. On the other hand, localized surface plasmon resonance (LSPR) is also widely studied in a broad range of applications. The distinct property of LSPR is a tailored and sharp absorption/scattering peaks depending on the shape and sizes of the metal nanostructures. In addition, plasmonics can enable integration of high speed optical circuit by taking the advantages from the current electronics and optics technologies. Thus, plasmonics is considered as a solution for the next generation systems that offers ultra-high speed data processing. In this dissertation, we will introduce a novel plasmon field effect transistor (FET) that enables direct detection and efficient amplification of plasmon energy. This FET has several advantages such as electrical isolation of plasmon absorber nanostructures from a sensing and drug screening. Currently, we have proof of concept for the antigen-antibody bonding using the plasmon field effect transistor. We will develop a multiplexing capable plasmon FET sensing platform by integrating an array of plasmon FETs with microfluidic channels to detect cancer biomarkers.

To my loving Parents

And

My brothers

ACKNOWLEDGEMENTS

I would like to thank all the people who have contributed to this work. I wish to express my gratitude to my advisor Professor Sung Jin Kim for his scientific guidance and encouragement throughout my Ph.D. program. I appreciate his efforts to teach me how to think in a scientific way and how to solve technical problems. And I'm grateful for giving me the idea of this work and helping me in every single step of this project.

I also would like to thank Professor Wang, Tigli, Agarwal and Datar for serving on my Ph.D. dissertation committee and for their valuable comments and suggestions.

I would also like to thank Dr. Juhyung Yun who kindly taught me the fabrication techniques and helped me with writing papers.

I also would like to thank Dr. Siddarth Rawal, Dr. Jaeson Lee for their suggestions for my research and advice when I co-worked with them.

I would also like to thank all the lab members, Young Hun Paik, Hui Lu, Kai Shen, Dr. Guo Min Jiang and Dr. Behzad Dogahe for their help over the years.

Table of Contents

List of Tables

List of Figures

Chapter 1

Introduction

Plasmonics is a fascinating new area that has recently emerged. It exploits the unique optical interaction between light and metallic nanostructures to enable manipulation of light propagation. The unique properties of plasmonics realize the light wave from the free space to be confined to an ultra-small object, noble metal nanostructures [1-3]. This is an extreme advantage since light can be focused on the nanometer range which is beyond the light diffraction limit [4]. The basic physics of plasmonics is a coupling of the light wave with free electrons in the metal [5, 6]. Since this light-electron coupling creates an oscillation of free electrons in the metal surface, it is called as surface plasmon resonance (SPR) or surface plasmon polariton (SPP) [7]. Especially, if the plasmonic coupling occurs in a confined 0-dimensional structure (e.g. nanoparticles), it is called as localized surface plasmon resonance (LSPR). This coupling of light is a conversion and a transformation of energy between the incoming light and electrons, and it opens a variety of applications in different areas such as nonlinear optics, optical imaging and sensing [8-10]. Also, recent improvements of fabrication techniques to create well-controlled nanostructures contributed to plasmonic applications such as solar cells, light emitting diodes and photo-detectors [11-15]. The idea of enhancement comes from generating of plasmon waves around the active region of solar cells, light emitting diodes and photo-detectors while scattering has to be considered to improvement [16-19]. Besides these typical opto-electronic applications, many bio-related applications such as imaging or sensing/detection could benefit from plasmon resonance effect. Surface plasmon resonance sensor is one of a successful application that used in biomedical researches. For example, GE's Biacore has

been widely used to study the binding interactions of molecules. And this SPR based sensing technology offers extreme sensitives and robust operation. On the other hand, localized surface plasmon resonance is mostly used in broad range applications because of its capability of the tunable spectrum. Based on the size, shape, composition and local dielectric environment of nanoparticles, LSPR shows tailored and sharp absorption spectrum. Moreover, LSPR shows stable optical property under temperature fluctuations which make LSPR a better candidate for specific applications such as biosensors and nanoscale spectroscopy in compare with SPR.

In this chapter, we will first introduce some of the main applications using plasmonics. Then we will discuss the problem that we are going to solve in this dissertation will be defined as well as our proposed solution with a brief literature review on the current research status of LSPR and SPR sensors.

Plasmonic applications

Surface plasmon could offer different applications. Due to the concept of interaction of light and metal structures, many applications could benefit from plasmonic. Photonic integrated circuit (PIC) could be accomplished using plasmonic structures as shown in Figure (1.1a). In this figure, the ring resonator structure was implemented by plasmonic waveguides smaller than silicon based ones. Since the light can interact with metal in Nano range, the size of PIC could be reduced by a large factor than conventional PIC [20-22]. Figure (1.2b) shows an example of nanoantennas using surface plasmon resonance (SPR).

In this figure by changing the geometry of antennas, the frequency response of the system can be tuned.

(a)

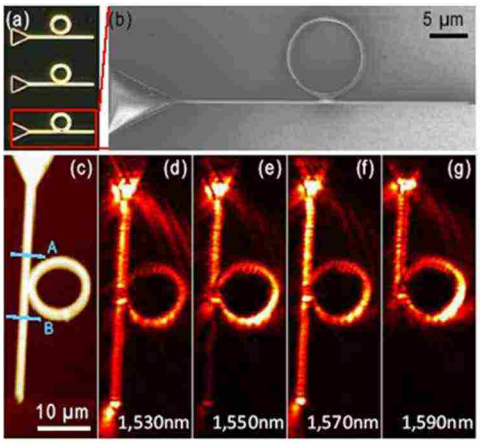

(b)

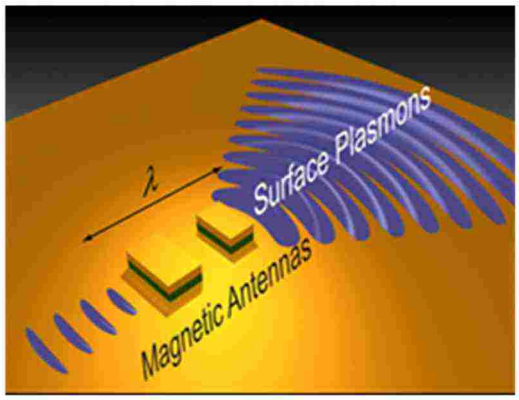

Figure 1.1 a) ring resonator structure using plasmonic structures. Reprinted with permission from [3]. Copyright (2009) Applied Physics Letters. b) nanoantennas for VIS-IR ranger using surface plasmon resonance. Reprinted with permission from [4]. Copyright (2012) American Chemical Society.

Another interesting application of plasmonic is in photovoltaic devices (PVs) [8-10, 12, 13, 23]. Using nanosize metal particles in the structure of PV devices helps to enhance the efficiency of PV devices because the metal nanoparticles improve absorption of photons in a specific wavelength and as a result more carriers will be generated in PV system which improves the total efficiency. Figure (1.2) shows this concept.

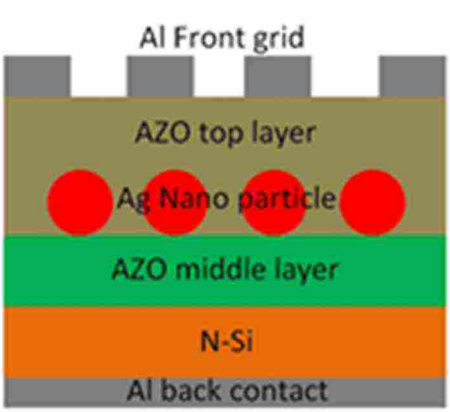

Figure 1.2 increasing of energy harvesting using the metal nanoparticles inside PV devices. In this picture the silver NPs are embedded inside the ZnO layer and light is illuminated from top aluminum grids.

Finally plasmonic holds a great potential for bio-sensing applications [7, 24-26]. It offers the highest sensitivity among other sensing mechanisms for biomarkers detection. Figure (1.3) shows a SPR sensor which could detect the binding of antigen-antibody which is important in cancer detection and disease diagnoses. In the sensing structure shown in the figure below, a fluidic channel brings a solution on top of the active area of the sensor. If any biomarker inside the solution attaches to the ligands then there will be a slight change in the angle of reflection which indicates the binding effect.

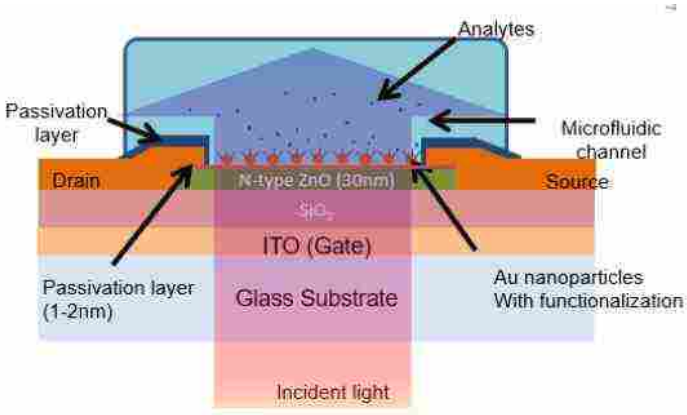

Figure 1.3 bio-sensing platform using plasmonic effects.

Problem definition and research objective

Many LSPR sensors have been reported so far for different applications in biology [3, 5, 25-29]. Gold nanoparticles (NPs) are used as a source of plasma excitation. Since depending on the shape, size and surrounding refractive index, various absorption spectrums could be extracted from gold NPs, many researchers have got this motivation to employ LSPR sensor for their sensing applications. However, the current LSPR sensors rely on optical instruments for their read-out system which is an important disadvantage. This disadvantage would not allow these LSPR sensors to be capable of integration on very small chips. Moreover, due to using optical instruments, the complexity of the overall system is high which makes the cost of utilizing of these sensors high in comparison with other available technologies. On the other hand, Schottky junction based devices for LSPR detection offer simple electrical signal read-out system due to their energy conversion mechanism. As a result, they have a high capacity of integration and multiplexing. However, as we mentioned before, there are two significant issues with these sensors. First, the low conversion efficiency of LSPR energy into generated photocurrent decreases the sensitivity of these kinds of detectors. Second, Schottky junction based devices use metal nanostructures as an electrode. It is a huge obstacle to the biological application where nanostructures have to be functionalized with different molecules and most likely they are to be used inside conductive liquids or buffers.

The objective of this project is to develop a novel sensing technology, which could efficiently detect and convert LSPR energy using Schottky based junction devices. Also to increase the sensitivity, the new device should be able to amplify the detected LSPR energy. The other criterion that has to be addressed is that the nanostructures have to be

electrically isolated. In this way, the nanostructures are capable of functionalization using many biological reagents. Therefore, this new device can be a valuable candidate for biomedical sensing applications.

Plasmon field effect transistor as a proposed solution

Figure (1.4) is our new proposed device to tackle the current issues mentioned in the previous section. Plasmon field effect transistor (pFET) consists of thin film transistor with a back gate and incorporated gold NPs on top of the transistor channel. ZnO, which is used as a transistor channel, is high band gap material which is transparent and also it does not have any overlapped optical response with Gold NPs. We claim that this device can efficiently detect and amplify the localized surface plasmon. Moreover, the nanostructures on top of the transistor channel are electrically isolated from drain, source and gate electrodes. Also, the proposed device has a high capacity of integration on semiconductor chips.

Plasmon field effect transistor benefits from Schottky junction based plasmon hot electron collection. In addition, electrically isolated LSPR absorber causes a higher stability and better signal-to-noise ratio along with availability to be used in liquids. Later in this dissertation, we will replace the ZnO layer with IGZO layer. Although both ZnO and IGZO are wide bandgap materials, IGZO offers more stability especially in bio-applications and in-situ experiments. Moreover, the plasmon FET device could be integrated with microfluidic channels, which makes this device a unique candidate for biomedical applications

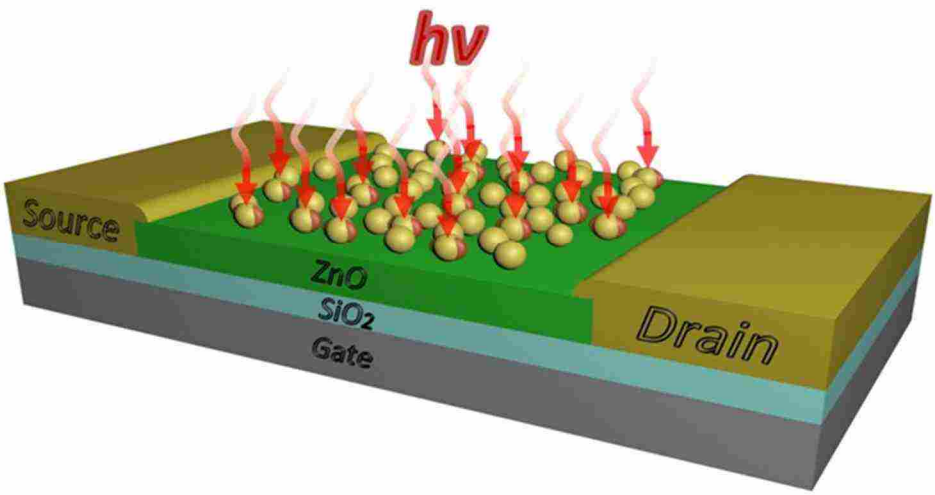

Figure 1.4 Illustration of Plasmon FET structure. The hV represents the incoming photon energy.

The plasmon FET will provide excellent thermal stability in its plasmonic absorption because the operating mechanism is free from the temperature dependent Fermi-Dirac function. And it is expected that the maximum operating speed will be limited by the switching speed of the FET device. Thus, we will investigate these properties by carrying out the proposed research. Another advantage of the proposed plasmon FET is the flexibility in the selection of the substrate. We will fabricate the pFET using InGaZnO or amorphous Si thin films on a Si substrate. This has a great advantage in terms of the integration capability with the existing CMOS technology and device scale-up capability. Finally, the plasmon FET uses a plasmonic nanostructure as an absorber (or antenna) and the absorption spectrum can be tailored by the nanostructure design and by using different materials.

Thesis organization

In this dissertation, we will explain the background theory and physics of surface and localized plasmon resonance in chapter 2. Also, different excitation techniques for plasmon surface plasmon resonance and the possible application will be explained. Then in chapter 3, the working principle of plasmon FET will be discussed. We will explain how induced plasmon hot electrons can enter the FET channel in creating current enhancement. The fabrication process of plasmon FET and gold nanoparticles are explained in chapter 4. In chapter 5, we analyze plasmon FET with conducting several experiments to show how efficient it can detect and amplify the plasmon resonance energy. Moreover, the sensitivity of plasmon FET to surrounding refractive index of gold nanoparticles will be demonstrated. Chapter 6 will present one the exciting application of plasmon FET as a bio-sensor. In this chapter the Plasmon FET is used to recognize the binding of a specific protein to carbohydrates linkers. Finally, the conclusion and future works will be exhibited in chapter 7.

Chapter 2

Introduction to surface plasmon resonance

Over decades, researchers in the optical field had been struggling to confine the optical signal to a smaller dimension [30]. Based on theory, the smallest achievable spot size of a focused monochromic light in an ideal condition is in the order of the wavelength. On the other hand, in electronics, the device sizes could be scale down to a couple of nanometers. Although photonic devices offer higher speed and bandwidth, the inability to scale down to the size of electronic devices is an important problem. Plasmonic is an ultimate solution for this problem because it brings the ability of manipulating light at nanoscale ranges. Plasmon resonance occurs based on the interaction of the electromagnetic field and electrons inside a metallic structure such as nano-particle or a thin film with nanometer scale. This interaction under specific conditions leads to generating of Plasmonic waves, an enhanced optical near field of sub-wavelength dimension With recent improvements in nanotechnology, plasmonic has got many attractions and offers many fascinating applications such as bio-sensors, photovoltaic devices and photonic circuits [30, 31].

There are two fundamental excitation methods for Plasmonic waves, which are called surface plasmons (SPs) and localized surface plasmon (LSPs). The SPs can be generated with a 2-dimensional thin metal plane that is connected with a dielectric material. The LSPs can also be generated with a 0-dimensional confined metal nanostructure. In both types of excitation methods, one of the key parameters for the plasmonic phenomenon is the dimension of the metallic object [31, 32]. In the case of the 2D metallic film based SPs, the thickness of the film should be around a couple of 10nm. Nano-range thickness of the

metallic thin film increases the coupling efficiency between incident electromagnetic field and free electrons inside metal film [33, 34]. The transferred energy creates an oscillation of the electrons, and this leads to generating plasmonic waves, known as surface plasmons (SPs) [31]. This surface plasmon generation needs a sophisticated optical geometry and specific dielectric constant condition to happen, and the details will be explained later in this chapter. This surface plasmon resonance has a wide range of applications such as a plasmonic waveguide, spectroscopy, sensing, metamaterials, imaging, and enhancement of emissive processes and nonlinearities [31-33, 35-40].

The other type of plasmonic excitation method, LSPs, requires the structure size in nanometer scale such as metal nanoparticles. These metal nanoparticles could be in different shapes, composition and sizes which produce different plasmon resonant frequencies, and these different structural properties enable different plasmonic absorption spectra [41-44]. Regarding optical instrumentation and excitation geometry, it is easier to generate localized plasmon resonance compared to surface plasmon resonance method [39].

In this chapter, the basic theory of plasmon waves will be explained. First, we will go over metal-optic interaction which explains the concept of plasmon waves. Then surface plasmon fundamentals, conditions, and applications will be covered. Finally, localized surface plasmon will be discussed to understand the differences of the LSPs over SPs.

Interaction of metal and electromagnetic waves

The interaction of metal and electromagnetic (EM) field can be explained by classical Maxwell's equations [31]. Depending on the frequency range (mostly from far infrared up to near visible range), metal can be approximated by the perfect conductor, and that means metal reflects most of the incident electromagnetic fields. However, with increasing the frequency, the EM field penetration increases significantly [45]. Finally, at ultra-high frequencies, metal can be considered as a dielectric, so it allows the electromagnetic field to propagate through metal. However depending on metal type such as Alkali or noble, this propagation can have different characteristics. Noble metals such as gold and silver show strong absorption due to transitions between electronic bands [46]. On the other hand, Alkali metals are transparent to ultraviolet frequencies since they have a free electron like band [30]. To describe this behavior, the complex dielectric function can be established (Ɛ(ω)). In general Ɛ(ω) can be written as [31]:

$$\varepsilon(\omega) = \varepsilon_1(\omega) + i\varepsilon_2(\omega) = \delta\varepsilon(\omega) + \frac{i\sigma'(\omega)}{\varepsilon_0\omega} \tag{2.1}$$

$$\sigma(\omega) = \sigma_1(\omega) + i\sigma_2(\omega) \tag{2.2}$$

Where σ is complex conductivity coefficient and, δε is static dielectric constant and ε_0 is permittivity of vacuum. Also, the complex refractive index can be defined as follow where k:

$$\tilde{n}(\omega) = n(\omega) + ik(\omega) \tag{2.3}$$

$$\tilde{n} = \sqrt{\varepsilon} \tag{2.4}$$

$$\varepsilon_1 = n^2 - k^2 \tag{2.5}$$

$$\varepsilon_2 = 2nk \tag{2.6}$$

$$n^2 = \frac{\varepsilon_1}{2} + 0.5\sqrt{\varepsilon_1^{\,2} + \varepsilon_2^{\,2}} \tag{2.7}$$

$$k = \frac{\varepsilon_2}{2n} \tag{2.8}$$

k is defined as the extinction coefficient and depends on the optical absorption of electromagnetic waves propagating through a medium. This dependence can be seen in following the equation [31]:

$$\alpha(\omega) = \frac{2k(\omega)\omega}{c} \tag{2.9}$$

Where, c is the speed of light in vacuum space (m/s). Considering above equations, the imaginary part of the dielectric function determines the absorption inside the medium. With this brief overview, we can now move on into Drude model that describes the optical properties of metal in frequency ranges lower than the threshold of transitions between electronic bands.

Drude model

The Drude model was introduced by Paul Drude in the 20th century after J.J. Thompson's discovery of the electron in 1897. It is an adequate model to describe the behavior of electrons inside metal structures. In this model, under a particular condition, the dielectric properties of metal can be seen as a free electron with a dielectric function of [31]:

$$\varepsilon(\omega) = 1 - \frac{\omega_p{}^2}{\omega^2 + i\omega\gamma} \tag{2.10}$$

Where, ω_p is the plasma frequency ($\omega_p = \sqrt{(ne^2/\varepsilon_0 m)}$), n is conduction electron density, e is an elementary charge, m is the electron mass. Here are the basic assumptions of Drude model [36]:

1- Collisions between electrons and ions are instantaneous and uncorrelated phenomenon
2- Electrons travel in straight lines between scattering with no interaction
3- In the time interval dt, the probability of an electron collision is dt/T where T is no related to position and momentum of the electron
4- After collision event for an electron, the electron has the temperature of the environment.

Plasma frequencies, ω_p are commonly in the range of visible light (i.e., ~ 10^{15}- 10^{16} Hz). In the Drude model, according to the above assumption, electron oscillation through applied electromagnetic field can be damped via collisions with the nucleus at a collision frequency $\gamma = 1/T$. At room temperature, the typical value of τ is on the order of 10^{-14} s, which results in $\gamma \sim 10^{14}$ Hz. The real and imaginary parts of $\varepsilon(\omega)$ can be expressed as [31]:

$$\varepsilon_R = 1 - \frac{\omega_p{}^2}{\omega^2 + \gamma^2} \tag{2.11}$$

$$\varepsilon_I = \frac{\omega_p{}^2 \gamma}{\omega(\omega^2 + \gamma^2)} \tag{2.12}$$

For the frequencies lower than ω_p, metals retain their metallic characteristics. However for optical frequencies $\omega >> \gamma$, we can approximate ε_R as $1-\omega_p^2/\omega^2$. Based on mentioned approximation ε_R is a negative value. The complex refractive index of metal can be expressed as following [31]:

$$n_R = \left[\frac{1}{2}\left(\sqrt{\varepsilon_R^2+\varepsilon_I^2}+\varepsilon_R\right)\right]^{0.5} \tag{2.13}$$

$$n_I = \left[\frac{1}{2}\left(\sqrt{\varepsilon_R^2+\varepsilon_I^2}-\varepsilon_R\right)\right]^{0.5} \tag{2.14}$$

The imaginary part of the refractive index is larger than the real part for $\omega < \omega_p$ As a result, the propagation of electromagnetic wave inside the metal structure is mostly absorptive which means the electric field decay exponentially. Skin depth is the distance that the amplitude of the electric field inside metal decreases by factor e^{-1}. Skin depth depends on the frequency as well as material and boundary condition. Following figure shows the real and imaginary part of ε (ω) of silver.

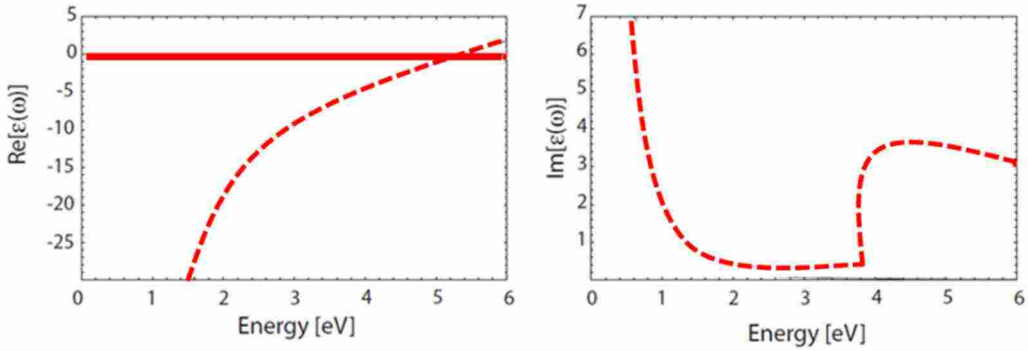

Figure 2.1 real and imaginary part of the dielectric function for silver (doted) and Drude model fitted.

Surface plasmon at metal/isolator interfaces

Plasmon is a collection of electrons that collectively oscillate in a conducting material such as metal. When electrons are displaced, the positive charge exerts an attractive force on the electrons and which leads to pulling them back to their original positions. These Coulomb interactions make the plasmons oscillate when they are excited. The Surface Plasmon is a propagation of the electromagnetic energy using the electron resonance at the interference of metal and dielectric. This propagation is confined in a perpendicular direction of interference. These surface waves excite via the coupling of the electromagnetic fields to oscillations of the metal's electron plasma [31]. Figure (2.2) shows a simple geometry for surface plasmon excitation which includes flat interference of metal Z<0 with the dielectric function of $\varepsilon_m(\omega)$ and non-absorbing dielectric at z>0 with positive real dielectric constant ε_d. Surface plasmon has p-wave like characteristics which means only TM mode can excite plasmon waves while there is no excitation mode for TE

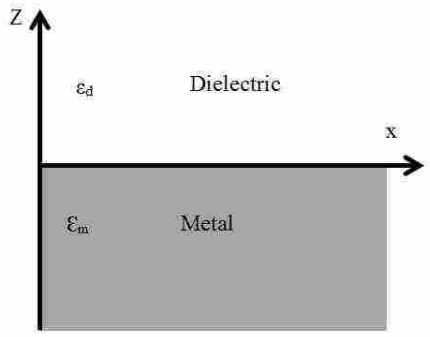

Figure 2.2 geometry of surface plasmon propagation with single interference of metal and dielectric.

polarization. In the figure (2.2), the electromagnetic field with a component normal to the surface of the metal creates charge density σ_s along the metal surface [31].

To get the better understanding of surface plasmon wave, we solve the wave equation based on the geometry shown in figure (2.2) [31].

$$\frac{\partial^2 E(z)}{\partial z^2} + \left(k_0{}^2 - \beta^2\right) E = 0 \tag{2.15}$$

Where E(Z) is the electric field along the Z direction, K_0 is wave vector and β is a propagation constant of traveling wave (ω/c). To determine the spatial field profile and dispersion of propagating waves, we have to separate different field components which are which are the electric field (E) and magnetic field (H). By using curl equations, for the propagation along-direction, the system equation could be simplified as [31]:

$$\frac{\partial E_y}{\partial z} = -i\omega\mu_0 H_x \tag{2.16}$$

$$\frac{\partial E_x}{\partial z} - i\beta E_z = -i\omega\mu_0 H_y \tag{2.17}$$

$$i\beta E_y = i\omega\mu_0 H_z \tag{2.18}$$

$$\frac{\partial H_x}{\partial z} - i\beta H_z = -i\omega\mu_0 E_y \tag{2.19}$$

$$i\beta H_y = i\omega\mu_0 E_z \tag{2.20}$$

Different polarization (TE or TM) properties allow this system to have two sets of solution. For TM mode the field component $E_{x,z}$ and H_y are nonzero. For TM mode we can rewrite the equations as follow:

$$E_x = -i\frac{1}{\omega\varepsilon_0\varepsilon}\frac{\partial H_y}{\partial z} \tag{2.21}$$

$$E_z = -\frac{\beta}{\omega\varepsilon_0\varepsilon}H_y \tag{2.22}$$

So the wave equation for TM mode can be defined as:

$$\frac{\partial^2 H_y}{\partial z^2} + \left(k_0{}^2\varepsilon - \beta^2\right)H_y = 0 \tag{2.23}$$

The solution for the above equation using equation (2.16-20) for Z>0 is as following equations:

$$H_y(z) = A_1 e^{i\beta x}e^{-k_2 z} \tag{2.24}$$

$$E_x(z) = -iA_1\frac{1}{\omega\varepsilon_0\varepsilon_1}k_1 e^{i\beta x}e^{k_1 z} \tag{2.25}$$

$$E_z = -A_1\frac{\beta}{\omega\varepsilon_0\varepsilon_1}e^{i\beta x}e^{k_1 z} \tag{2.26}$$

Where for $z < 0$, $k_i \equiv k_{z,i}$ $(i = 1, 2)$ is the component of the wave vector normal to the interface in metal and isolator media. Its reciprocal value, $Z = 1/|k_z|$, expresses the evanescent decay length of the fields normal to the interface, which means confinement of the wave. Based on the boundary condition at the interface:

$$\frac{k_2}{k_1} = -\frac{\varepsilon_2}{\varepsilon_1} \tag{2.27}$$

Also

$$\begin{aligned} k_1{}^2 &= \beta^2 - k_0{}^2 \varepsilon_1 \\ k_2{}^2 &= \beta^2 - k_0{}^2 \varepsilon_2 \end{aligned} \tag{2.28}$$

By combining equations (2.27) and (2.28), the dispersion relation of surface plasmon at interference can be described as following:

$$\beta = k_0 \sqrt{\frac{\varepsilon_1 \varepsilon_2}{\varepsilon_1 + \varepsilon_2}} \tag{2.29}$$

The dispersion relation of SPs along the interface between the dielectric medium ε_d and metal ε_m is shown in figure (2.3). For frequencies lower than $\frac{\omega_p}{\sqrt{1+\varepsilon_d}}$, the propagation of SPs bound to the surface, which called non-radiative evanescent surface waves. As frequency increases ($\omega > \omega p$) , wave vector along x, y-directions becomes real value so the surface plasmon radiate out of the surface, which is called radiative SPs [31].

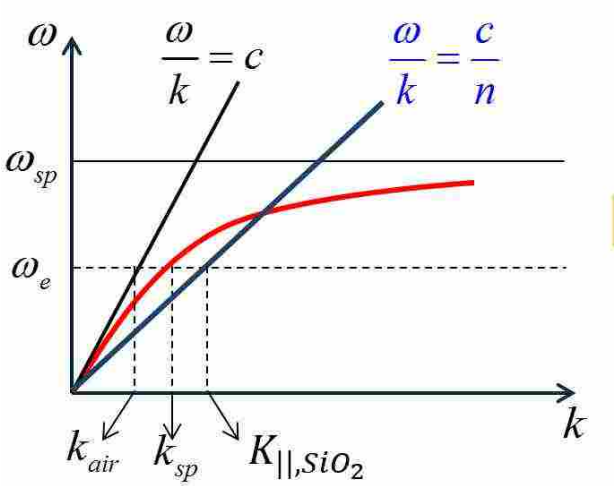

Figure 2.3 surface plasmon dispersion relation for single interference of metal and dielectric with ε_m and ε_d respectively.

Analysis of surface plasmon on metal/Di Electric surface

Since the dielectric constant of the metal is a complex number, the wave vector K is also complex number. As results, surface plasmon wave which propagates along interference of metal/dielectric exhibits a finite propagation length L given by [36, 47]:

$$L_{x=}1/2k_{xI} = \frac{c}{\omega}\left(\frac{\varepsilon_{mR}+\varepsilon_d}{\varepsilon_{mR}\varepsilon_d}\right)^{\frac{2}{3}}\frac{\varepsilon_{mR}{}^2}{\varepsilon_{mI}} \tag{2.30}$$

Where

$$\begin{aligned}\varepsilon_m &= \varepsilon_{mR}+\varepsilon_{mI}\\ k_x &= k_{xR}+k_{xI}\end{aligned} \tag{2.31}$$

Also, it is well known to calculate the depth of SPs penetration (skin depth) inside metal (δ_2) and dielectric (δ_1) which leads to following equations [47]:

$$\delta_1 = \frac{1}{k_{z1}} = \frac{c}{\omega}\left(\frac{\varepsilon_d + \varepsilon_{mR}}{\varepsilon_d{}^2}\right)^{0.5} \tag{2.32}$$

$$\delta_2 = \frac{1}{k_{z1}} = \frac{c}{\omega}\left(\frac{\varepsilon_d + \varepsilon_{mR}}{\varepsilon_{mR}{}^2}\right)^{0.5} \tag{2.33}$$

For terahertz regime, since $\varepsilon_m < \varepsilon_d, \varepsilon_{mI} > \varepsilon_{mR}$, the propagation length and skin depth of SPs can be approximated by

$$L_x = \frac{c}{\omega}\frac{\varepsilon_{mI}}{\varepsilon_d{}^{3/2}} \tag{2.34}$$

$$\delta_1 = \frac{c}{\omega}\left(\frac{\sqrt{2\varepsilon_{mI}}}{\varepsilon_d}\right) \tag{2.35}$$

$$\delta_2 = \frac{c}{\omega}\left(\frac{2}{\varepsilon_{mI}}\right) \tag{2.36}$$

The propagation length and skin depth exhibit a strong dependence on frequency. As shown in Figure (2.4), in the visible frequencies, SPs exhibit large field confinement to the interface that leads to small propagation length due to increased damping. In the terahertz frequencies, however, SPs fields extend more inside dielectric space, which shows small localization and larger propagation length.

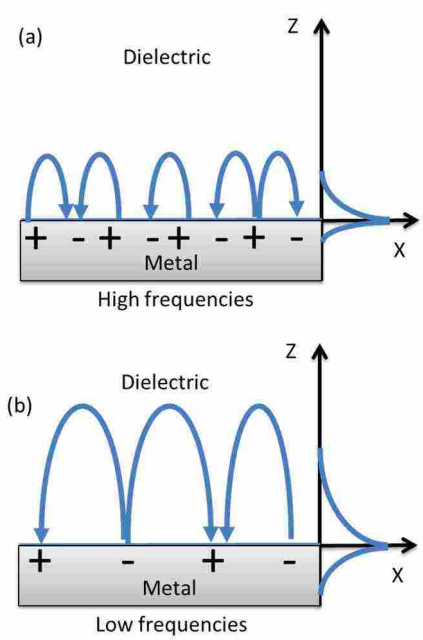

Figure 2.4 surface plasmon propagation on the interference of metal and dielectric at (a) high and (b) low frequency. Also, the exponential decay of electric filed is shown for both cases.

For example, at 0.54 THz, the skin depths of SPs inside the air layer and silicon layer are 0.14 and 0.012 m, respectively, while, the skin depth of SPs inside the Aluminum layer is 110 nm [42, 43].

Excitation of surface plasmon waves

Two-dimensional electromagnetic waves can generate surface plasmon polariton (SPP) which propagates at the flat interface between a conductor and a dielectric [48]. Confinement can be achieved if the propagation constant β is greater than the wave vector k in the dielectric or in another word, wavevector in both metal and dielectric should be matched, leading to evanescent decay on both sides of the interface. As a result, the SP dispersion curve, therefore, lies to the right of the light line of the dielectric ($\omega = ck$) that

allow SP to propagate. Three-dimensional electromagnetic waves could not excite SP unless special techniques for phase-matching are employed. There are couples of techniques to excite the surface plasmon such as prism coupling, grating coupling, charged particle impact, near-field excitation and highly focused optical beam [31]. In this section, we will introduce the two commonly used SP excitation techniques which are prism and grating coupling methods.

Prism coupling

On the interference of metal and dielectric, surface plasmon cannot be excited since the wave vector of the light in the dielectric side is smaller than β. As a result, the projection of the wave vector along the interference is always smaller than SP propagation constant β ($\beta > k_x \sin\theta$). This problem can be solved by a three-level system where a thin metal film sandwiched between two isolators with different dielectric constant [31]. Figure (2.5) shows two famous geometry of surface plasmon excitation by using a prism. A beam reflected at the interface between the prism which has higher dielectric constant ε and the metal will have a momentum $k_x = k * \sin\theta$, which is enough to excite SPs at the interface between the metal and air which has lower Ɛ. In this way, the propagation constant β can meet the SP wave vector which means the generation of the surface plasmon.

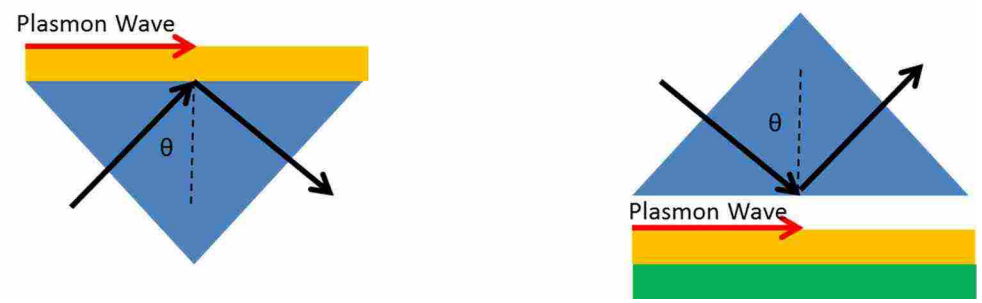

Figure 2.5 surface plasmon excitation through prism coupling in the Kretschmann (left) and Otto (right) configuration.

The most common configuration is the Kretschmann method [49] where a thin metal film is located on top of a glass prism. Incident photons which impinging from the glass side at an angle greater than the critical angle of total internal reflection can tunnel through the metal film and excite SPs at the metal/air interface. The other geometry is the Otto configuration [50], where there is a narrow air gap between prism and metal film. Total internal reflection occurs at the prism/air interface, exciting SPPs via tunneling to the air/metal interface. This configuration is preferable when direct contact with the metal surface is not possible. The dispersion relation of prism coupling is also shown in figure (2.6).

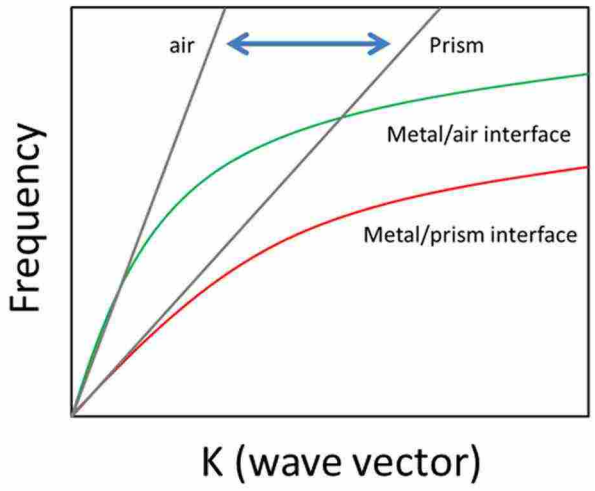

Figure 2.6 the dispersion relation for surface plasmon in the air, metal and dielectric medium which shows the propagation constant is only achievable between the light lines of air and the prism.

Grating coupling

To overcome the mismatch of β and in-plane momentum $k_x = k*\sin\theta$ of the incident beam, a metal grating structure also can be used with grooves or holes that have a lattice constant of a. figure (2.7) shows the simple example of grating structure. The phase matching takes place when the following condition satisfied:

$$\beta = k \sin\theta \pm \upsilon g \qquad (1.37)$$

Where g is a reciprocal vector of grating and ν is an integer number.

Figure 2.7 geometry of phase matching of light to surface plasmon with grating

In the case of one-dimensional gratings, significant changes to the SP dispersion relation happen if the gratings are deep so the modulation can no longer be considered as a small perturbation of the flat interface. For a groove depth on the order of 20 nm, band gap could be considered for metallic gratings [51]. For larger depths, it can be seen that the localized modes also happens inside groove which distorts the first order of SPs. However, this phenomenon enables coupling of short wavelengths [31, 48].

Localized surface plasmon

Today, with metal nanoparticle technology, the nanometer size regime becomes available in optics. The coherent oscillation of conduction band electrons in metals can modify the optical characteristics of metals [52]. These modifications in optical responses can be explained by the Plasmon effect [30]. There are particular metals such as gold and silver available to use in plasmonics applications. The interaction between the incident light and free electron of metal creates the localized surface Plasmon (LSP) effects or charge density oscillation in a closed surface of the nanoparticle. The LSP waves have the ability to scatter, absorb and squeeze the light into the nanometer dimension. Based on the

previous explanation a new filed in science and technology was established which is called Plasmonics [32, 42].

Here we are going to cite some important applications of metal nanoparticles in different areas of technologies. This plasmonic technology enables nano-optics, which can greatly increase the resolution and the signal strength in an imaging system and spectroscopy [34]. If metal nanoparticles (NP) are attached to the molecules, the molecular fluorescent can be enhanced [47]. So in this way the new light emitting devices are available for fluorescence microscopy [53]. Also with using metal NP arrays it is possible to manipulate and control the absorption and transmission of the optical signal. Negative refractive index, super-lensing effect, and metamaterials are other novel subjects where metal nanoparticle based plasmonics plays an important role in these subjects [54, 55].

There have been many applications and research outcomes in the biomedical and biotechnology areas. For example, biomolecules labeled with metal NPs can be traced in real time during the biological process. Moreover tuning the optical response of metal NP is available by using functionalized NPs. This tailored property can be used to destroy the tumor cells when the metal NPs are selectively attached to the tumor cells. In this procedure, near infrared incidence will excite the resonance frequency of metal NPs, and the localized heat from the electron resonance energy will kill the tumor cells [36, 56].

Three different driving forces make metal NP plasmonics one of the hottest topics in today's researches. First, development of sophisticated lithography technology and chemical methods allow the mass production of NPs with complex structures. The possibility of synthesizing and tuning metal building blocks give us this opportunity to

control and engineer the Plasmon response of NPs. This control and tuning availability open new area in material science, communication and biochemistry [52].

Second, measurement technologies are greatly improved in a recent year. The capabilities of monitoring single particle, spatially map response on nanoscale and access ultra-fast time scale are enhanced by NPs plasmonics [52].

Third, the capabilities of modeling and simulation of NPs optical response have been greatly extended. These extensions provide a detailed and quantitative understanding of NPs. So, a perfect simulation of NPs will help both theory and experiment to develop and creating novel structures for future works [52].

Basic theory of LSPR

Light interaction with a particle of size d could be analyzed by quasi-static approximation when $d << \lambda$; the particle is much smaller than the wavelength. In this condition, the phase of the harmonically oscillating electromagnetic field is practically constant over the particle volume; therefore, the spatial field distribution can be calculated by assuming the simplified problem of a particle in an electrostatic field. This approximation of the full scattering problem defines the optical properties of nanoparticles smaller than 100 nm adequately.

Figure (2.8) shows a homogeneous sphere placed into an electrostatic field $E=E_0z$. The surrounding medium is isotropic and non-absorbing with the dielectric constant ε_m, and the field flux lines are parallel to the z-direction. The sphere dielectric function describes by $\varepsilon(\omega)$. Here we are trying to solve the potential equation $\nabla^2\Phi = 0$ which leads to electric field solution.

The general solution for following geometry is [47]:

$$\Phi(r,\theta)=\sum_{l=0}^{\infty}\left[A_l r^l + B_l r^{-(l+1)}\right]P_l(\cos\theta) \tag{2.38}$$

where $P_l(\cos\theta)$ are the Legendre Polynomials of order l, and θ the angle between the position vector r at point P and the z-axis. Since the potential has to be finite then the solution for potential inside and outside of the sphere can be written as [47]:

$$\Phi_{in}(r,\theta)=\sum_{l=0}^{\infty}A_l r^l P_l(\cos\theta) \tag{2.39}$$

$$\Phi_{out}(r,\theta)=\sum_{l=0}^{\infty}\left[B_l r^l + C_l r^{-(l+1)}\right]P_l(\cos\theta) \tag{2.40}$$

The coefficients A_l, B_l, C_l can be defined from the boundary conditions at $r \rightarrow \infty$ and at the sphere surface r = a. The other coefficients A_l and C_l are described by the boundary conditions at r = a. Finally, we can derive the following equations for potential inside and outside of the sphere [47].

$$\Phi_{in}=-\frac{3\varepsilon_m}{\varepsilon+2\varepsilon_m}E_0 r\cos\theta \tag{2.41}$$

$$\Phi_{out}=-E_0 r\cos\theta+\frac{\varepsilon-\varepsilon_m}{\varepsilon+2\varepsilon_m}E_0 a^3\frac{\cos\theta}{r^2} \tag{2.42}$$

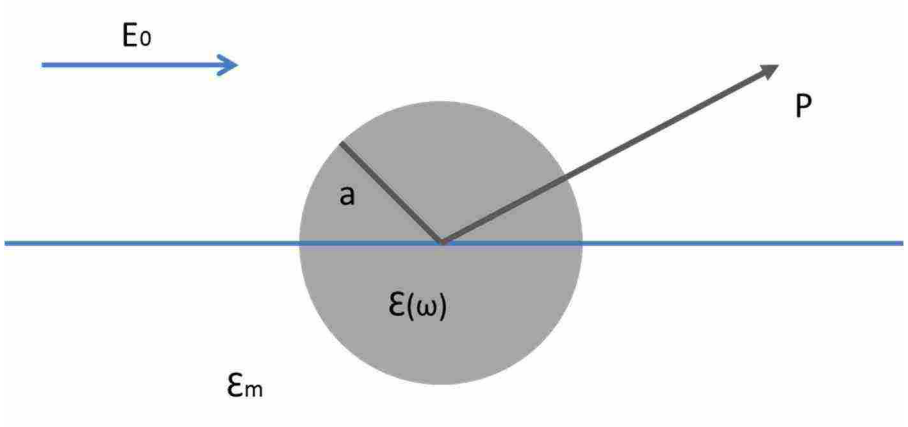

Figure 2.8 Sketch of a homogeneous sphere placed into an electrostatic field.

Φ_{out} describes the superposition of the applied field and that of a dipole located at the particle center. Equation (2-42) could rewrite by the dipole moment P [47]:

$$\Phi_{out} = -E_0 r\cos\theta + \frac{P.r}{4\pi\varepsilon_0\varepsilon_m r^3} \tag{2-43}$$

$$P = 4\pi\varepsilon_0\varepsilon_m a^3 \frac{\varepsilon-\varepsilon_m}{\varepsilon+2\varepsilon_m} E_0 \tag{2-44}$$

The polarizability α could be defined as follow [47]:

$$\alpha = 4\pi a^3 \frac{\varepsilon-\varepsilon_m}{\varepsilon+2\varepsilon_m} \tag{2-45}$$

At this point we can drive the electric field distribution by using potential equations [47]:

$$E_{in} = \frac{3\varepsilon_m}{\varepsilon+2\varepsilon_m} E_0 \tag{2-46}$$

$$E_{out} = E_0 + \frac{3n(n.P)-P}{4\pi\varepsilon_0\varepsilon_m}\frac{1}{r^3} \tag{2-47}$$

As it is clear, the resonance in α also causes a resonant improvement of both the internal and dipolar fields. This field-enhancement at the plasmon resonance on which many of the applications of metal nanoparticles in optical devices and sensors could be establishes.

By using Poynting vector, we can approximate the corresponding cross sections for scattering and Absorption C_{sca}, C_{abs} [47]:

$$C_{sca} = \frac{k^4}{6\pi}|\alpha|^2 = \frac{8\pi}{3}k^4\alpha^6\left|\frac{\varepsilon-\varepsilon_m}{\varepsilon+2\varepsilon_m}\right|^2 \tag{2-48}$$

$$C_{abs} = k\,\mathrm{Im}[\alpha] = 4\pi k\alpha^3\,\mathrm{Im}\left[\frac{\varepsilon-\varepsilon_m}{\varepsilon+2\varepsilon_m}\right] \tag{2-49}$$

For small particles where, a<< λ, the efficiency of absorption, scaling with a^3, dominates over the scattering efficiency, which scales with a^6.The expressions for the cross sections (2-48, 49) are valid for dielectric scatterers. Due to the rapid scaling of Csca ∝ a^6, it is almost impossible to eliminate small objects from a background of larger scatterers. Here it is common to define the extinction factor for nanoparticles which is shown in equation (2-50) [36].

$$C_{ext} = C_{abs} + C_{sca} = 9\frac{\omega}{c}\varepsilon^{3/2}{}_m V\frac{\varepsilon_2}{[\varepsilon_1+2\varepsilon_m]^2+\varepsilon_2{}^2} \tag{2-50}$$

Figure (2.9) shows the extinction cross section of a silver sphere in the quasi-static approximation calculated using this formula for immersion in two different media.

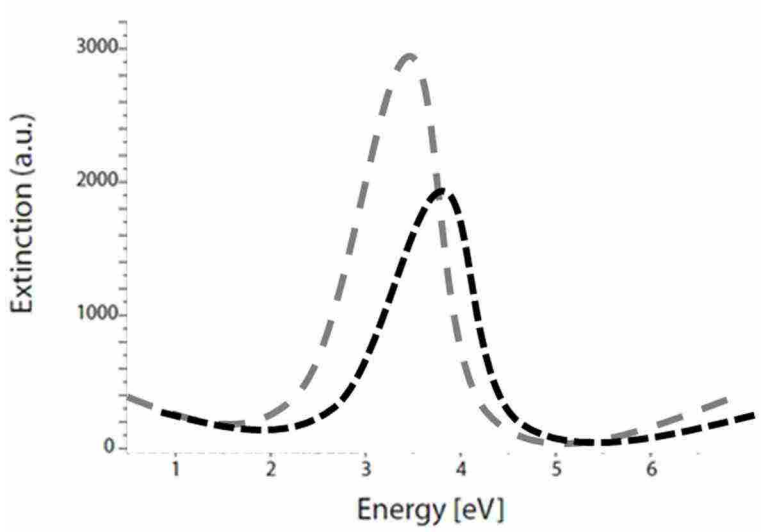

Figure 2.9 Extinction cross section calculated using (5.14) for a silver sphere in air (black curve) and silica (gray curve), with the dielectric data.

Nanoparticle plasmonics

In this section, we are going to explain a complete theoretical model for NP plasmonics. Towards this goal, two principle challenges are important. 1) An accurate description of the response of the electron plasma in the material that makes up the NP, 2) determining the effect of the particle geometry on the electromagnetic fields. The most common approach to the first issue is the classical dielectric formalism, where the material linear response is described by a local bulk dielectric function $\varepsilon(\omega)$. After this step, the different boundary conditions are set based on various geometries for solving Maxwell's equations.

In the simplest model used for the dielectric response, the response of the free-electron plasma is characterized by a harmonic oscillator. The resulting dielectric function is given by the Drude formula, $\omega = 1 - \frac{\omega^2 P}{(\omega(\omega + i\gamma))}$ where γ is the frequency dependent damping and ωp is the bulk metal plasma frequency, which depends on the metal electron density, n, the electron charge, e, and the electron mass, me. Mie solved the equation for the sphere, and the results are known as Mie theory. Figure (1.12a) shows the results.

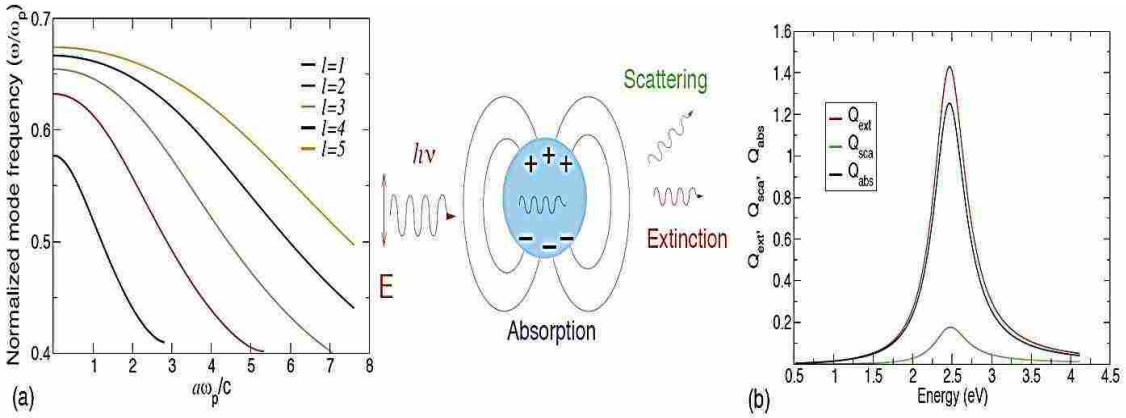

Figure 2.10 (a) Modes of a spherical metal NP as a function of the particle radius *a*. Dipolar (l = 1), quadrupolar (l = 2), and higher-order modes are plotted. Mode frequencies are normalized by the bulk plasmon frequency ωp. (b) Scattering, absorption and extinction coefficients (cross sections normalized by the particle geometrical area) for a spherical metal NP of radius a = 10nm, and schematic of the scattering geometry. Reprinted with permission from [52]. Copyright (2008) John Wiley and Sons.

The first order which relates to dipole response is represented by l=1. For small particles ($a << c/\omega_P$), the energy of this mode is $h\omega = h\omega_P/\sqrt{3}$. This mode redshifts as the particle size increases, due retardation effects. This is the mode typically excited by linearly polarized light and is responsible for the dominant feature in the optical spectra of

colloids. Figure (2.10b) shows typical absorption, scattering and extinction optical spectra for a 10 nm particle in a vacuum.

To understand the optical response of more complex nanostructures, it is necessary to use rigorous computational approaches capable of handling arbitrary geometries. Quantitative theories based on empirical dielectric response functions, rather than simple Drude models, also motivate the use of computational approaches. Among the numerical methods most commonly used are the finite difference time domain (FDTD) method, the discrete dipole approximation (DDA), Greens function approaches similar in spirit to the DDA, the multiple multipole (MMP) method, multiple scattering techniques, transfer matrix approaches, plane wave expansions, and boundary element methods (BEM). Among mentioned method, FDTD is one the best choice and successful approaches to simulate plasmon waves in NPs. The FDTD method involves a discretization of Maxwell's equation in space then time domain equation is applied to each cell based on previous values of that cell and the boundary conditions.

Nanorods analysis based on size and shape

Nanorods are in interests, because manipulating their length and width will provide extreme tunability over plasmon properties. As a cylindrical rod of length Lrod, radius R, with hemispherical end caps and total length Ltot = Lrod + 2R provides a good approximation for the typical geometry of real particles. The near- and far-field optical response for such rods of different lengths, including retardation, by means of the boundary element method, is shown in Figure(1.13)

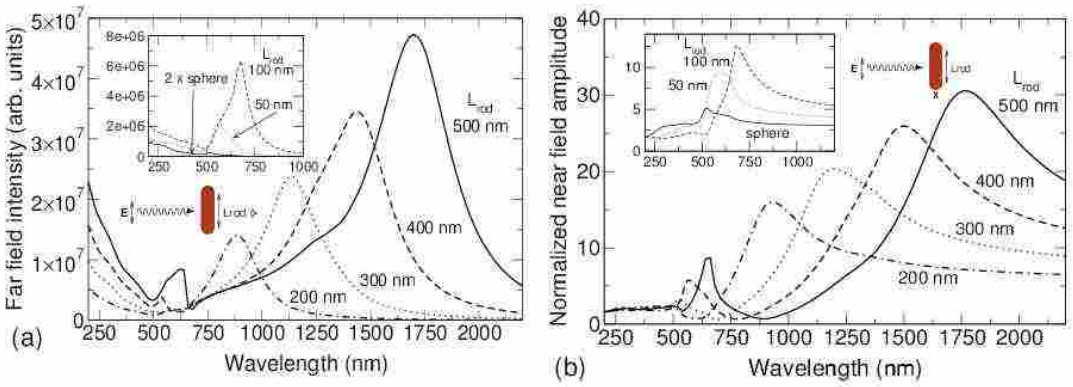

Figure 2.11 (a) Far-field scattering intensity as a function of wavelength for a plane wave incident on an Au nanorod of radius R = 40nm. (b) Normalized near-field amplitude 1 nm from the nanorod end. Reprinted with permission from [52]. Copyright (2008) John Wiley and Sons.

For the far field, response below 500 nm is a bulk response and does not occur in the near field. The longest-wavelength peak in the response corresponds to the dipole resonance. The near-field resonance wavelength depends strongly on the location along the rod where it is measured. A blueshift of the resonance is observed as the measurement position is moved along the rod from the end to the center, while remaining a fixed distance away from the surface, as shown in Figure (2.12) Near the center of the rod, in fact, the dipolar resonance disappears. This variation of the resonance along the rod axis is of great importance for any application that exploits the plasmon resonance to modify the response of attached molecules or other nanostructures.

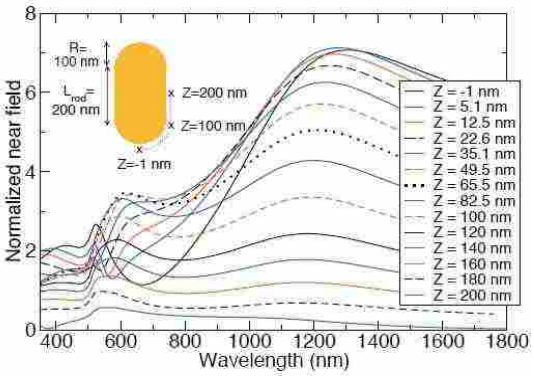

Figure 2.12 Position dependence of the near-field response of a gold nanorod with length Lrod = 200 nm and radius R = 100 nm. Reprinted with permission from [52]. Copyright (2008) John Wiley and Sons.

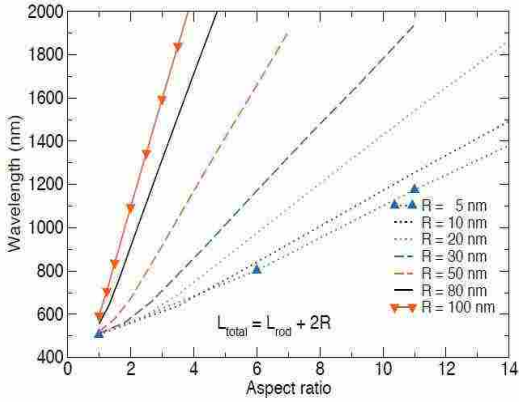

Figure 2.13 The dependence of the dipole resonance wavelength on aspect ratio $L_{tot}/(2R)$ for different radios R. Reprinted with permission from [52]. Copyright (2008) John Wiley and Sons.

The peak wavelengths for the dipolar resonance, as extracted from the calculated spectra for the far field and the normalized near-field response, increase approximately linearly with increasing L_{tot}, except when the longitudinal dimension L_{tot} is comparable to the lateral dimension 2R and end effects are dominant. For small R, dipole resonance wavelengths extracted from the far field and near field response are nearly identical. As R increases, the near-field resonance becomes noticeably redshifted from the far-field resonances.

So far, we explained about the dependence of plasmon resonance on length and thickness of Nanorods. Another geometry which plays an important role in determining the resonance frequency is the aspect ratio. The aspect ratio for Nanorods is defined $L_{tot}/(2R)$.

This dependence cannot be explained quasi-static model because this model, the quasi-static model, is simple but compelling, ignoring any explicit dependence on nanorods length or radius. A full mapping of the plasmon dipole resonances in nanorods from full electromagnetic calculations, including retardation, provides a stringent test for this approach. The dependence on aspect ratio is shown in Figure (1.13) For different R. In the quasi-static limit, the plasmon resonance should be independent of R, and all curves should be identical. Surprisingly, there is no such region.

Coupled plasmons

If two sources of plasmon wave have resonance together, then there would be a possibility for each plasmon waves to be coupled with the other one. This is a simple definition for coupled plasmon concept, but there are lots of difficulties in calculations. These coupling can have different effects on optical responses. For example, the coupling between the plasmon on the inner and outer edges of the nanorings causes huge redshift in the resonance peak. The amount of coupling and resonance shift depends on complexity, shape, and interspace distances. Sometimes this coupling happens in one particle but for different regions like nanorings and nanostars. These couplings cause enhancement in near field magnitude, especially around the interspace distance. Therefore, this coupling mechanism can be used for the sensors in various areas [30].

To understand coupled plasmons, the concept of the plasmon hybridization can be used. In the same way, that atomic orbitals hybridize to form bonding and antibonding orbitals in molecules, plasmons in different particles can couple in phase or out of phase, with the strength of the coupling determining the induced resonance shift. The effect of the plasmon

hybridization can be seen by considering two coupled dipoles, as illustrated in Figure (2.14). Hybridization can redshift or blueshift the resonance, depending on the dipole orientation. When the dipoles are coupled end-to-end, the field generated by one dipole (the black dipole in the figure) at the second dipole is in phase with the polarization of the first dipole. As a consequence, the optically active, hybridized mode of the pair is redshifted from the single-dipole resonance frequency. When the dipoles are coupled side-by-side, the field generated by the black dipole at the second dipole is out of phase with the polarization of the first dipole. The second dipole responds out of phase to the driving field, at frequencies blueshifted from the single-dipole resonance [30].

To fully understand plasmon coupling in such cases, detailed calculations are necessary. Figure (2.14) shows the calculated dependence of the dipolar response on the separation between two identical gold rods. Several regimes with clearly different behavior are apparent and have been observed experimentally. For gaps smaller than a nanometer, the dipole resonance continues to redshift, but the far-field dipole scattering saturates and is then suppressed, as shown in Figure (1.15) The charge localization at the gap becomes so large that the dipole mode cannot support additional charge localization, and charge oscillation along the rods is inhibited. At the same time, higher order modes are excited to support the charge localization. However, they also saturate in turn as the gap is decreased [30].

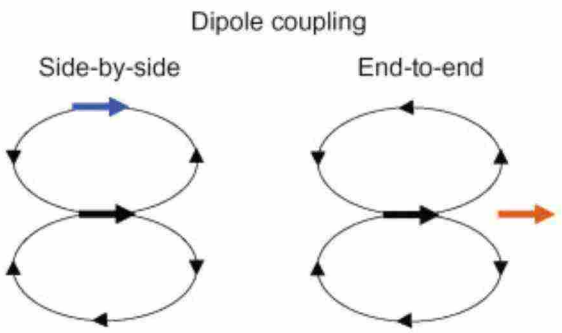

Figure 2.14 (a) Schematic of dipole-dipole coupling. The field lines of the black dipole are indicated. (b) Far-field and near-field response of a pair of identical Au nanorods, coupled end-to-end, as a function of gap separation, for a plane wave incident with polarization along the rods. Reprinted with permission from [52]. Copyright (2008) John Wiley and Sons.

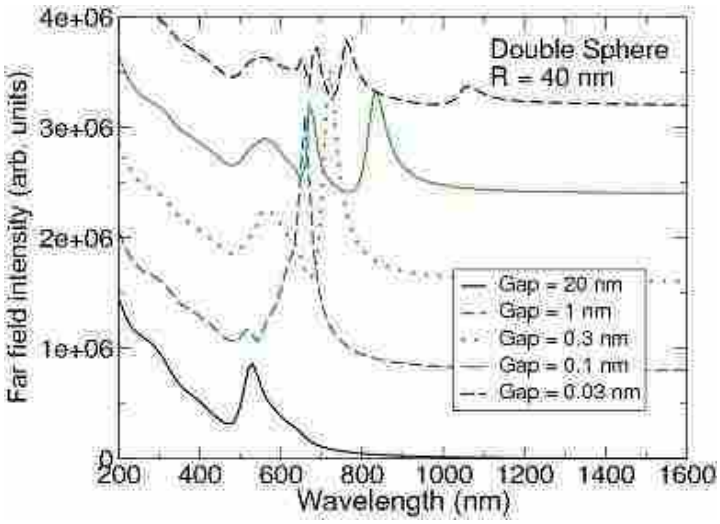

Figure 2.15 Spectra of the far-field intensity of a pair of coupled, identical gold nanospheres for different separations between the spheres. Reprinted with permission from [52]. Copyright (2008) John Wiley and Sons.

Photogeneration of hot plasmonic electrons with metal nanocrystals

The nanoscale particles at certain frequencies can generate hot carries. The efficiency of hot electron generation in nanostructures is high due to the non-conservation of the momentum of electrons in a confined nanoscale system. Once the size of nanostructures increases the number of induced plasmonic hot carries generation decreases with same excitation energies. Moreover, the light polarization is also important. When the optically induced electric current has the same direction as the smallest dimension of nanostructures, the hot carrier generation has the highest efficiency.

To design a plasmonic detector or device, there are three main limitations that have to be considered.

1. Intra-band transitions are responsible for generation of energetic carriers and also dominate the absorption
2. Intra-band transition generates both electron and hole with higher energy
3. The carries generation and absorption spectra can be significantly different

Experimentally, the generated hot carriers from nanostructures could be collected through a semiconductor metal Schottky barrier photodetector as a photocurrent or surface photochemistry.

The induced plasmonic hot electrons are attractive in many applications such as: solar cell, and a photodetector, because the nanostructures can enhance the light absorption in the mentioned devices. The benefits of metal nanostructures are summarized as follow:

- Large absorption cross section

- Hot electrons with enough energy level to be transferred
- Tunability of plasmonic response of nanostructures by changing the dimensions and sizes

Plasmonic nanocrystals

The energy of the electron is quantized inside the metal nanostructures. Like the quantum mechanics theory, we could define the energy of an electron due to potential wall of nanocrystals. Figure (2.17) shows the energy of electrons is quantized and optical transitions occur between the discrete states. The hot electron distribution of LSPR is different from the bulk system. Hot electrons in a confined nanocrystal occupy all region of the allowed energies[57].

$$E_F < \text{Hot electrons} < E_F + \omega \tag{2.51}$$

This can be understood considering the fact by the conservation of energy, a hot electron can have the energy $E_{excited} = E + \omega$. Therefore, the peak allowed the energy of the electron in the system is $E_{max} = E_F + \omega$ and, the hot-electron distribution extends from the Fermi energy to the peak value (the blue part of the curve in Figure (2.16c)). Moreover, the energy interval for photo-excited holes is $E_F - \omega <$hot holes$< E_F$ (the red part on the curve in Figure (2.17c)).

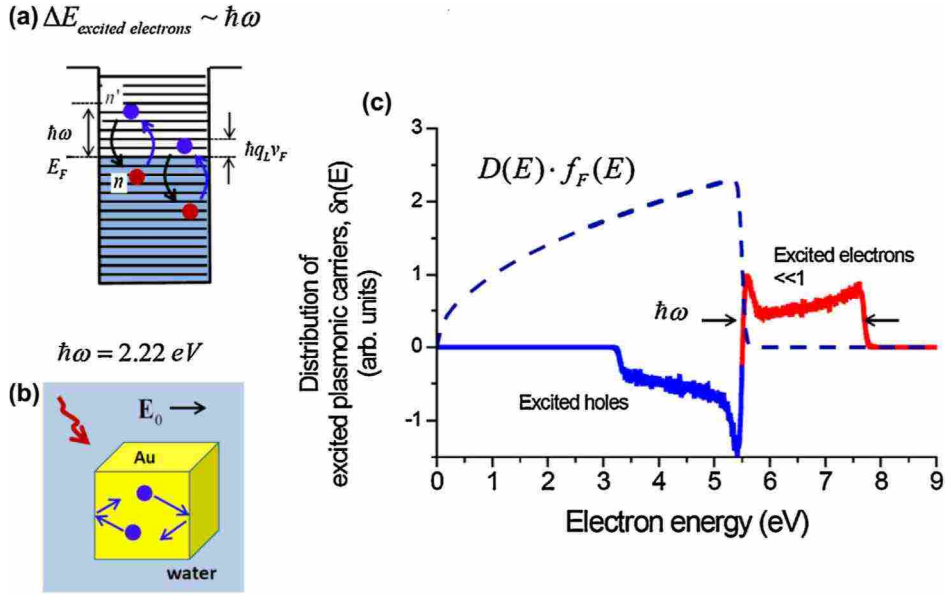

Figure 2.16 (a) the electron transition in metal nanocrystal. First the electron in fermi sea becomes excited then a steady-state distribution of high-energy electrons in a localized plasmon wave forms. (b) Model of an Au nanocube with electrons inside the walls. (c) Plasmonic electron distribution in the localized surface plasmon in a 10 nm gold nanostructure. Reprinted with permission from [57]. Copyright (2014) Elsevier.

Surface plasmon Vs. Localized surface plasmon

Although SPR and LSPR seem to have a similar mechanism but they are quite different in fundamental technologies. Surface plasmon resonance (SPR) is a wave that propagates along the metal surface in an evanescent mode. Figure (2.17) shows typical SPR technology. As it is illustrated this technology needs a complicated optical geometry which includes a controlled metal thin film and prism to excite Plasmon mode. A highly sensitive detection system also needs to integrate to this setup since SPR is the angle dependence phenomenon. The related equation (2-52) shows that the incident angle and refractive index are two key parameters that can manipulate the wave numbers at the boundary between

metal thin film and prism. High sensitivity to refractive index and incident angle makes SPR a valuable candidate for sensing applications [37].

$$k_{\square,\mathrm{Pr}ism} = \sqrt{\varepsilon_d}\,\frac{\omega}{c}\sin\theta = k_{sp} \tag{2-52}$$

Where $k_{\square,\mathrm{Pr}ism}$ and k_{sp} are wavenumbers on prism and metal surface, θ incident angle of light on the metal surface and $\sqrt{\varepsilon_d}$ is dielectric constant on metal.

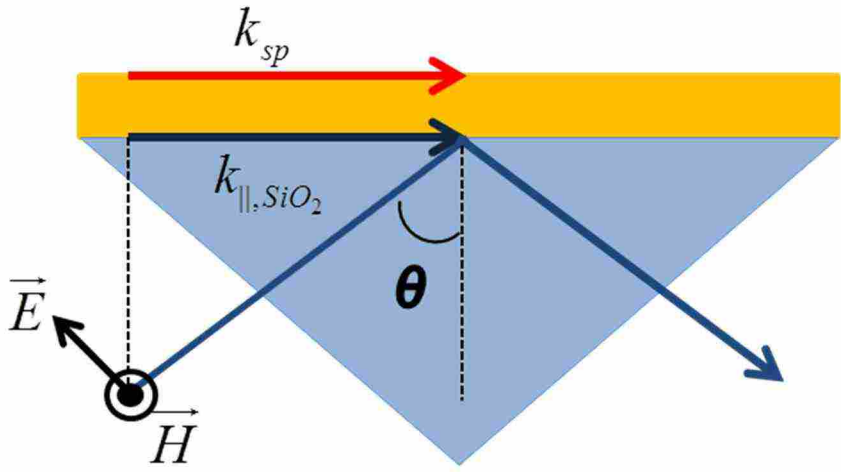

Figure 2.17 surface plasmon resonance typical excitation geometry using prism and noble metal thin film (Kretschmann)

On the other hand, localized surface plasmon (LSPR) occurs when metal nanoparticle structures are smaller than the wavelength of incident light. Figure (2.18) shows the LSPR excitation in gold nanoparticles. Based on the Mie theory, if the nanoparticle (NP) size is relatively smaller than the wavelength, then at resonance frequency, the NP shows dipole behavior where electrons resonate by absorbing photon energy. Therefore, it appears with

strong absorption at specific wavelength. The related equation (2-53) shows the extinction coefficient for metal nanoparticles. As it can be seen, this coefficient is related to volume and the host refractive index matrix of NPs [37].

$$\sigma_{ext}(\lambda) = 18\frac{\pi}{\lambda}\varepsilon_H'^{1.5}V_M \frac{\varepsilon_M'(\lambda)}{[\varepsilon_M'(\lambda)+2\varepsilon_H']^2+\varepsilon_M''(\lambda)^2} \quad (2\text{-}53)$$

Where λ=wavelength, V_M volume of nanoparticle, Ɛ' and Ɛ'' are real and imaginary part of the permittivity respectively.

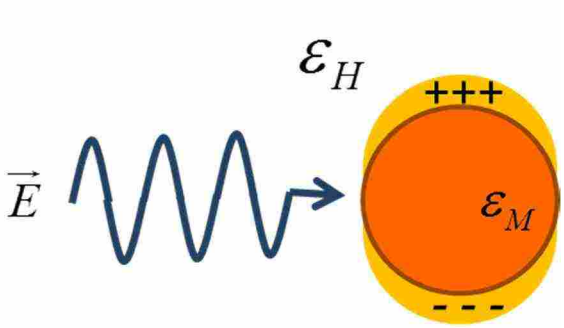

Figure 2.18 localized surface plasmon excitation using noble metal nanoparticles.

Table (2-1) shows a comparison between SPR and LSPR sensing technologies toward sensing application especially in biology.

Table 2-1 Comparison of SPR and LSPR sensing technology

Properties	LSPR	SPR
Label-free sensing	YES	YES
Bulk Dielectric Sensitivity (nm/RIU)	10^2	10^6
Sensing Distance (nm)	10	1000
Signal-to-Noise ratio	Worse	Better
Instrumentation	Simple	complex
Temperature Sensitive	No	Yes
Target mass per unit surface area (ng/cm^2)	Better	Worse

Both LSPR and SPR are capable of label-free sensing since they both are sensitive to local refractive index changes [49]. As a result, once a target analyte binds to the metal surface (SPR) or metal NPs (LSPR), eventually both SPR and LSPR sensors show different response. In addition, both LSPR and SPR provide real time information of an event [45]. Recent studies showed that the SPR sensing has superior bulk dielectric sensitivity due to the refractive index and angle dependence in its excitation geometry. Moreover, SPR has higher sensing distance in comparison with LSPR. However, it is also reported that LSPR sensor has better detectivity in ng/cm^2 (target mass per unit surface area, a common metric for SPR sensors) than a typical SPR sensor. This high detectivity can compensate the poor bulk dielectric sensitivity of LSPR [50]. Therefore, highly efficient and robust sensors can be developed using LSPR technology [51, 52]. LSPR sensors also have advantages such

as no temperature dependence in its optical property, simple instrumentation capability and a broad range of responses. After considering everything, we chose LSPR technology as our sensing method. There are two basic different ways to detect LSPR. Conventional LSPR was detected using absorbance measurement of NPs. The Schottky junction based direct measurement is a new method that reported couple of years ago. Unlike the conventional LSPR detection, the Schottky junction based detection, has advantages of the simple read-out system (no need to optical instruments) and integrability on small size electronic chips by using semiconductor technology [53-56]. In the next section, we will discuss LSPR energy detection using Schottky junction based devices.

Summary

In this chapter the background physics of SPR and LSPR were presented. By using Drude model, the interaction of light with metal was explained. Moreover different excitation mechanisms for SPR using prism and thin metal film were discussed. In addition, LSPR theory was presented by explaining the Mie theory. Metal nanoparticles in the case LSPR show different absorption spectrum with different size, composition and surrounding refractive index. Both SPR and LSPR have several advantages and they can be used in several applications such as bio-sensors, photovoltaic devices and plasmonic wave guides.

Chapter 3

Novel plasmon to electron conversion device: plasmon field effect transistor

Plasmon field effect transistor (FET) is a novel sensing platform to detect and amplify the plasmonic energy. Unlike the conventional LSPR sensors which work based on the absorption spectrum, plasmon FET does not need any bulky optical instrument for detection of the plasmonic energy. Simply, by reading the drain current of plasmon FET, we can detect the plasmonic energy. A similar direct plasmonic detection devices have been reported using nanostructured metal-semiconductor Schottky diodes. Compared with theses Schottky junction based devices, the plasmon FET has several advantages as a sensing platform such as high quantum efficiency from the amplification mechanism, and functionalization capability due to its electrically isolated metal nanostructures.

In this chapter, we first explain the mechanisms of plasmon resonance detection and energy conversion by using Schottky junction based devices. Then, we will introduce our novel plasmon FET as an excellent sensing platform that addresses the issues from the current LSPR sensing technologies. The proposed plasmon FET is a back-gate thin film transistor with incorporated gold NPs. The conduction layer of the FET is made from a ZnO film, which is optically transparent due to its large energy band-gap. In this work, we have used ZnO for transistor channel in order to avoid the optical absorption spectra between gold nanoparticles and transistor active channel. However, the transistor channel could be any n-type semiconductor materials such as Si or other compound semiconductors. The overall structure and working principle of plasmon FET will be discussed later in this chapter.

Schottky junction based diodes as plasmon detector

As briefly discussed in the introduction, there have been several report about Schottky diode based devices that enable a direct detection of plasmonically absorbed energy in gold nanostructures [11, 42, 58, 59]. These successful demonstrations made a big step for plasmonic integrated circuits as the next generation technology. The plasmon field effect transistor also has a Schottky junction between metal nanostructures and the semiconductor film. Therefore, it is important to understand the working mechanism of Schottky junction based plasmonic detection. In this section, we will start to discuss the details of the Schottky junction based plasmonic detection. Figure (3.1) shows the energy band diagram of a Schottky junction. Depending on the nanostructure, the incoming photon with a certain frequency can excite hot electrons in the metal following its plasmonic absorption spectrum. If the excited hot electrons have enough energy to overcome the Schottky barrier, they can generate photocurrent [58, 60]. Thus, the Schottky junction based diodes provide direct conversion of plasmon energy into electrical current. The responsivity of this device to incoming light in the absence of plasmon resonance depends on the energy-dependent internal photoemission probability. This quantum transmission probability η can be approximated by Fowler theory which describes the number of electrons in the system with sufficient energy to overcome the Schottky barrier [61, 62]:

$$\eta = C_F \frac{\left(h\nu - q\phi_B\right)^2}{h\nu} \tag{3-1}$$

where C_F is the device-specific Fowler emission coefficient [62], $h\nu$ is the photon energy, and $q\phi_B$ is the Schottky barrier energy. By fitting the responsivity curve of a planar Schottky junction with equation (3-1), we can extract the material dependent Schottky

barrier height for a given metal-semiconductor interface. Once the Schottky barrier forms by the plasmon resonance, the total quantum transmission probability (responsivity R) could rewrite as follow [8]:

$$R(v)=\eta S(v) \tag{3-2}$$

Where S(v) in general depends on multiple factors, including the geometry, composition, and size of the plasmonic devices [2]. In the quasi-static regime, the plasmonic particles are smaller than the wavelength of light; the optical response will show the dipolar behavior and will demonstrate a Lorentzian line shape near the resonance frequency [42].

The working principle of such devices was reported years ago [62, 63]. The photon with specific energy level can generate hot electrons inside metal nanostructures. If the generated hot electrons could overcome the Schottky barrier at the boundary of metal nanostructures and the semiconductor layer, then the hot electrons can move to the semiconductor layer, resulting in photocurrent (Figure(1.3)) [3, 64]. A typical design scheme which has been used so far for Schottky junction based hot electron detection is making the nanostructured plasmon absorbers to serve as one electrode in diode structure. A wide bandgap semiconductor was used to prevent an overlap of absorption spectra between plasmon absorber and semiconductor. However, the Schottky based junction devices have very low external quantum efficiency due to the limited absorption in a thin metal structure and inefficient hot electron diffusion from metal to semiconductor [65]. Another disadvantage of Schottky plasmon detector is their limited use as a sensing

platform due to the electrically connected metal nanostructures that need to be functionalized with target molecules.

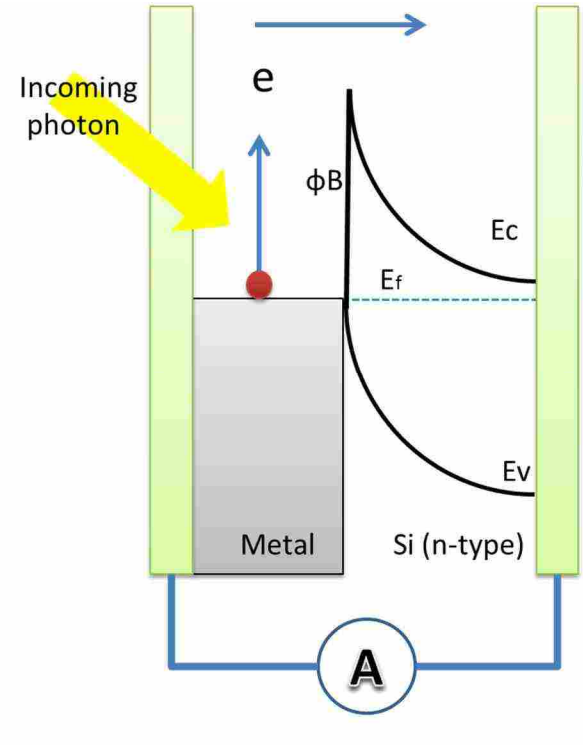

Figure 3.1 Metal-semiconductor Schottky junction hot-electron emission. The band diagram shows plasmonically driven internal photoemission from the gold nanostructure to the semiconductor. E_C, E_F and E_V stand for the conduction band, Fermi level and valance band, respectively. And Φ_b is the barrier energy height.

Plasmon Field effect transistor

In this section, we first explain the basic working principle of field effect transistor (FET), then we will discuss the details of the plasmon FET such as device structure, energy band diagram and working principles.

The field effect transistor (FET) is a type of transistor that uses an electric field to control the conductivity of the channel. Depending on the semiconductor type this channel could be p or n type [66]. This type of transistor considered as a unipolar transistor as there is one type of charge carriers that involve in transistor operation. Figure (3.2) shows the basic structure of complementary metal oxide semiconductor (CMOS) field effect transistor. This structure of the transistor which the gate is located at the top of the channel area is mostly used for amplification and switching functions. It is good for low power device and has an excellent integration capability. The other type of FET, thin film transistor (TFT), is shown in figure (3.3) where the gate connection is located at the bottom of the transistor. Although the back-gate transistors have same transistor characteristics, they are more suitable for non-Si materials, and they have lower fabrication cost. Depending on semiconductor type, the biasing voltage could be positive or negative to create conducting channel. Source-drain biasing also creates a horizontal electric field which moves the electrons or holes inside channel while gate voltage generates saturation area inside the channel. In other words, there are two different electric fields inside transistor which are perpendicular to each other [66].

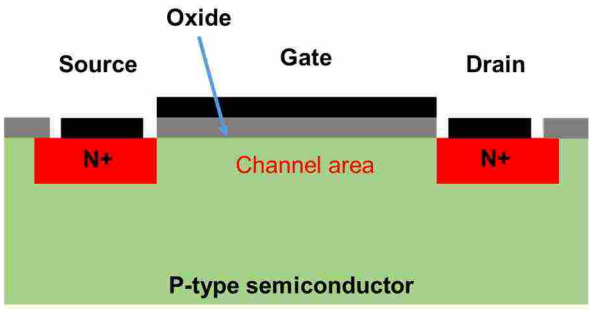

Figure 3.2 conventional field effect transistor structure with a gate on top of the channel area

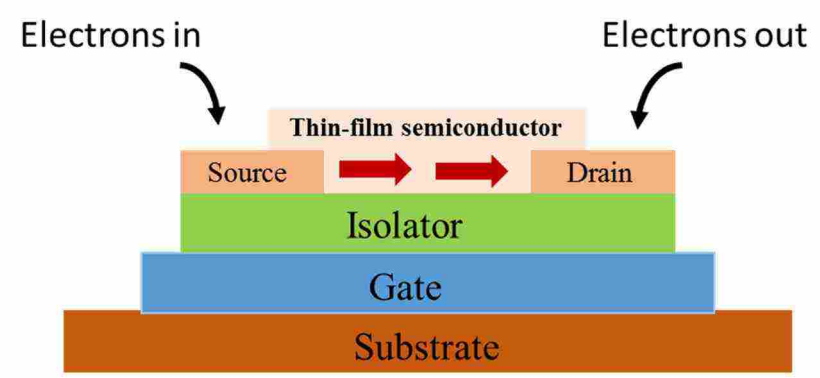

Figure 3.3 conventional back-gate field effect transistor

Based on the biasing voltage, there could be three different defined mode of operation for FET. For gate voltage below threshold voltage $V_g<V_{th}$, there is no conducting channel so the transistor is in the cutoff region and no current passes through the semiconductor layer. Once gate voltage increases more that the threshold voltage; channel forms inside the semiconductor. At this point, the transistor acts as a resistor with low Vds, because the magnitude of the horizontal electric field is small. This mode called linear region because with increasing of drain-source voltage, transistor current also increase. Finally by increasing V_{ds} FET goes to saturation region where transistor current is no longer depend on V_{ds}. Figure (3.4) shows these three regions [66].

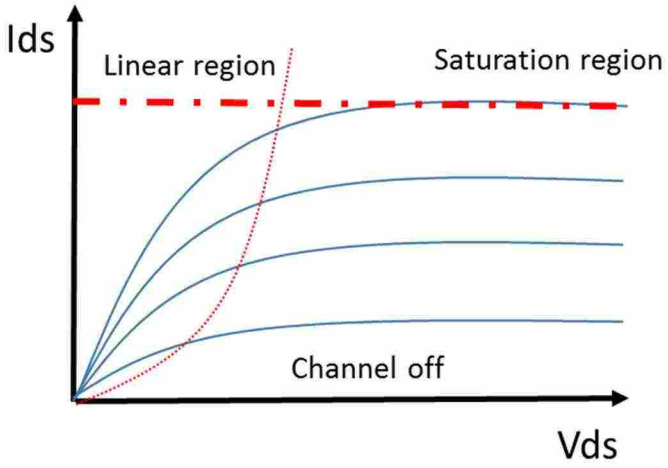

Figure 3.4 typical I-V characteristics of conventional FET. Linear, channel off and saturation are the three common modes of FET operational condition.

Structure of plasmon FET

Figure (3.5) shows the schematic of our proposed plasmon FET. The device consists of a field effect transistor with an n-type ZnO channel. ZnO is a wide bandgap (3.3eV) material which is transparent in the visible region and has absorption at UV ranges [67]. Under ZnO layer, there is a SiO_2 layer which acts as an insulator. The insulation layer is on top of the heavily doped silicon substrate which provides gate control for our proposed device. Gold nanoparticles are on top of the ZnO layer which is shown in Figure (3.5). These metal nanoparticles are the source of induced plasmonic energy under the incident light. Based on the literature, the LSPR absorption is in the visible wavelengths which are around 500-700nm for gold nano particles [68]. However, the size of nanoparticles, composition and surrounding refractive index are three important parameters in determining the absorption spectrum profile [64, 69].

As shown in figure (3.5), the gold nanoparticles are isolated electrically from transistor structure. The field effect transistor forms a current channel at the bottom part of ZnO layer near SiO_2/ZnO junction. Therefore, the applied positive voltage to the gate causes a formation of electron channel at the lower part of ZnO layer. The junction between each gold NP and ZnO layer forms a Schottky junction which has a barrier height around 0.6-7eV. Gold NPs under the illumination of light produce more hot electrons at the wavelength of plasmonic absorption. These hot electrons could be contributed to transistor drain-source current with two different mechanisms. First, the hot electrons are able to jump over Schottky barrier if they have enough energy which should be more than Schottky barrier energy. Second, the plasmonically induced hot electrons can tunnel through the Schottky barrier when the Schottky barrier thickness becomes thinner by the applied gate bias. Figure (3.6) shows these two mechanisms. Once these hot carriers get inside ZnO layer, the electric field produced by gate voltage moves them in the form of drift current. This drift current of hot electron is perpendicular to FET current which produced by drain source voltage. Also, it is proportional to the gate voltage magnitude. When these hot carriers reach the bottom of ZnO layer, FET current channel, an enhancement in current can be detected directly through a simple drain current measurement. When more carriers such as electrons come inside current channel of the transistor, depending on the gate voltage, more carriers will be generated and, as a result, current level increases. Increasing the number of electrons inside ZnO layer could be interpreted as increasing in conductivity level of ZnO layer. This enhancement in conductivity causes drain current enhancement.

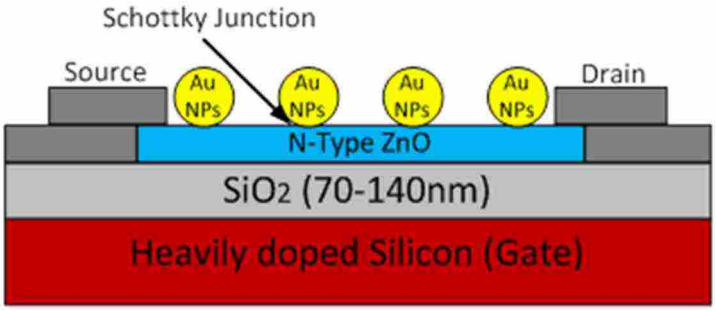

Figure 3.5 schematic of our proposed plasmon field effect transistor

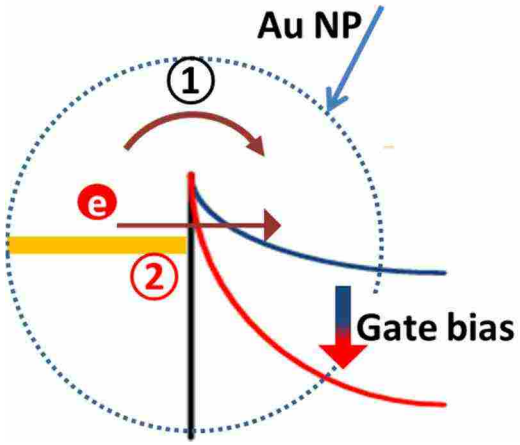

Figure 3.6 band diagram of plasmon FET a) with/Without gate voltage. With the applied gate voltage. Quantum tunneling effect in Au/ZnO/SiO2 structure increases because gate voltage causes thinner barrier and enhances the tunneling efficiency.

Gate voltage of FET device plays an important role in the efficiency of how many hot electrons can migrate to the ZnO layer or, in other words, how big, the plasmon energy can be detected directly. The electric field generated by gate voltage brings more electrons inside FET current channel through drift current mechanism ($J_n = qn\mu_n E$) where J is current density, q is a charge of the electron, n is a number of electrons, μ is electron mobility and

E is electric field [62]. Higher gate voltage causes modification of conduction band layer edge in semiconductor side (ZnO). Therefore, the wall thickness between carriers in the metal side and semiconductor decreases. This phenomenon is more notable when the carriers in the metal side do not have enough energy to jump over barrier height. So the only mechanism for them to be transferred inside ZnO layer is quantum tunneling, and gate voltage increment causes a higher tunneling efficiency due to wall thickness shrinkage.

The working principle, Schottky junction based internal hot-electron emission, was reported few decades ago [2, 66]. The photons that are absorbed in a metal contribute to generating 'hot electrons' and, if the hot electron energy is high enough, the hot electrons can overcome the Schottky energy barrier at the boundary between metal and semiconductor. Therefore, the hot electrons can move to the semiconductor, resulting in photocurrent. The reported works have shown that the generated current reflects exactly the plasmonic absorption in the metal nanostructures [3, 15, 64]. However, all those demonstrations show very low responsivity (A/W) or external quantum efficiency due to the limited absorption in the thin metal structure and inefficient hot electron diffusion from metal to semiconductor. Up to now, the best internal quantum efficiency (IQE) is 0.2% under no voltage bias condition [1, 60, 63]. Besides the low efficiency issue, the reported Schottky junction based plasmon detectors have a device structure that has the electrically connected plasmonic electrode structure. It limits the plasmonic structure design and requires complex fabrication process. Another issue of the Schottky plasmon detector is the limited detectable energy (lowest photon energy) due to the Schottky barrier height, while this plasmonic metal nanostructures can absorb the photon energy beyond the semiconductor bandgap energy. Therefore, it is needed that a novel device design that can

extend a detection spectrum beyond the mid-IR wavelength by taking the advantages of the plasmonic nanostructures.

Plasmon FET combines a conventional transistor structure with noble metal NPs. The results of this combination create a device with novel properties. Basically, plasmon FET is a bridge between electronics and plasmonic since it converts the plasmonic energy to an electric signal. The novel device is sensitive to any LSPR parameters such metal composition, nanoparticle size and surrounding refractive index of NPs. Such sensitivity enables potential applications which we are going to discuss in the next section. We have discussed about the working mechanisms of the plasmon FET and the Schottky junction diode based plasmon energy detection. The detailed experimental studies to confirm the working principles will be discussed in the following chapters.

Applications of plasmon FET

- plasmonic sensing and amplification

Plasmon field effect transistor can provide the information of the plasmonic response of the metal nanostructure in a very simple and robust way. It also converts the optical detection to the electrical signal, which makes easy for further read-out process. Including the signal amplification properties, plasmon FET has a great advantage as a sensing platform. The direct electrical signal conversion eliminates the bulky optical instruments and the amplification mechanism can tackle the noise issue by increasing the signal to noise ratio (SNR).

Plasmon FET is also capable of sensing plasmonic related parameters such as nanoparticles sizes, shapes, compositions and changes in surrounding refractive index.

These changes of the nanostructures turn out the change of plasmonic absorption spectrum. Then the change of plasmonic absorption can be monitored as an electrical signal using plasmon FET. The different shapes of NPs have different absorption spectra. Nanospheres only show one peak in the spectrum since it has zero dimension, while nanorods have two district peaks because its asymmetry confinement (or resonance) structure. Thus, we can detect different geometries of nanoparticles which used as a source of LSPR regarding the fact that the spectral response of plasmon FET matches the absorption spectrum of nanoparticles.

- Biological application

Since plasmon FET is sensitive to the changes of surrounding refractive index around gold NPs, it could be a valuable candidate to for antigen-antibody bonding sensing. The idea comes from the fact that if a gold nanoparticle is functionalized with some specific antigen and the specific antibody for that antigen attached to its pair, then the total average refractive index around the gold NP will be changed. This causes the absorption spectrum modification which means different plasmonic spectrum properties. These changes could be detected by plasmon FET. Figure (3.7) shows the basic Idea. As it can be seen, attaching molecules to the NPs cause a red shift in the absorption spectrum. As we discussed in chapter 2, the attached molecules, which have higher refractive index than air n>1, increases the effective refractive index on the gold surface, resulting in a red shifted absorption peak and slightly broader full width half maximum of the plasmonic absorption spectrum.

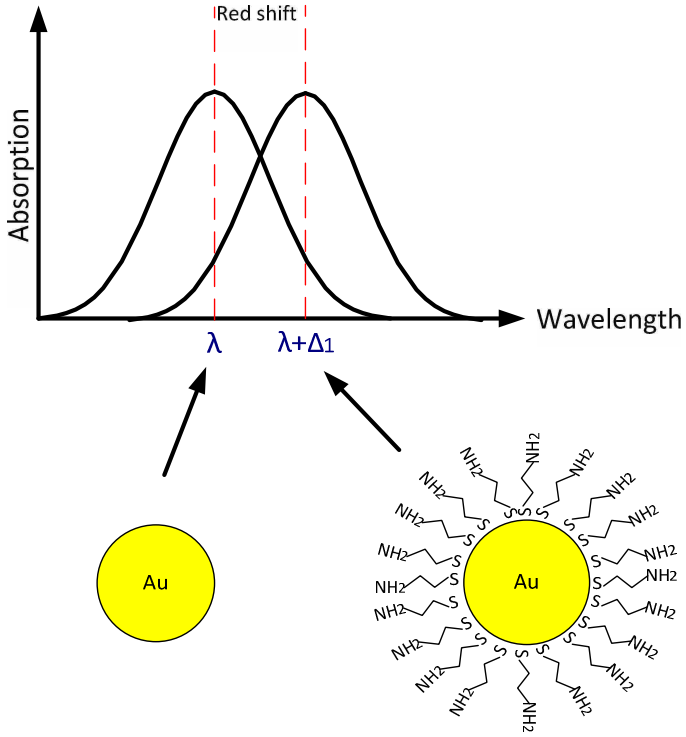

Figure 3.7 absorption spectrum red shift due to attaching a linker to gold NP. Since the refractive index around gold NP increases.

Using the same principle, antigen-antibody bonding could be simply detected using plasmon FET. As we emphasized earlier, the readout of the Plasmon FET is based on the electrical current that changes by the number of hot electrons from the plasmonic absorption. Therefore, plasmon FET sensing platform can eliminate the use of complicated optical geometry. Comparing our proposed sensor with conventional sensors, where SPR sensors detect antigen-antibody bonding, our novel sensor has simpler configuration and its capable of integration and multiplexing. Figure (3.8) shows the basic geometry of SPR sensors for biology purposes. This type of sensors uses surface plasmon effect to detect biological interactions. Briefly, if any interaction happens the surface plasmon angle will

be shifted slightly. Based on changes in the surface plasmon angle, the biological interactions could be detected. In this figure, dextran linkers are used to functionalize the gold film surface. These linkers could be used to grab antigens which could be attached to one specific antibody pair. The plasmon FET uses a smaller amount of analyte to detect the target because first it has better target mass per unit surface area and second the area of functionalization could be very small [14, 29, 70, 71].

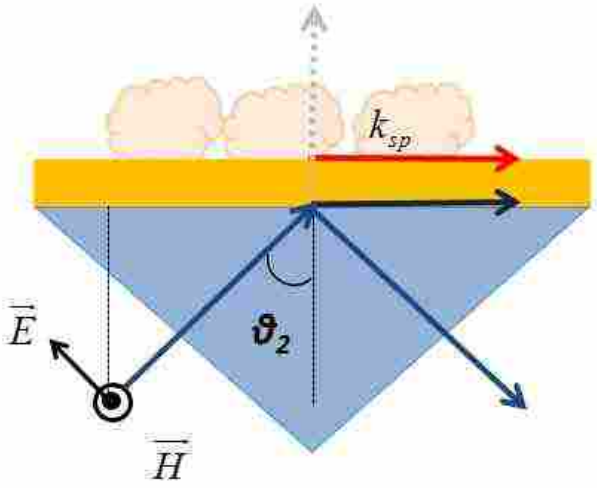

Figure 3.8 typical surface plasmon resonance sensor for biological application. Dextran linkers are used to functionalize the gold film surface. These linkers could be used to grab antigens which could be attached to one specific antibody pair.

- VIS-IR detectors

Plasmon FET is a decent candidate for VIS-IR detection. Since nanoparticles on top of the transistor channel could be replaced with other nanoparticle shapes, plasmon FET could be used to detect IR range frequencies. As mentioned in chapter 2, nanorods have two dimensions which provide two distinctive peaks in the absorption spectrum. These peaks could be detected by plasmon FET. Therefore, we can tune the absorption spectrum of

nanorods in IR region by changing the length and aspect ratio of nanorods,. As a result, the spectral response of plasmon FET will be located in IR frequencies and it can be used as an IR sensor that does not rely on the semiconductor bandgap [13, 22, 28, 68].

Summary

In this chapter, we discussed the plasmon field effect transistor and related physics to understand the working principles. Plasmon FET is a hybrid device that consists of thin film transistor and incorporated gold NPs. This novel structure can detect and amplify the plasmon energy and does not require complicated optical geometry for surface plasmon energy detection. Also, due to the amplification process, the plasmon FET offers better SNR in compare with Schottky junction based devices for LSPR Energy detection. The electrically isolated gold NPs structure is one of the advantages that enables functionalization for biomedical applications.

Chapter 4

Fabrication of plasmon field effect transistor

In this chapter, the fabrication method of plasmon FET will be discussed. We prepared a ZnO film on top of the heavily doped Si substrate which has a thermally grown silicon dioxide layer. After substrate preparation, we carried out typical cleanroom fabrication processes, such as photolithography, metal deposition and dry/wet etching, to create thin film transistor. Finally, gold nanoparticles are incorporated by using a self-assembly method. The fabrication details will be discussed in the following sections.

Substrate preparation

Figure (4.1) shows the substrate layers of plasmon FET. Two different types of FETs were fabricated. The first one was on the Silicon substrate where the heavily doped silicon layer was used as a back gate for the transistor. The other samples were fabricated on top of the glass substrate that is covered with a thin ITO layer which serves as a gate electrode. The first Si based device was fabricated as following processes. A 100nm SiO_2 film was predeposited on top of the Si wafer using a thermal oxidation process to create a dielectric layer for Gate bias. A thin n-type ZnO film (30, 50 and 100nm thickness) was then deposited using a RF sputter machine to create an active semiconductor channel. Ar ambient was maintained at 5 mTorr pressure in the chamber, and the substrate temperature was controlled to maintain 250 ˚C while the deposition process was carried out at 300W RF source power. The deposition rate was modulated to be 7.3nm/min, while the substrate was rotated for uniformity.

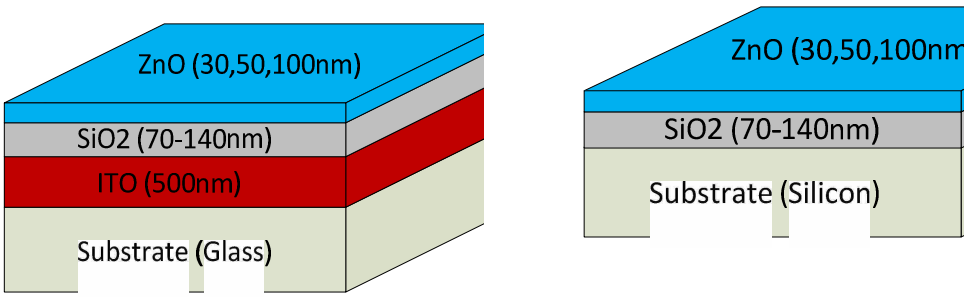

Figure 4.1 substrate layers of plasmon FET on glass (Left) and Silicon (Right). The ITO and the ZnO was grown using sputtering and SiO_2 was fabricated using PECVD.

Photomask design

The photomask for the photolithography process was designed using layout2009 software. In this design, different W/L ratios were considered for FET structures. We also considered an opening on top of ZnO channel for gold nanoparticles incorporation. This opening is isolated from drain and source connections because we want the gold NPs to be electrically isolated from source and drain electrodes. As it shown in the following figure (4.2) transistors with W/L ratio of 50/5, 50/10, 20/5, 20/10 and 20/2 um/um were designed.

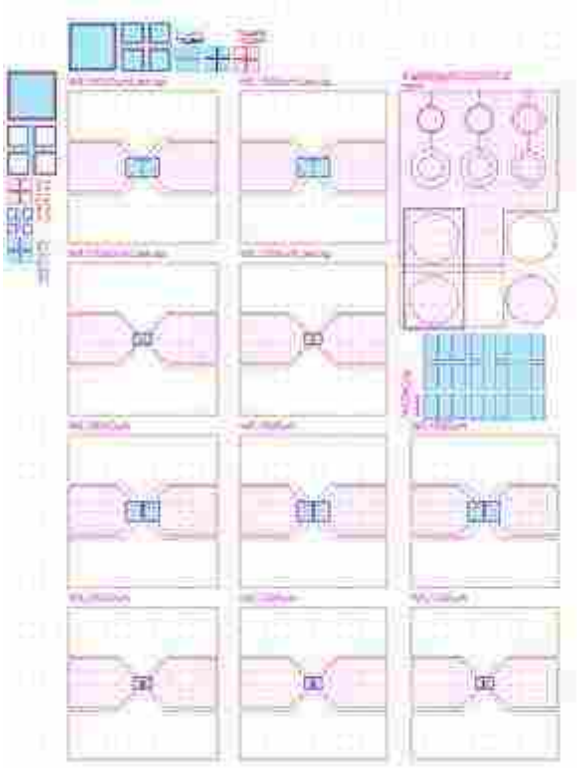

Figure 4.2 mask design for plasmon FET

Photolithography and wet etching

The ZnO layer was patterned using typical photolithography and wet etching processes. Figure (4.3) shows the ZnO etching for channel patterning. The following steps are used to pattern ZnO channel:

1. Photoresist (PR) Spin coating-AZ52114E (4000rpm/30s)
2. Heat treatment (2min/95C°)
3. Exposing (7s)
4. Developing –A2399MIF (25s)

5. ZnO Etching (HCL:DI/1:500) for 10s depends on ZnO thickness

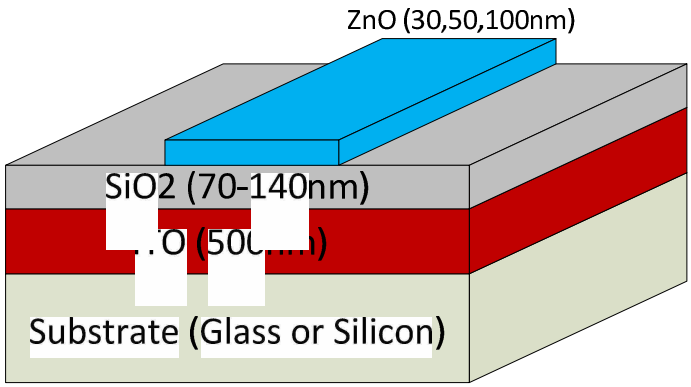

Figure 4.3 channel patterning on ZnO layer

After channel patterning, the following procedures were used to create source and drain contacts which are shown in figure (4.4).

1. PR Spin coating-AZ52114E(4000rpm/30s)
2. Heat treatment (2min/95C)
3. Exposing (7s)
4. Extra heat treatment and exposing for changing polarity purpose (2min-120C/60s)
5. Developing –A2399MIF (25s)
6. Metal deposition (AL-Au/500nm-300nm)
7. Cleaning (Acetone/Methanol/DI Water-5/5/5min)

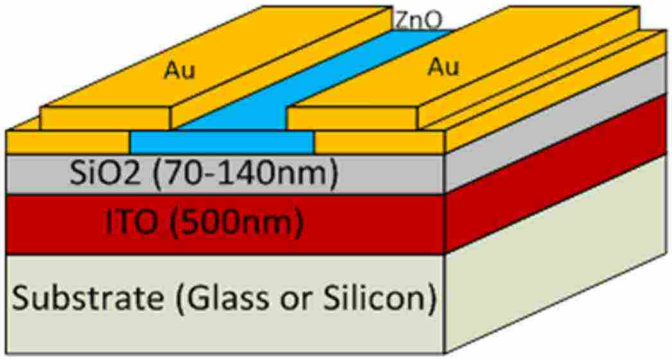

Figure 4.4 drain-source patterning and metal deposition to make ohmic contact (Ti/Au)

To create Drain and Source electrode contacts on the ZnO film, Cr/Au layers were deposited on the photoresist patterned substrate using an electron beam evaporator. After the lift-off process, the device becomes a fully functional field effect transistor (FET). Then, we carried out a characterization for the electrical properties of the FET device before gold nanoparticle incorporation on the ZnO layer. Figure (4.5) shows the final fabricated field effect transistor on the glass substrate with a size of 1x1 inch (left) and microscopic picture of FETs on a silicon substrate (right).

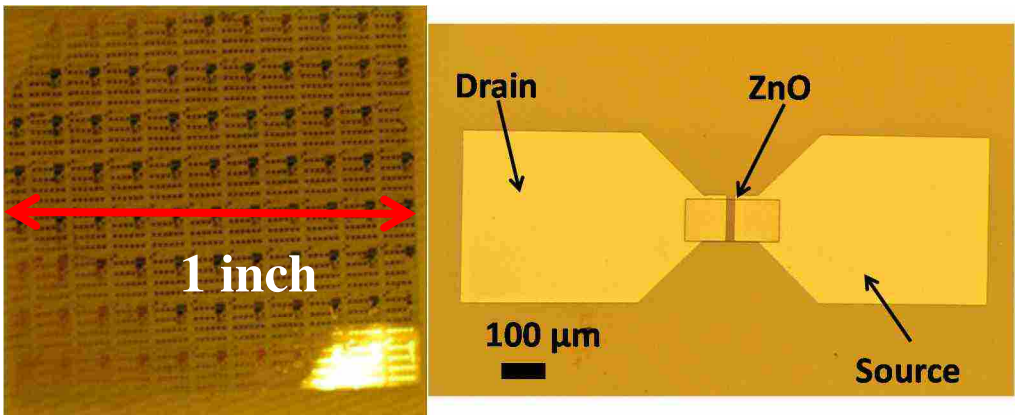

Figure 4.5 fabricated FET transistors on Left) glass and Right) silicon substrate

I-V characteristics of fabricated FETs

Figure (4.6) shows the I-V characteristics of typical fabricate FETs. As it can be seen from this figure, fabricated FET has a typical transistor characteristic. The drain-source current range is about 20μA in the saturation mode. Also, the I-V curve in the saturation mode shows very low slope, which means the initial electrical properties of the fabricated thin film transistor is almost ideal.

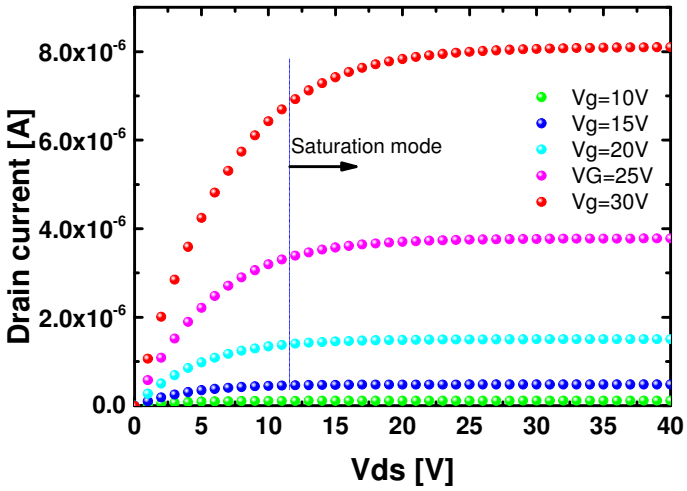

Figure 4.6 I-V characteristics of typical fabricate FETs

Gold nanoparticles incorporation

Finally, gold nanoparticles were added on top of the ZnO channel using a thermal reflow method to create self-assembled gold nanoparticle structures on the ZnO layer. Several reflow conditions were examined to control the size distribution of gold nanoparticles, and the best results were obtained with a 5nm thin gold film with 320˚C of heat treatment for 10 minutes. The size distribution and the shape of gold NPs play an

important role in plasmon FET, and the details of this will be discussed later in chapter 5, the spectral response of plasmon FET matches the absorption spectrum of gold NPs on top of ZnO layer. To investigate and analyze the incorporated gold NPs size distributions and shapes, we have carried out further investigations such as scanning electron microscopy (SEM), atomic force microscopy and absorption spectrum measurement. And these results will be discussed in the following sections.

Scanning electron microscopy analysis

Figure (4.7) shows the SEM picture of gold NPs on top of ZnO layer. A side view of a fabricated plasmon FET, gold nanoparticle sizes and ZnO layer thickness are shown in figure (4.7-10) respectively.

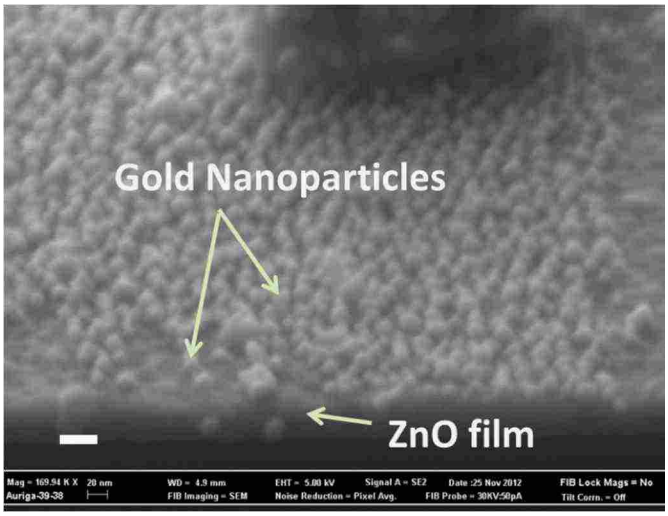

Figure 4.7 SEM image of fabricated field effect transistor including gold NPs on top of ZnO layer

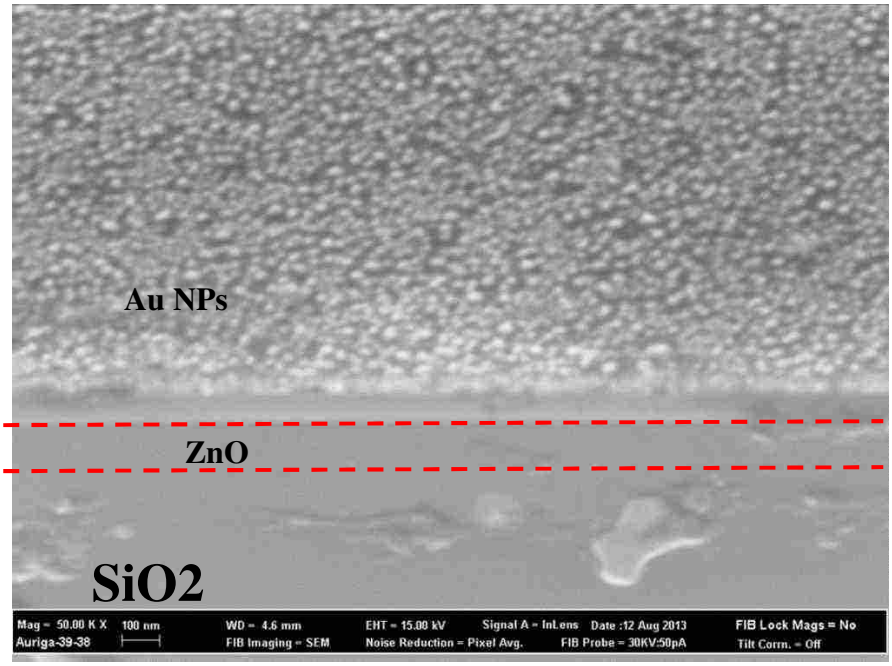

Figure 4.8 SEM picture of fabricated plasmon FET with Au NPs on top (side view). Between dashed lines is the ZnO layer.

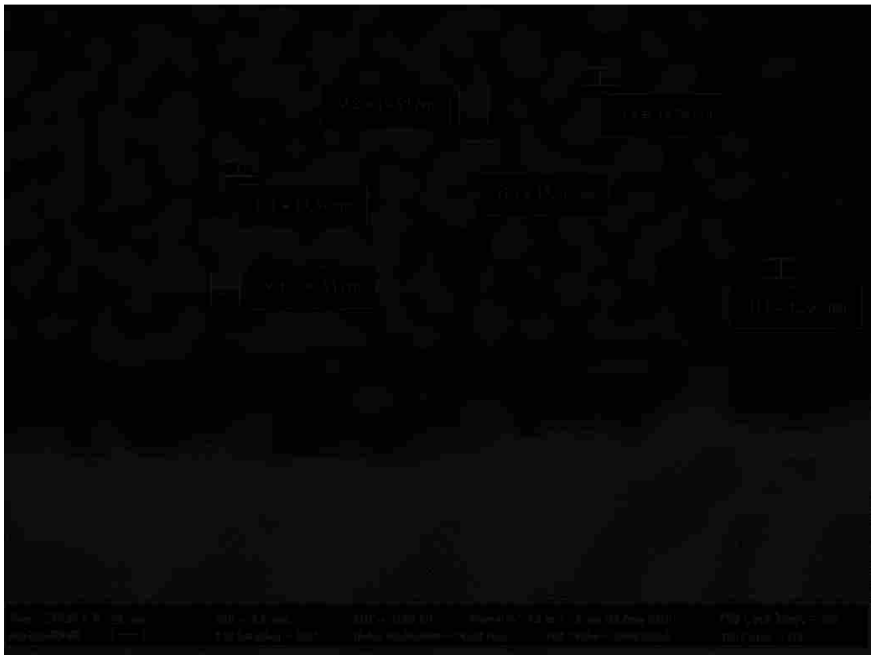

Figure 4.9 SEM picture of gold NPs on top of ZnO channel. Different sizes could be measured from 10nm to 20nm.

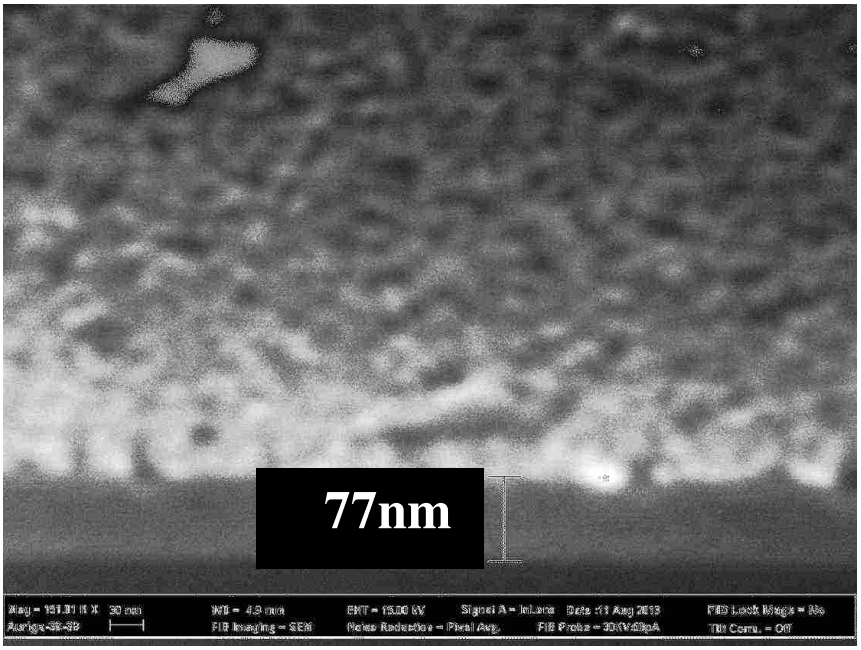

Figure 4.10 SEM picture of plasmon FET (side view). The measured ZnO layer thickness is around 77nm. Low contrast is because of tilted sample.

Based on the SEM analysis, the size of gold nanoparticles could be in the range of 8-20nm. The size distribution of gold NPs could also depend on substrate condition and metal film thickness. To investigate this dependence, we fabricated plasmon FETs with different thicknesses of the passivation layer (HfO_2) between gold NPs and ZnO layer. The AFM studies of these samples are explained in the next section.

Atomic force microscopy analysis

Atomic force microscopy was carried out to study the gold NPs size distribution on top of plasmon FET and the results are shown in figure (4.11). As it is shown in this figure, the shape of NPs is not ideally spherical. AFM statistics shows that particles size on top plasmon FET is in the range of 7-15nm. Considering the self-assembly process to fabricate NPs as well as AFM result, it could be realized that gold NPs on top of our device are more

semi-sphere shape also they are in contact with each other at the base level. Therefore, it could be concluded that the plasmonic spectrum captured by the device is broader than it is expected and also the spectrum could have a different profile with different light incident angels which are going to be discussed in next chapter. AFM studies also showed that the substrate condition could change the size distribution of gold NPs. In this study, we analyzed two plasmon FET structures with a different thickness of the passivation layer between gold NPs and ZnO layer (5,25Å). The result is shown in figure (4.12). From the measured results, we observed that the thinner HfO_2 passivation layer results in the larger nanoparticle sizes. According to figure (4.12) the average size of gold NPs in the sample with 5Å of HfO_2 layer is about 5.7nm while the sample that has 25Å of HfO_2 shows the average particle size of 4.1nm. We will confirm this study in Chapter 5, when we measure the spectral response (A/W) of plasmon FETs with different thickness of HfO_2 layer. The spectral response measurements show a clear blue shift while the passivation layer becomes thinner. It can be concluded that the blueshift in spectral response is because of the smaller size of gold NPs. In addition to the substrate condition, the initially deposited thin metal film thickness is a very important parameter to control the nanoparticle sizes using the self-assembly method. In the following section, we will discuss details of the absorption spectrum of fabricated gold NPs with different thicknesses of the metal film.

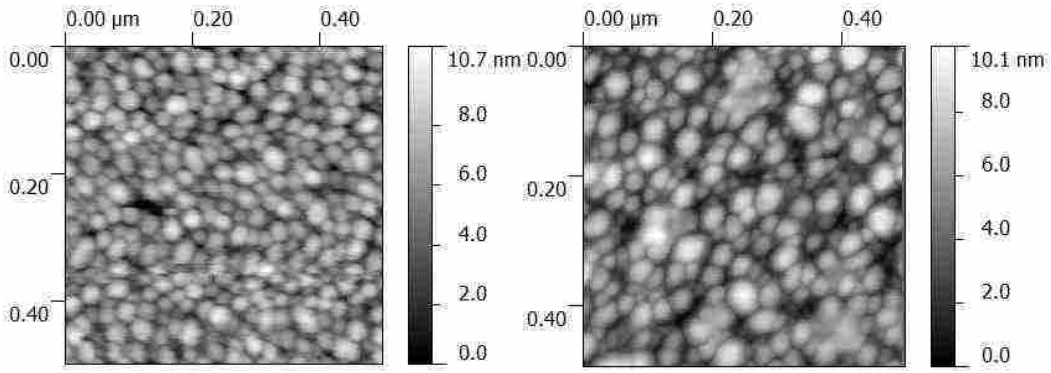

Figure 4.11 AFM of gold NPs on top of FET channel with (a) 25A (b) 5A of HfO2 thickness

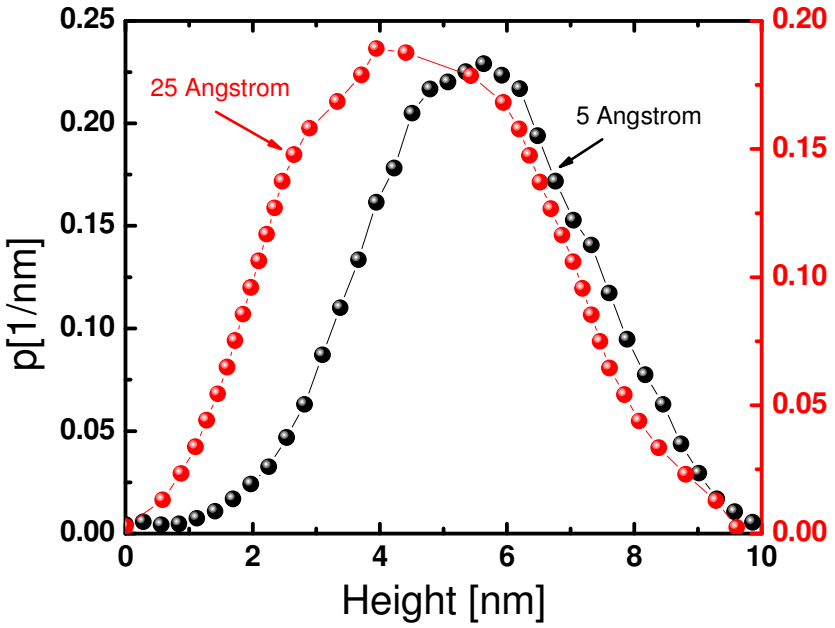

Figure 4.12 Height Distribution of top plasmon FET with 5,25A thickness of HfO2

Absorption spectrum of gold nanoparticles

The size of gold nanoparticles relies on the metal film process and substrate condition. The AFM results from the previous section showed that the substrate condition could change the gold nanoparticle sizes while the metal film condition and self-assembly

process are same. In addition to the type and thickness of the substrate, the metal film thickness is also a parameter that can change the nanoparticle sizes. Following figure shows the absorption spectra of different thicknesses of the thin gold films (3, 5, 7nm). And the self-assembly process was carried out under the same temperature and time conditions. As it is shown in the figure, once the metal deposited gold film thickness increases the absorption spectrum becomes broader, and it also experiences a red shift. This result shows that the resultant gold NPs have different sizes with different thicknesses of a metal film (the thinner film makes larger nanoparticles) under a constant self-assembly method (temperature and time).

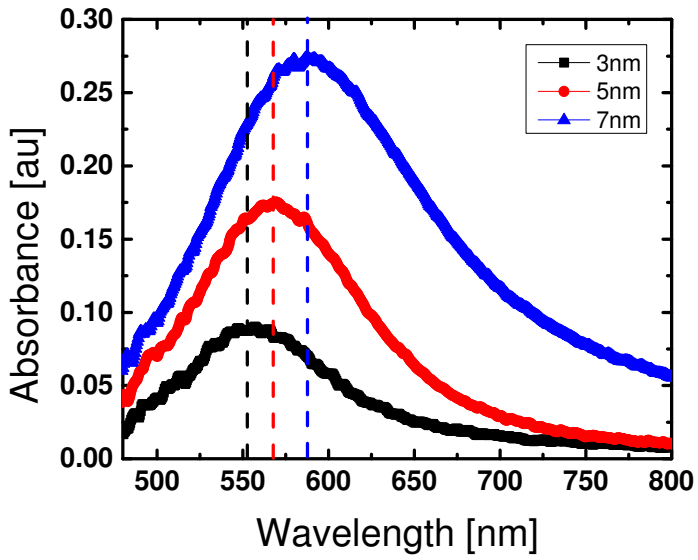

Figure 4.13 the absorption spectrum of gold nanoparticles with different thicknesses of thin film (3,5,7nm)

Fabrication of plasmon FET for bio-applications

To use the plasmon FET as a bio sensor, the InGaZnO (IGZO) was used as a channel layer. The IGZO is transparent (wide bandgap) semiconductor like ZnO but it is more resistant to buffer liquids than ZnO. Based on our experiments, PBS caused a lot of damages to ZnO layer however IGZO did not change upon exposing to PBS solution. Therefore we choose to use IGZO instead of ZnO to fabricate plasmon FET as bio-sensor. The fabrication procedures follow the same steps as we discussed earlier din this chapter. Briefly, a heavily doped p-type silicon (<100>, Boron doping level: ~ 10^{20} cm^{-3}) substrate was prepared by cleaning procedure (Aceton/Methanol/ DI water). Followed by 50 nm SiO2 film formation on the Si wafer using a thermal oxidation for a gate oxide. For the channel layer, a thin n-type InGaZnO (IGZO) film (30nm thickness) was then deposited using an RF magnetron sputtering using an IGZO target (2 inch size and 99.99% of purity) applying 90 Watts of RF power under 6.2 mTorr Ar ambient at 25^{o}C of substrate temperature. The deposition rate was 0.8 nm/min, while the substrate was rotated to achieve thickness uniformity. For the channel isolation, the IGZO layer was patterned using a typical photolithography process and a wet etching process using diluted HCl solution (2%). To create an Ohmic contact between Drain/Source electrodes and the n-type IGZO film, Cr/Au layers were deposited using electron beam evaporation. After the lift-off process, the device is a fully functional field effect transistor (FET). The fabricated FET devices were characterized regarding their electrical performance before gold NPs were incorporated into the active layers. Finally, gold was added on top of the IGZO channel using a thermal reflow method to create self-assembled gold nanoparticles. Several reflow conditions were tested to achieve a narrow size distribution and to optimize the semi-

spherical shape of gold NPs. Best results were obtained with a 5 nm gold film treated at 320˚C for 10 minutes. The dimensions of the fabricated devices were 100 µm and 50 µm of channel length (L) and width (W), respectively. Also the open area onto which the Au NPs were assembled was 30 µm × 100 µm. As shown in figure (4.14), a new mask has been designed to with three different size of plasmon FET (100µm×100µm, 50µm×100µm and 20µm×100µm).

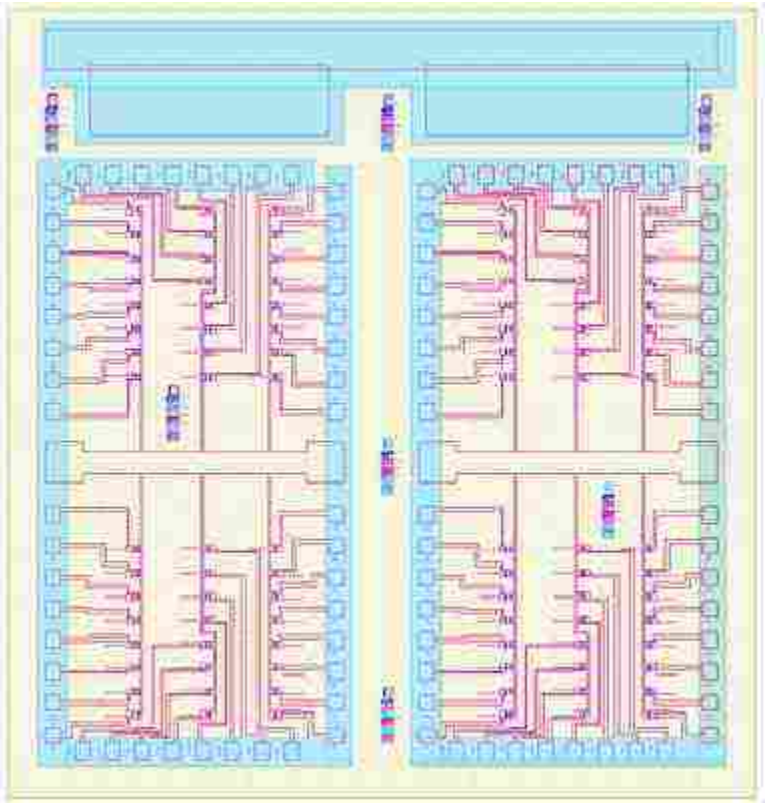

Figure 4.14 the mask design for bio compatible plasmon FET sensor. The designed plasmon FETs have three different sizes (100µm×100µm, 50µm×100µm and 20µm×100µm). The microfluidic channel can be fabricated on top of sensors (the total mask size is 1 inch x 1inch).

This design is compatible to integrate with microfluidic channels as well. The drain and source connection are placed at the edge of the chip. Thus the microfluidic channels

can be mount on top of the device. The fabrication of microfluidic channels will be explained later in this chapter. The images of the device structure using an optical microscope and a scanning electron microscope (SEM) are shown in the figure (4.15).

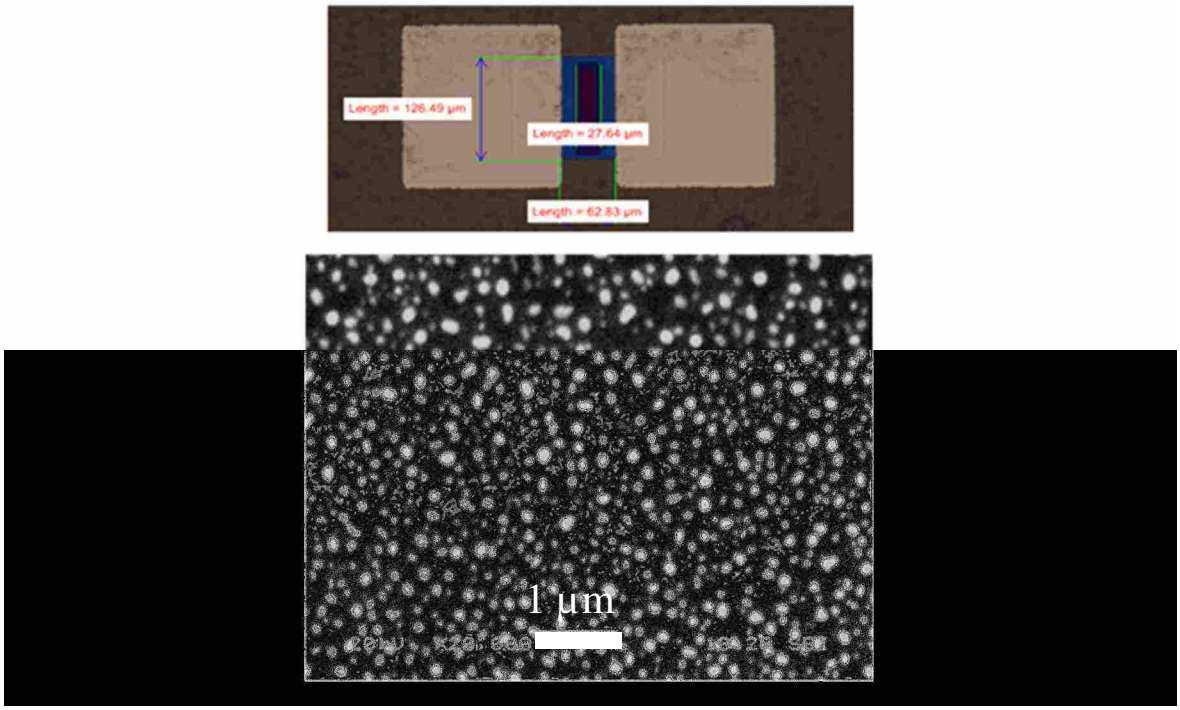

Figure 4.15 the micrograph of plasmon FET (top) and the SEM picture of self-assembled gold NPs.

Microfluidic channel fabrication

To fabricate microfluidic channels the mold was prepared using Su-8 2075. To define the recipe for the Su-8 the following table was used to tune the processing parameters on Si wafer <100>. The resultant developed Su-8 had 71 µm thickness. The thickness was measured using the step profiler. Figure 4.16 shows the microfluidic channel mold pattern on top of Si wafer. In addition, the following process was done to fabricate the microfluidic channels:

1. Prepare PDMS (Polydimethylsiloxane) molding solution

   -Mix Sylgard 184 Base / Curing Agent in a 10(base, 25g) : 1(curing agent, 2.5g) Ratio by weight for 15 mins.

2. Remove all bubble from molding solution (PDMS)

   -Put the PDMS in Vacuum Chamber

   (Vacuum 25 psi for 15mins twice)

3. Molding

   -Put a wafer with pattern in a petri dish

   -Pour PDMS on the wafer

   -Remove bubble again by using pipette (without vacuum chamber)

   -Put the petri dish on an optical table

   -Wait for a day

4. Remove mold and Cut micro-fluidic patterned PDMS

5. Attach micro-fluidic PDMS on the device

   -Exposure the device to ozone for 30 mins

   -Put the PDMS on the device by using Mask Aligner

Table 4-1 recipe for Su-8 2075 development process

Spin Coating	First Step	Speed (RPM)	500
		Ramp (RPM/sec)	100
		Time (S)	10
	Second Step	Speed (RPM)	1900
		Ramp (RPM/sec)	300
		Time (S)	30
Pre-Baking	Stress removal @ 65'c	Temp ('C)	65
		Time (min)	6
	Baking @ 95'C	Temp ('C)	95
		Time (min)	20
Cooling to Room Temperature		Cooling time (min)	5 min
Mask Aligner	Exposure	Lamp Intensity (mW/cm2)	18.74
		Required Intensity (mJ/cm2)	600
	Time = [mJ/cm2] / [mW/cm2]	Time of exposure (s)	32.01707577
Post-Baking	Stress removal @ 65'c	Temp ('C)	65
		Time (min)	6
	Baking @ 95'C	Temp ('C)	95
		Time (min)	10
Cooling to Room Temperature		Cooling time (min)	5
Developing Step		Developer	su8 developer
		Developing time (min)	6 min
		rinsing material	Isopropanol + N2
Hard - Baking		Temp ('C)	105
		Time (min)	5 min

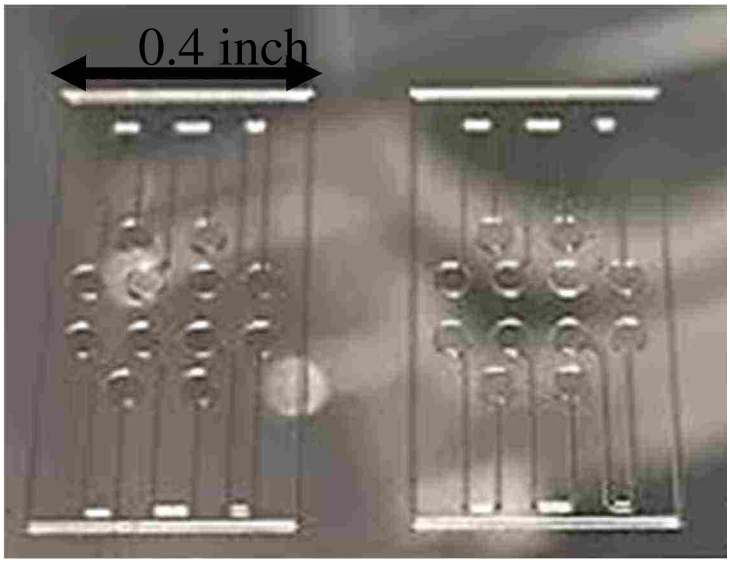

Figure 4.16 the fabricated microfluidic channel mold with Su-8 2075

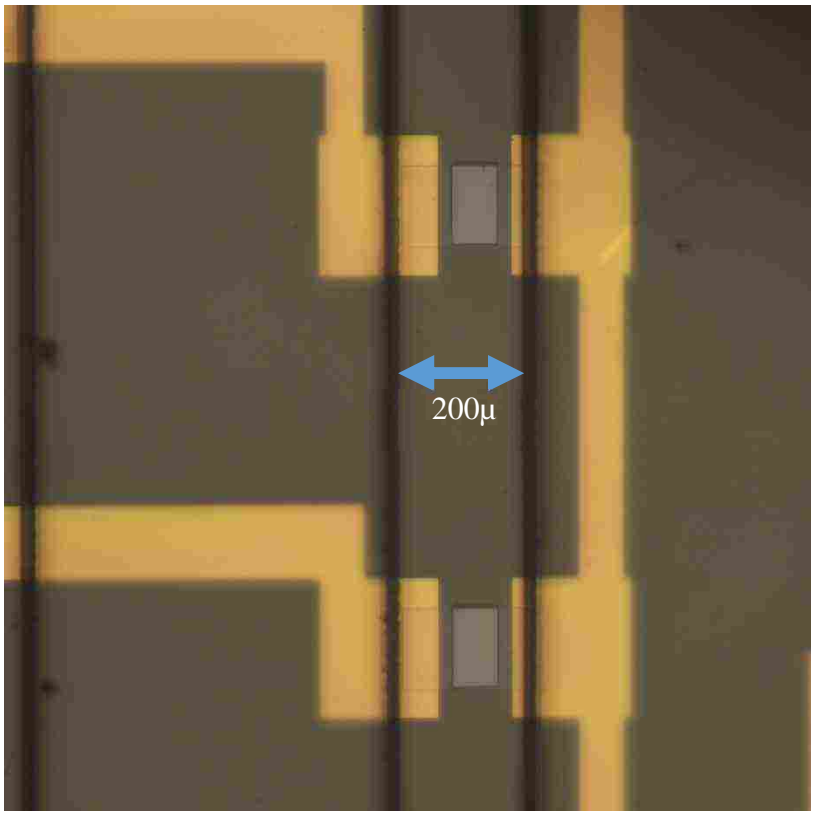

Figure 4.17 the fabricated microfluidic channel on top of plasmon FET

Figure 4.17, shows the fabricated device with microfluidic integrated on top of the device. The design has three different sizes if fluidic channel which matches the three different sensor sizes. The fluidic channels have the width of 80µm, 100µm and 120µm. The injection was done using the commercial needle which makes this device more suitable for mass production and industrial uses. In addition, this sensor can run by 5V which makes it a perfect choice to be connected through USB,

Summary

In this chapter, we presented the fabrication process of plasmon FET. The plasmon FET can be fabricated using conventional micro fabrication. The field effect transistors were fabricated successfully and the I-V characteristic curve showed that that fabricated FETs had the typical transistor response. The gold nanoparticles on top FET channel were fabricated using self-assembly method where the thin layer of gold baked at 300^{o}C. Using SEM and AFM pictures; we confirmed that the fabricated gold NPs have median sizes around 5nm. However, the nanoparticles sizes can be controlled by using different substrate conditions or metal film thicknesses. In addition, the IGZO-based plasmon FET was fabricated for biomedical applications. And at the end, the microfluidic base sensors was presented.

Chapter 5

Characterization of plasmon FET

In this chapter, we will discuss the properties and characteristics of plasmon FET with different sets of experiments. These studies will include spectral responses, electrical and plasmonic properties of the plasmon FET. By carrying out these experiments, we could have understandings how and why the plasmon FET can detect the plasmon induced hot electrons and produces the amplified detected signal. Even though we believe that there are still unexplored underlying physics of the plasmon FET, the discussed results in this chapter will clearly explain the basics operating theory of the plasmon FET.

We will start this chapter with explaining the characteristic of the Schottky Barrier height for ZnO/Au junction. The Schottky properties of Au/ZnO junction play an important role in the spectral response of plasmon FET because the generated plasmonic hot electrons have to overcome the Schottky barrier height to be able to contribute to FET drain current. Then we will explain the experimental setup that we used to characterize the plasmon FET. After introducing measurement setup, we will show the spectral response of plasmon FET under different conditions such as different gate voltages, thicknesses of ZnO, operating temperatures and light incident angles. In addition, some of the experimental results will be discussed with the simulation results.

Schottky Barrier height for ZnO/Au structure:

Schottky diode of Au/ZnO and Au/HfO_2/ZnO was fabricated to characterize the Schottky barrier height (Figure5.1). The device structure is Au (10nm)/HfO_2 (0, 1, 2, 3,4nm)/ZnO (800nm)/AZO (250nm)/Al (100nm) with 1 mm diameter of circular pattern. For diode fabrication, 100nm-thick Al was deposited on a Si substrate. Then AZO and ZnO deposited on the Al layer successively, forming Ohmic and Active layer, respectively. AZO between Al and ZnO prohibit Al diffusion and provide Ohmic property. RF magnetron

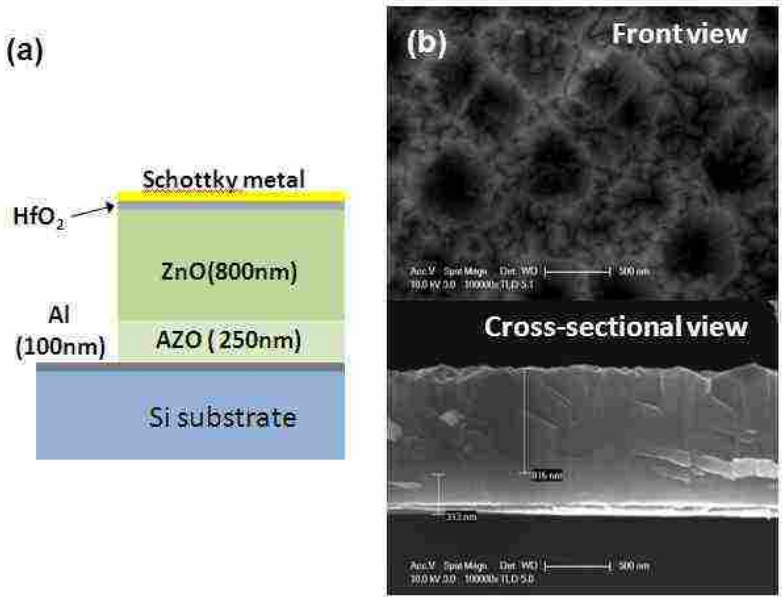

Figure 5.1 Schematics of Au/ZnO Schottky device structure of (a) Au/HfO_2/ZnO/AZO/Al having a ZnO MIS Schottky junction. (b)Front and (c) cross-sectional SEM images.

sputtering was used to deposit the ZnO and AZO films using a pure ZnO target (99.99%) and an AZO target (99.99% and 2at% of Al_2O_3 sintered). AZO and ZnO deposition were carried out with a 300W RF power and 250 ˚C of substrate temperature. Patterning of the diode structure was done by a photolithography process. An ultra-thin HfO_2 layer was deposited for the interface passivation using an atomic layer deposition (ALD) method at

the temperature of 120°C to create 0, 10, 20, 30, 40Å thick insertion layers. The gold deposition was followed by a thermal evaporation to create a Schottky junction. After performing lift-off process, the diode was isolated by HCl wet etching process that removes a portion of the ZnO and AZO to reach the back Al contact.

The current flow in a Schottky contact is determined by the thermionic emission theory, and the current transport of the metal-semiconductor contact involves mainly three modes of current transport: thermionic emission, thermionic-field emission and field emission. The current density for ideal thermionic emission is:

$$J = A^{**}T^2\exp(-\frac{q\phi_b}{nk_BT})(\exp\left(\frac{\mathrm{qV_a}}{\mathrm{k_B}T}\right) - 1) \quad (5\text{-}1)$$

Or by simplifying:

$$J = J_0(\exp\left(\frac{\mathrm{qV_a}}{n\mathrm{k_B}T}\right) - 1) \quad (5\text{-}2)$$

And

$$J_0 = A^{**}T^2\exp(-\frac{q\phi_b}{k_BT}) \quad (5\text{-}3)$$

Where A^{**} is the effective Richardson constant for the semiconductor (for ZnO, $A^{**} = 32\frac{A}{cm^2K^2}$, T is the absolute temperature (300K), q is charge of a single electron, n is the ideality factor, k_B is the Boltzmann constant, and V_a is the applied voltage [72, 73]. When $V_a \geq (3k_B * T)/q$ under forward bias, equation (5-1) could be modified as:

$$J = J_0\exp\left(\frac{\mathrm{qV_a}}{n\mathrm{k_B}T}\right) \quad (5\text{-}4)$$

The ideality factor value for an ideal rectifier is n≈1, indicating the dependency of the bias voltage and the Schottky barrier height. When the current is dominated by thermionic-field emission instead of thermionic emission, the ideality factor can significantly exceed unity [72]. Large ideality factor can also be caused by interface states and recombination centers [72]. For a non-ideal or real Schottky contacts, the current density can be expressed with the inclusion of a series resistance effect:

$$J = J_0(\exp\left(\frac{\mathrm{q}(\mathrm{V_a} - AJR_S)}{n\mathrm{k_B}T}\right) - 1) \tag{5-5}$$

Gold has a high work function with the range of around 5.1-5.47 eV (3), which is suitable for a Schottky junction formation with an n-type ZnO. Furthermore, an ultra-thin HfO_2 layer was introduced to study the insulator thickness dependency (i.e. quantum tunneling dependency) on the diode current [74]. Figure (5.2) presents semi-log I-V characteristics, which shows current rectification by Au/ZnO Schottky barrier. Inserting an HfO_2 layer decreased the current density of both forward and reverse bias region, but it shows better current rectification. Quantum tunneling enables diode current flow at the forward bias even with insulating the junction. At the reverse bias, thermally perturbed leakage components were effectively suppressed with the surface passivation effect. However, 40Å of HfO_2 thickness limits the forward current due to the high series resistance, and the severely insulated Au/ZnO junction shows a giant ideality factor value. It provides a strong clue about the current flow mechanism on Au/HfO_2/ZnO channel region of plasmon FET.

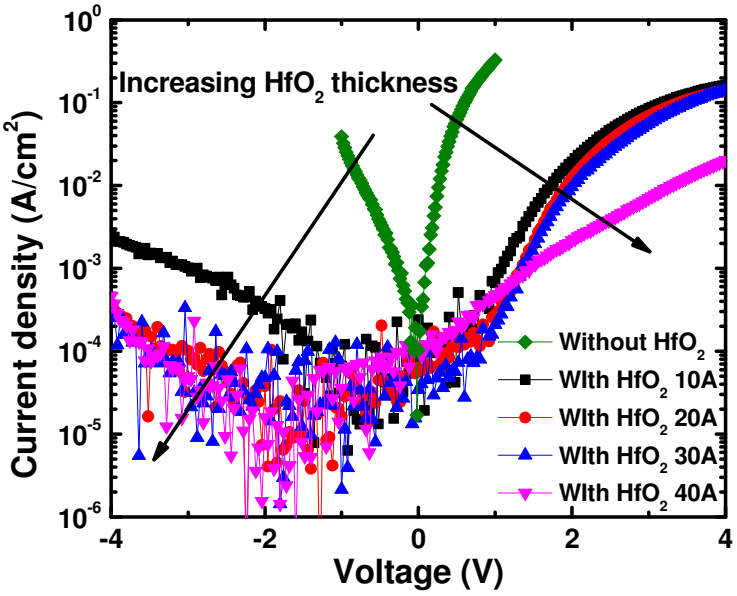

Figure 5.2 Semi-log I-V curve of Au/ZnO Schottky diode (Au/HfO2/ZnO/AZO/Al) with different HfO2 thickness(0-40Å)

Then, ideality factor, the dark saturation current and barrier height was extracted using equation (5-1-4). If we take the log both sides of the equation (5-2), it becomes:

$$ln(J) = ln(J_0) + \frac{q}{nk_BT} * V_a \quad (5\text{-}6)$$

This equation represents the equation for the linear portion of the ln(J)-V graph of y=mx+b, where $y = \ln(J)$, $b = \ln(J_0)$, $m = \frac{q}{nk_BT}$, and $x = V_a$.

From here, the ideality factor n can be derived:

$$n = \left(\frac{k_B T}{q} * m\right)^{-1} \quad (5\text{-}7)$$

and barrier height can also be derived, where:

$$\phi_b = -\frac{k_B T}{q}(b - \ln(A^{**}T^2)) \quad (5\text{-}8)$$

J_0, n, and ϕ_b were extracted using equation (5-6,7,8) and summarized in Table 1.If we simplify Equation (5-2), it becomes $J = J_0 exp(AV)$. The current transport mechanisms between ZnO/Au junction appears by combining diffusion, thermionic emission, generation and recombination, tunneling, and space charge limited current (SCLC). For the HfO_2 inserted Schottky junction, high ideality factor and high value of slope of log-log I-V curve indicates that the dominating mechanism is thermionic emission with effects of tunneling and recombination [75].

Table 5-1 Calculations from log (J)-V plot of Au/HfO_2/ZnO MIS Schottky diodes

Schottky diode of Au/HfO2/ZnO/AZO/Al			
Thickness of HfO_2 (Å)	Ideality factor n	Dark Saturation Current J_0 (A/cm^2)	Barrier Height Φ_b (eV)
0	1.9	1.2 x 10^{-4}	0.61
10	9.1	1.1 x 10^{-5}	0.68
20	8.8	3.3 x 10^{-6}	0.72
30	8.9	2.7 x 10^{-6}	0.72
40	20.8	7.6 x 10^{-5}	0.64

Experimental setup for plasmon FET

For the electrical characterization of plasmon FET, two source meters (Keithley 2400) are used to provide the Gate-Source and Drain-Source voltage biases. The spectral response measurement was carried out using a monochromatic light through a fiber-optic cable delivered on the sample with controlled angles at the probe station. The optical measurement system consists of a quartz tungsten halogen lamp (250W, Oriel), a lock-in amplifier (SR830, Stanford Research) with a mechanical chopper, a monochromator (SP2300, Princeton Instruments) and appropriate optical filters to suppress the second harmonic lights from the monochromator. The light power was measured using a NIST calibrated silicon photodetector (FDS-1010CAL, Thorlabs) and an optical power meter (PM100D with S120VC, Thorlabs) for the spectral response calculation. The measured monochromatic optical power was controlled from 0.7 to 2mW/cm2 for the 400nm-800nm spectral range. Additionally, a picoamp meter (Keithley 6485) was used to measure the drain current from unmodulated light illumination. A customized LabView program controls the monochromator, the lock-in amplifier and picoam meter for automated computerized measurements. The following figure shows the schematic of the measurement setup.

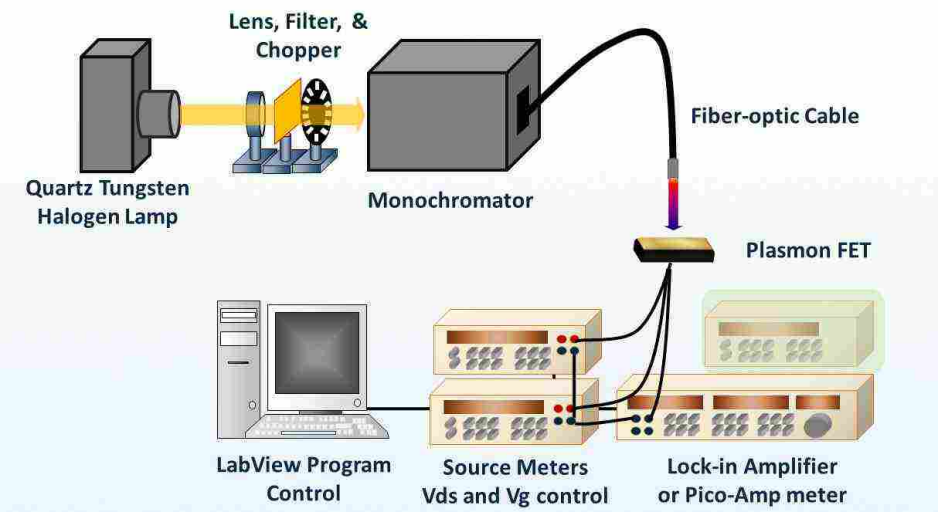

Figure 5.3 Measurement setup to obtain spectral response of plasmon FET

This experimental setup helps us to extract the optical response of plasmon FET. As it can be seen in figure (5.3), the chopper can modulate the incoming light to the monochromator. By using the modulation frequency of chopper and lock-in amplifier, we are able to extract only the optical response of our device. That means we can calculate the current enhancement in transistor due to optical excitation. In the next section, the spectral response of plasmon FET will be shown using our measurement setup. The spectral response of plasmon FET depends on plasmonic hot electrons inside gold nanoparticles at plasmon resonance frequency.

Spectral response of plasmon FET

As we mentioned in chapter 3, gold NPs on top of plasmon FET are a source to generate plasmonically induced hot electrons. The localized plasmonic resonance occurs at a specific wavelength, and it depends on size and shape of the NPs. In this study, we explored the plasmon FET response in the range of 400-800nm. Once plasmonic resonance occurs

inside Au NPs, the generated hot electrons have to overcome the Schottky barrier formed by Au/ZnO junction in order to allow a thermionic diffusion to the semiconductor region. Based on the work function difference between gold and n-type ZnO, it is expected that a Schottky barrier is formed with around 0.6-0.7 eV of barrier energy as we discussed in the previous section. Thus, the generated hot electrons at visible wavelength (400nm-800nm) can diffuse from gold NPs to ZnO layer. In terms of optical properties, the gold NPs with 5-10nm in radius exhibit strong plasmonic absorption around a wavelength of ~520nm. This absorption peak depends on the dielectric constant of host materials surrounding gold NPs and size of NPs. In order to avoid overlap of the absorption spectrum, we choose ZnO for the FET channel material. We confirm that the bandgap of 250nm-thick ZnO thin film is 3.3 eV and shows almost zero absorbance (<0.001%) at the spectral range between 450nm to 1100nm. Thus, it is expected that there will be no optical response in the drain current under illumination at any visible wavelength.

As discussed earlier, the plasmonic absorption generates hot electrons in gold nanoparticles and these energetic hot electrons can migrate across the Schottky barrier and diffuse to the ZnO film which is shown in figure (5.4). Consequently, this process supplies more electrons in the ZnO channel, resulting in increased channel conductivity and drain current (Id). Figure (5.5 shows the typical spectral response of plasmon FET. As it is clear in this figure, plasmon FET has a peak response around 600nm. We also did a direct measurement of transistor drain current without employing a lock-in amplifier. The results are shown in figure (5.6). The measured current using a picoamp meter shows the well matched plasmonic current. It should be noted that the measured current using amp meter does not reflect the pure contribution from the plasmonically induced hot electrons. The

value that can be seen in the figure is a summation of DC current level of the transistor and the contribution from the hot electrons absorbed in gold NPs.

Interestingly, the measured data shows that the amplitude of the hot electron induced drain current depends on the gate voltage bias. Under the saturation mode operation of the plasmon FET, the spectral response value, R(A/W) reached to larger than 3, which implies that an amplification process was involved, depending on the applied gate voltage bias. This efficient amplification can be explained by an energy band model. Without gate voltage bias, the plasmon induced hot electrons can migrate only with diffusion once they have high enough energy to overcome the Schottky barrier which is shown in figure (5.7). Due to the short mean-free-path in the gold and semiconductor structure, it is difficult to collect plasmon induced hot electrons with a lateral electric field across Drain and Source. When positive Gate voltage is applied to the plasmon FET, there will be the large potential difference between Schottky junction and gate oxide (Figure5.7b). This internal electric field created by gate bias facilitates electrons to move to the other boundary where the FET channel is located (process③ in figure (5.7)). The migrated hot electrons are seized by the gate voltage, consequently contributing to channel enhancement and to allow more drain current to flow (process④ in figure (5.7)). Therefore, the collected current from the device is proportional to the plasmonic absorption from the gold nanostructure but is not limited to the number of hot electrons generated in the metal. It should be noted that the free electrons in the gold nanostructure were not depleted after long time exposure to the light. This could indicate that there is a restoring force to recharge electrons back in gold NPs since nanoparticles are attached to the ZnO surface which has an electric field by drain-source voltage bias at their boundary, this effect will be explained later.

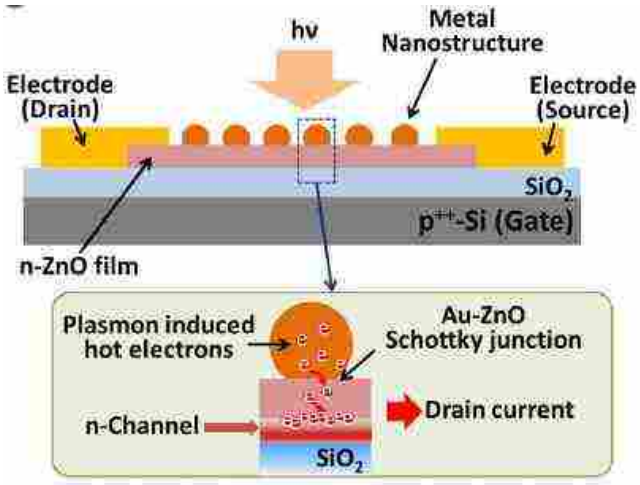

Figure 5.4 Operational principle of plasmon FET under light illumination. The plasmon induced hot electrons migrate from the gold nanostructure to ZnO channel and increase channel conductivity and drain current

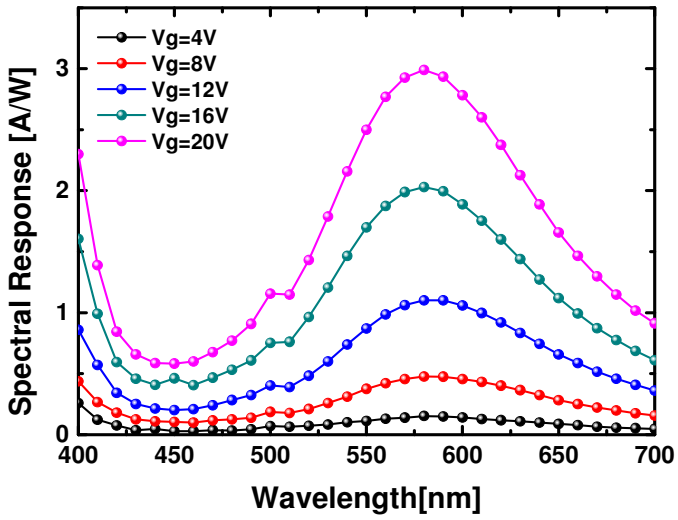

Figure 5.5 Spectral response of plasmon FET as a function of gate voltage bias

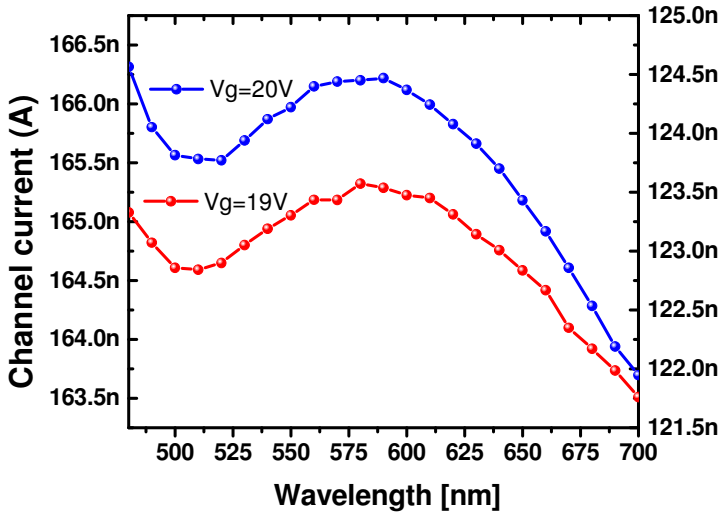

Figure 5.6 plasmon FET channel current using direct measurement

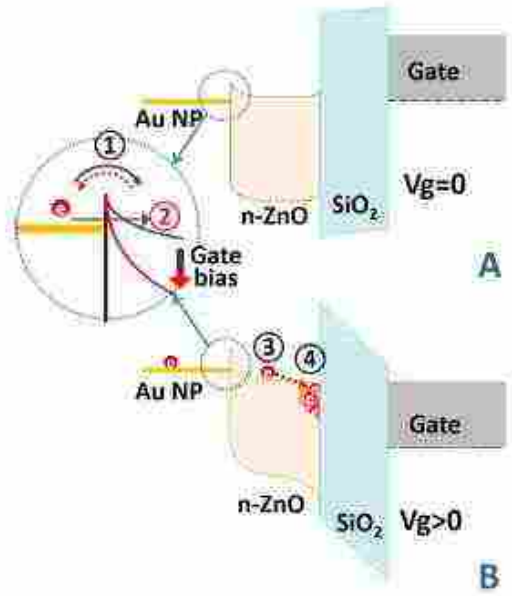

Figure 5.7 Gate voltage dependent ZnO energy band bending of plasmon FET and amplification mechanism. (a) Thermionic diffusion without gate bias. (b) Internal field assisted hot electron migration and quantum tunneling at the Schottky junction with gate voltage bias.

Study on free electron discharging

One of the questions on the working mechanism of the plasmon FET is how the gold nanoparticles can provide hot electrons without depletion when it was illuminated for a long time. If there is a substantial amount of electrons migrated, the gold nanoparticles could be depleted. Consequently, the plasmon FET cannot produce plasmonically induced drain currents, if there is no mechanism to refill the electrons. We carried out an experiment to check if the electrons in the gold nanoparticles can be depleted due to the hot electron migration. We continuously illuminated the plasmon FET and measured the drain current at near the peak wavelength of the plasmonic absorption (0.85mW/cm^2 at 550nm). Based on the calculation, the entire volume of gold NPs has total 3 x 10^{12} of free electrons by using the free electron density of gold (5.9 x 10^{28} /m^3). Using the spectral response (0.01A/W) without gate voltage bias, the number of the collected hot electrons from the gold nanoparticles are 8.9 x 10^{11} /s. Therefore, the estimated time to deplete the entire free electrons from the gold NPs under continuous illumination of light will be 3.37s. Therefore, several hours of continuous light exposure measurement to observe a depletion of the free electron in gold NPs is more than enough. The measured data in (5.4) shows that there is no change in plasmonically induced drain current. This indicates that there is a circuit to supply electrons to the gold nanoparticles while it loses plasmonically hot electrons. The sampling rate for data showed in Figure (5.8) is 10 seconds. After 1h dark condition, the light at 550nm was illuminated on sample continuously, and the drain current was stored at every 10 seconds.

There have been a report by Liu et al. regarding the plasmonically induced hot electron transfer and restoring mechanism. In this paper, they studied an Au/ZnO Schottky junction.

At the plasmon resonance condition, the generated hot electrons in Au NPs overcome the Schottky barrier and leave Au NPs positively charged which brakes equilibrium of Fermi level condition in Schottky junction. As a result, the low energy electrons will flow into Au NPs to compensate the Fermi level differentiation. It should be noted that the gold nanoparticles are not completely isolated from the FET although the nanoparticles are not directly connected to the three electrodes for voltage bias. Therefore, the junction area between ZnO and gold nanoparticle is under influence from the drain-source voltage bias as shown in Figure (5.9). The perpendicular electric field at the metal-semiconductor boundary can supply electrons to the gold nanoparticles while the plasmonically induced hot electrons move to the FET channel (by gate bias) or return to the adjacent gold nanoparticles (by drain bias). This possible mechanism can be supported by the drift current based plasmonic spectral response of plasmon FET under zero Gate voltage bias. We also collected the plasmonic induced hot electrons under drain-source voltage bias condition without gate voltage bias. In this case, we have a very low spectral response because the device does not amplify the plasmonic response. But the drain-source voltage bias collects plasmon induced hot electrons without depletion of the free electrons in gold NPs. This means there is a closed circuit between gold NPs and ZnO channel layer while they have an electric field by drain-source voltage bias. The calculation of contributed induced plasmonic hot electrons is shown in next section.

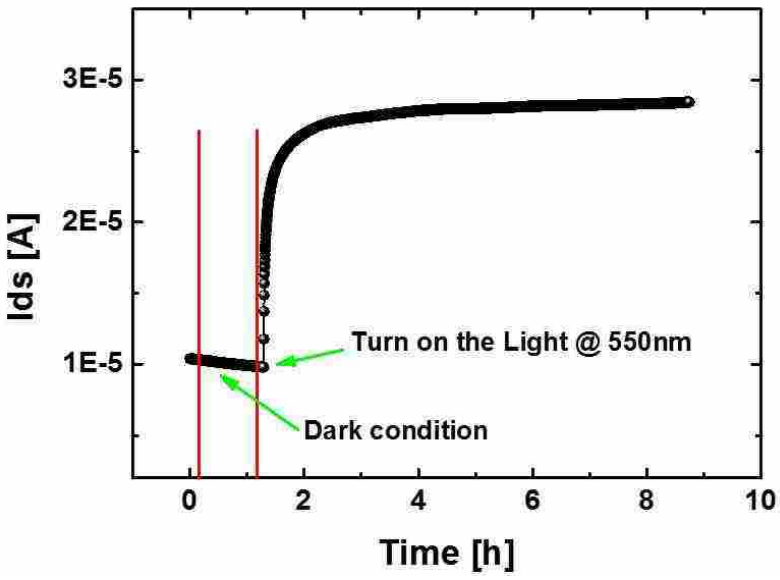

Figure 5.8 Drain current measurement of plasmon FET under dark and light

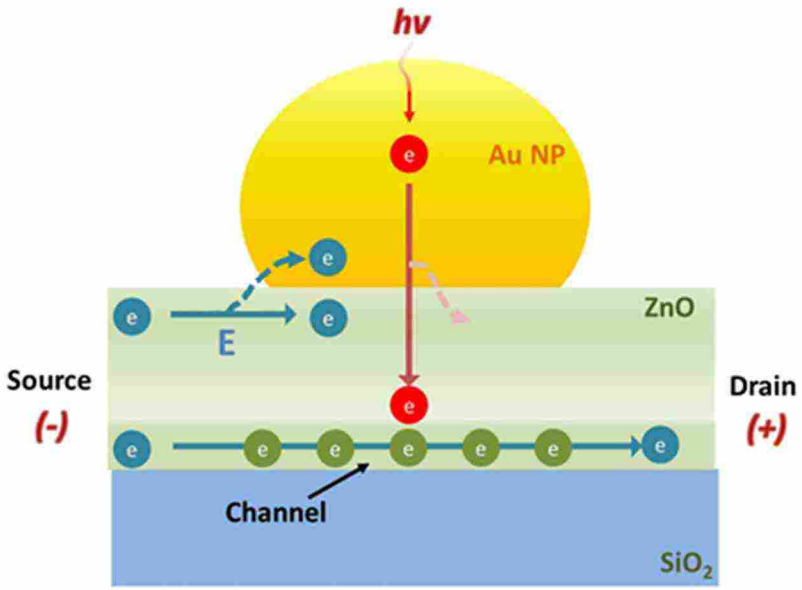

Figure 5.9 Low energy electrons supply mechanism in plasmon FET, under illumination conditions. The rough ZnO surface creates a complex E-field profile at the boundary and could contribute electron restoration for gold NPs.

Number of contributed hot electrons to the plasmon FET

To obtain the number of contributed hot electrons to the plasmon FET current channel form gold NPs, first the total number of photons absorbed by the gold nanoparticles was calculated at the peak wavelength (~580nm or 2.13eV). From the measured absorption spectrum of gold nanoparticles, it has approximately 22% absorption (α) at the plasmonic peak wavelength. The illuminated power density on the device (100μm x100μm) was 78.5μW/cm2 (ϕ_{in}). Therefore, the number of absorbed photons in gold NPs is,

$$n_{photon} = \frac{\alpha \cdot \phi_{in} \cdot A}{qh\nu} = \frac{0.22 \times (78.5 \times 10^{-6}) \times (10^{-2})^2}{(1.6 \times 10^{-19}) \times 2.13} = 5.05 \times 10^{9} / s$$

Then, the number of hot electrons that contributed to increased drain current was calculated. Since the transistor is operating at saturation mode, the FET drain current at saturation mode can be written as [76]:

$$\Delta I_{ds} = \frac{1}{2} \mu_n C_{ox} \frac{W}{L} (V_{gs} - V_{th})^2 \tag{5.9}$$

Where C_{ox} is capacitance per unit area ($\frac{\Delta Q}{V.Cm^2}$), μ_n is the mobility of electrons in ZnO layer ($\frac{Cm^2}{V.s}$)), V_{gs} is the gate-source bias voltage and V_{th} is the threshold voltage of FET. W and L represents the width and length of channel area in FET structure respectively.

Since the plasmon FET was under a large voltage bias condition (V_{ds}=20V and V_{gs}=20V), the small threshold voltage is neglected. Using the charge is the product of capacitance and voltage ($Q = C.V$), The increased drain current equation becomes:

$$\Delta I_{ds} = \frac{1}{2} \mu_n \Delta Q \frac{W}{L} * V_{gs}$$

Experimentally obtained electron mobility (μ_n) of ZnO TFT was 17 V.s/cm^2. And the measured drain current change (ΔI_{ds}) using lock-in amplifier was 23.4nA at 580nm.

Therefore, the increased charge (ΔQ) can be calculated as follow:

$$\Delta Q = \frac{2 \times \Delta I_{ds}}{\mu_n \times V_{gs}} = \frac{2 \times 23.4 \times 10^{-9}}{17 \times 20} = 1.376 \times 10^{-10} [C]$$

Then the total increased number of electrons at the channel is:

$$n_{channel\_electron} = \frac{\Delta Q}{q} = \frac{1.376 \times 10^{-10}}{1.6 \times 10^{-19}} = 8.6 \times 10^{8}$$

As a result, around 17% (8.6 x 10^8) of total generated hot electrons (5.05 x 10^9) are contributed to the increased drain current (ΔI_{ds}). And this number is defined as quantum efficiency (Q.E.).

As described in the main text, the gate voltage bias facilitates the hot electron transport to the FET channel. Therefore, the plasmon drain current was increased when higher gate voltage bias. Using the same method, we also calculated hot electron contribution efficiency (or QE) under different gate bias conditions as shown in Figure (5.10). This shows a unique property of plasmon FET, which is the internal efficiency of photo-generated hot electron efficiency, can be controlled by the gate voltage bias.

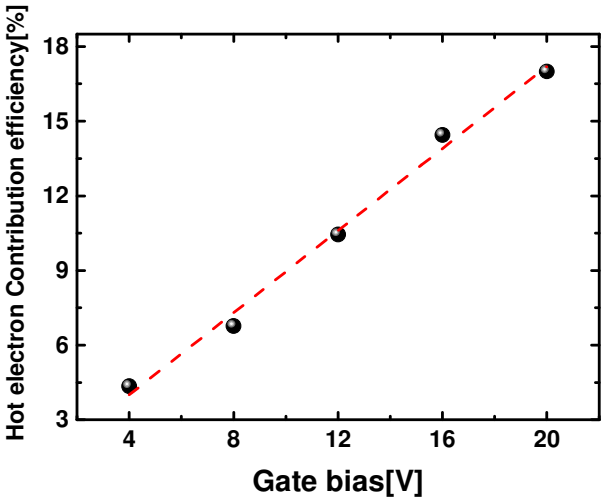

Figure 5.10 Hot electron contribution efficiency (or IQE) under different gate bias conditions. This set of data was calculated by using the results in Figure 5.5. This efficiency is the ratio of contributed hot electrons vs. generated hot electrons.

Finally, the number of hot electrons that each gold NPs contributes to the current channel of plasmon FET can be calculated. In this way, the covered area on plasmon FET is 100µm x100µm, and 5nm of gold was deposited before the thermal reflow process. Assuming average diameter of 10nm for Au nanoparticles after self-assembly process. Each nanoparticle has a volume of 4.186x $10^{-24}m^3$. The total volume of Au nanoparticles based on the fabrication condition is 10^{-12} m^3. Therefore, the plasmon FET has $1.19x10^7$ Au NPs. Therefore, the number of contributing electrons from each Au NP is $8.6x10^8/1.19x10^7$ =72.

In addition, we also calculated the quantum efficiency under no gate bias condition. As shown in Figure (5.5) the responsivity becomes extremely small without gate voltage bias. In this case, the device operates as a photoconductor. Thus, the drain current can be obtained using following equation [77]:

$$\Delta I_D = q \cdot \mu \cdot \Delta n \cdot E$$

Based on the measured data shown in figure (5.5), the calculated Δn is 1.225 x 10^4 under 30V V_{DS} bias. And it is around 0.0017% of the generated hot electrons in gold NPs. To confirm the working principle of plasmon FET several experiments have been done. To investigate the diffusion mechanism (process④ in digure (5.7)), plasmon FETs with different ZnO thicknesses were fabricated and spectral responses were calculated. In the next section, we will discuss this experiment.

Spectral response of plasmon FET with different ZnO thicknesses

The importance of gate bias assisted hot electron accumulation has been studied using devices with different ZnO channel thicknesses, and it shows that a stronger electric field is important for efficient plasmon energy detection. To understand this idea, the plasmon FETs were fabricated with different ZnO channel thicknesses (30, 50,100nm) and the spectral responses of each device were characterized. Under the same voltage bias condition, the highest spectral response was observed with the thinnest ZnO film (figure 5.8). This phenomenon can be explained by the distance that induced plasmonic hot electrons have to travel to reach the FET current channel. With a longer distance, the chance of recombination of hot electrons inside ZnO layer also becomes higher. Higher chance of recombination means there will be a very small amount of plasmon induced hot electrons which could be contributed to the transistor current enhancement. Based on the Figure (5.11), the plasmon FET with ZnO thickness of 100nm almost shows no plasmon spectral response. Also, plasmon FET with 30nm of ZnO shows the highest Plasmonic signal in compare with 50 and 100nm thick ZnO film.

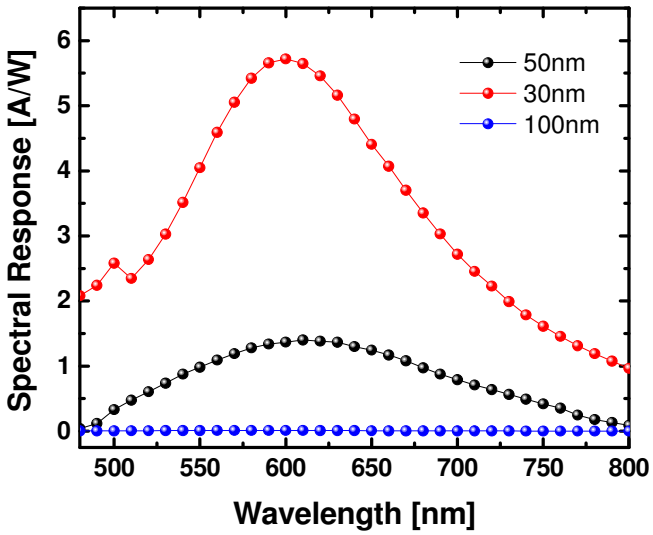

Figure 5.11 Spectral response of plasmon FET with different thicknesses of ZnO layer (30, 50,100nm)

After observing the fact that thinner ZnO layer provides a higher spectral response, it was in our interest to see how passivation layer between gold NPs and ZnO layer can change the plasmon FET spectral response. Because once there is a passivation layer between gold NPs and ZnO layer, induced plasmonic hot electrons have to tunnel through the passivation layer to reach ZnO. With this experiment, we could examine how the quantum tunneling mechanism (process ② in figure5.7) is happening inside the plasmon FET. Following section describe this experiment.

Effect of the passivation layer on plasmon FET spectral response

When gate bias is applied, there is another interesting hot electron migration mechanism, which is a quantum tunneling process through the thin Schottky barrier wall (process ② in figure 5.5). The modified potential from the positive gate bias creates not only a drift field to facilitate hot electron migration, but also a thin enough Schottky barrier

to allow electron tunneling from gold nanoparticles to semiconductor channel. In order to confirm this tunneling mechanism, we have fabricated HfO_2-layer (5-30 Å) inserted devices at the Schottky boundary (between gold and ZnO). The insulating HfO_2 layer inserted devices also show similar drain current amplification as a function of gate voltage bias which is shown in figure (5.12). The probability of quantum tunneling is an exponential function ($T = e^{-\alpha L}$, where, T is the probability of tunneled electrons, α is the wavenumber in the insulating layer, and L is the wall length) [78-80]. The measured drain current was decreased exponentially as the HfO_2 thickness is increased. These results were well matched with the expectation of tunneling induced hot electron migration and confirmed that quantum tunneling is one of the mechanisms of hot electron migration from the nanostructures to the semiconductor channel. Therefore, we can conclude that tunneling-assisted hot electron migration may enable a plasmon FET to detect photon energy that is well below the Schottky barrier energy. Also, we measured spectral response of each sample with a different thickness of HfO_2 passivation layer. Figure (5.13) shows these results with HfO_2-layer (5-30 Å). The thicker passivation layer causes smaller amount electrons migrate to the ZnO channel. The discrepancy between peak positions with different thicknesses of HfO_2-layer comes from the fact the HfO_2 has a lower refractive index in compare to the ZnO (figure (5.14)). And it means the thicker HfO_2-layer causes a lower refractive index value in the host matrix. According to this fact, we should expect a blue shift in the spectral response with an HfO_2-layer.

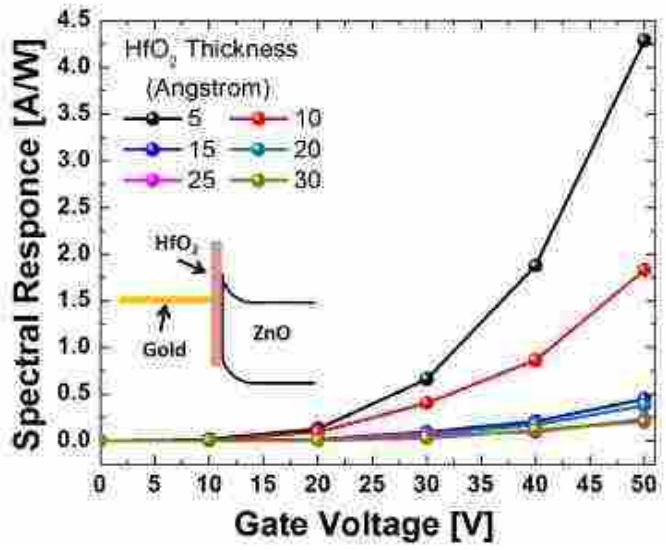

Figure 5.12 Measured Drain current from plasmon FETs with various thickness of HfO2 film between gold and ZnO layer. Each data point is taken from the peaks of the spectral responses.

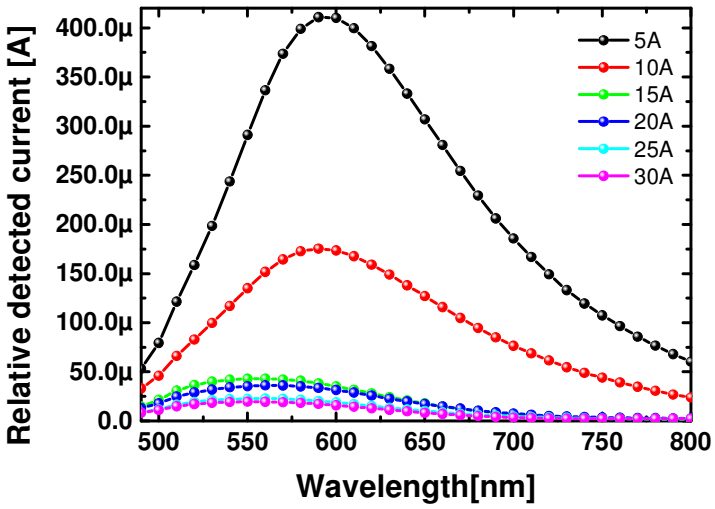

Figure 5.13 Spectral response of plasmon FET with different thickness of the passivation layer HfO2 (5-30 Å)

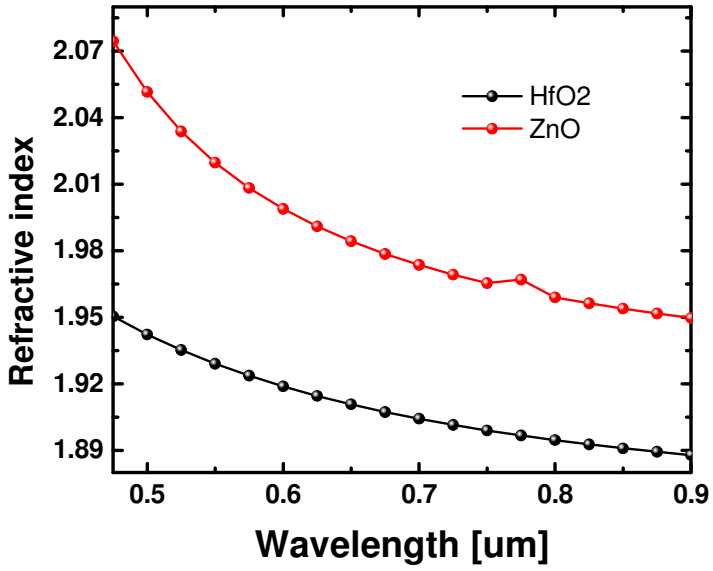

Figure 5.14 Refractive index for ZnO and HfO2 in the range of 0.5-0.9um

Sensitivity to surrounding refractive index

One of the fascinating properties of localized surface plasmon resonance is the spectral shift depending on the surrounding refractive index. To confirm this plasmonic property, we have carried out an experiment that shows modified spectral responses under different surface conditions of gold nanoparticles. The 3-mercaptohexanoic acid (MPA) molecule was used to cover gold NPs in the Plasmonic sensor. MPA has -HS terminated structure that can be easily bonded to gold. The refractive index for MPA is 1.4846 which higher that air. Figure (5.15) shows the absorbance of a glass sample with gold NPs on top with and without MPA coating. This figure indicates that gold NPs with MPA coating has lower resonance frequency and red shift in the absorbance spectrum confirms this idea. In addition, the absorbance of gold NPs coated with MPA has a higher amplitude in compare with gold NPs because MPA molecule increases the host refractive index of gold NPs. The

same experiment was done on the actual sensor which shows the result in the figure (5.16). As expected, after coating gold NPs on top of plasmon sensor with MPA molecule, the sensor shows a red shift in its spectral response. In the figure (5.16) the sensor responses without gold nanoparticles, with gold nanoparticles, and with functionalized gold nanoparticles with MPA are shown. There is no plasmon signal when there are no gold NPs. Moreover after MPA coating the spectrum experienced red shift around 25nm. It should be mentioned that after the MPA coating, plasmon signal magnitude becomes lower because a portion of the incoming light is absorbed by MPA molecules. Therefore, the intensity of the light that can reach NPs becomes smaller and as a results less plasmon absorption was produced.

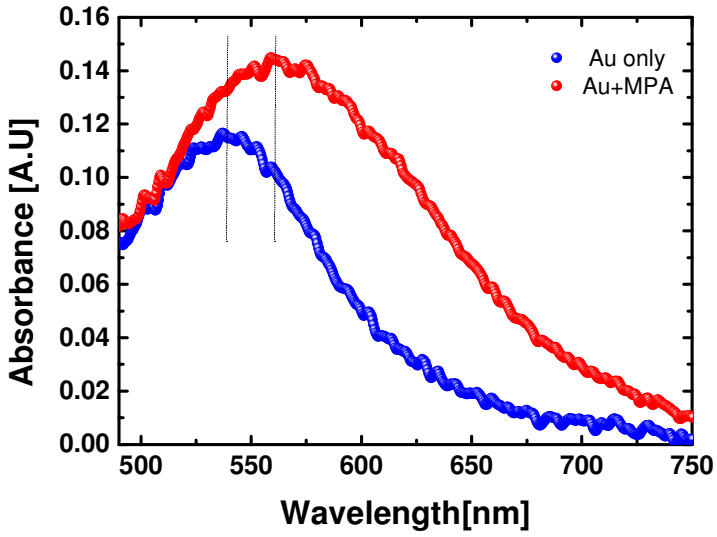

Figure 5.15 Absorption spectra of bare gold nanoparticles and 3-MPA coated gold nanoparticles. The nanoparticles are deposited on the glass substrate.

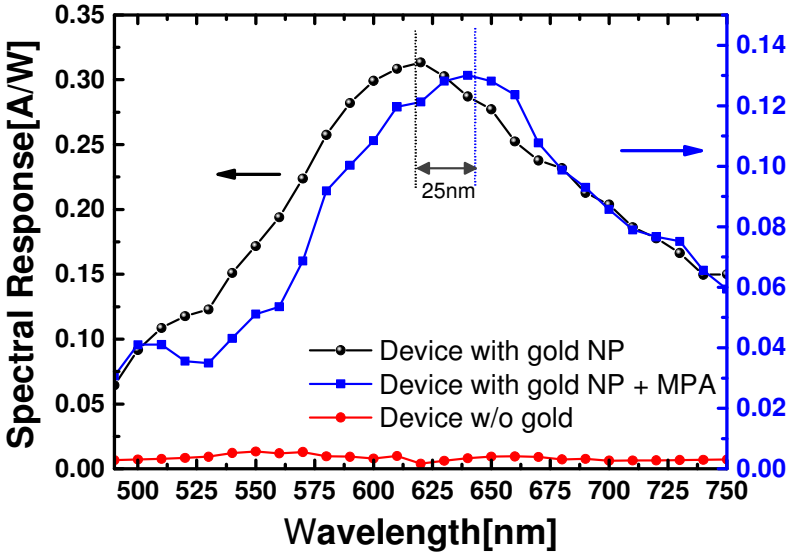

Figure 5.16 Spectral response of plasmon FET: the spectral responses are taken from an FET without gold NPs, after gold NP incorporation and after 3-MPA molecule attached on gold NPs.

In order to confirm the spectral shift from MPA functionalization is adequate, we have carried out a computational experiment using a finite-difference time-domain (FDTD) simulation. The nonlinear dispersion model based on FDTD (Rsoft FullWave) was used for this calculation. The gold NPs are on top of the ZnO layers, and they are not a perfect sphere shape as shown in figure (5.17), and it was confirmed by an AFM study. The base size of gold NPs is around 12nm which is in agreement with average nanoparticle sizes from AFM data. The transmitted power spectrum in the ZnO layer was obtained under different host matrix conditions for Au NPs (surrounding refractive index, n=1, 1.5, and 2). We observed that increased host material refractive index causes the red shift of the absorption spectrum (Figure 5.18). And the broader absorption spectrum was obtained with the increased refractive index of surrounding area.

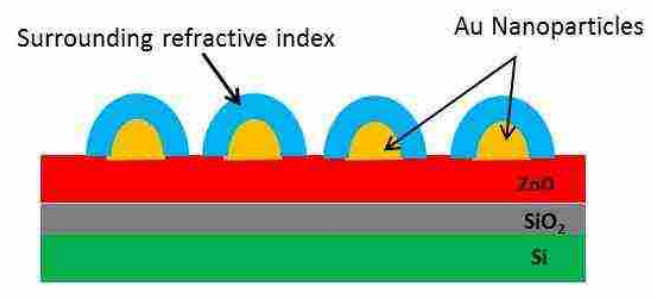

Figure 5.17 Geometry for FDTD Simulation

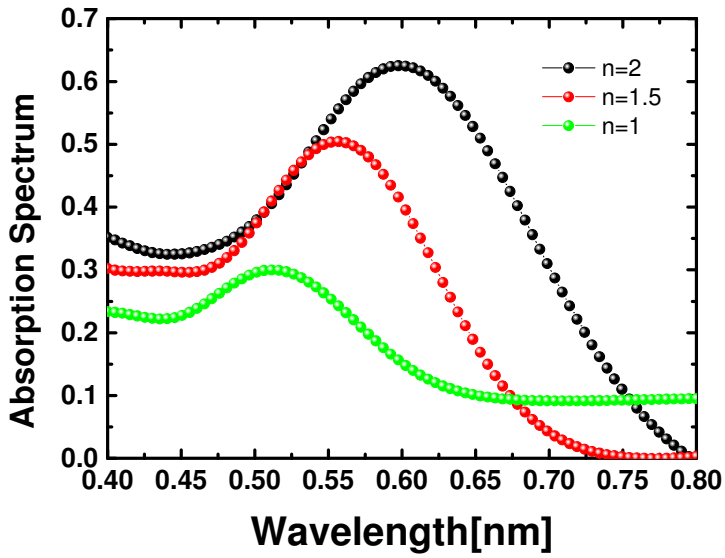

Figure 5.18 FDTD based simulated results for plasmonic absorbance using the geometry in FigureS7 with different gold NP surrounding refractive indices (1, 1.5 and 2).

As it mentioned before in chapter 4, the fabricated gold NPs on top of FET with self-assembly method are not completely spherical. The shape of gold NPs is most likely to be semi spheres as it shown in figure (5.17). The fact that the NP shapes are not spherical implies that the plasmon FET spectral response depends on the incident angle if the incoming light. We will explain this effect in the next section.

Power and incident angle dependence

A perfect sphere shape of gold nanoparticles can exhibit a narrow plasmon absorption spectrum, and independency to the polarization and angle of the incident light. Due to the thermal reflow based fabrication process, the gold nanoparticles are typically formed as a semi-spherical structure. We carried out an atomic force microscopy (AFM) study on the self-assembled gold nanoparticles on various substrates. The AFM image shows hemisphere shape of nanoparticle structure which has larger base sizes than their height. We have studied to understand how the hemisphere structure of the nanoparticles changes the spectral response of the plasmon FET by changing the incident angle of the light. The following results show how incident angle could affect the profile of spectral response of plasmon FET. The spectral response of the plasmon FET was measured with two different angles, 45° and 0°, to the plasmon FET (Figure 5.19). This shows that 90° incident angle has better full-width-half-maximum (FWHM) response and bigger spectral response (R=A/W) value than 45° incident angle. The absorption peaks were slightly different in both cases. We believe that better spectral response from 90° incident angle is mainly caused by the strength of the hot electron momentum inside the gold nanoparticles. It could be explained by using the limited escape cone theory for hot electron emission, which means that the hot electron momentum (kinetic energy) should be greater than the barrier height [77]. Since the initial hot electron momentum is inherited from the incident photon energy (Poynting vector), the incident angle to the gold nanostructure is an important parameter for hot electron emission over the Schottky junction barrier. In addition, we carried out illuminated power dependency study using neutral density filters which cut

75%, 50%, and 25% of incoming power. As expected, the plasmon detection is a function of a number of photons that produce hot electrons in the gold nanoparticle.

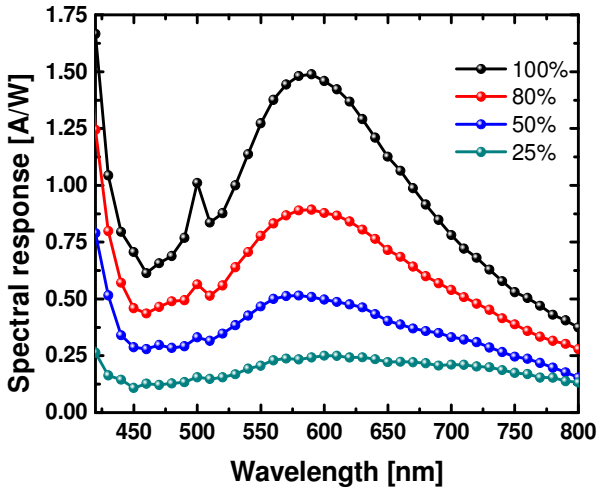

(**a**)

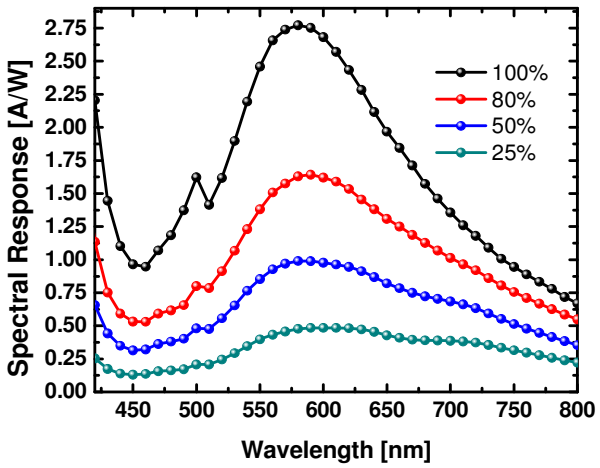

(**b**)

Figure 5.19 Spectral response of plasmon FET with different incident power and incident angles (a) 45°, (b) 0°

So far, we have done several experiments on plasmon FET. However, all of these experiments have done while the plasmon FET was in saturation mode. It would be interesting to examine the plasmon FET while it works under zero gate voltage bias

because any detected spectral response in this mode is due to only the contributed induced plasmon hot electrons and not enhancement in transistor channel conductance level. This effect will be explained in the next section.

Drift current based plasmonic spectral response

When the light illumination keeps generating hot electrons inside gold NPs at the plasmon resonance frequencies, the generated hot electrons can migrate to the ZnO layer by the thermionic emission mechanism. And these migrated hot electrons can be collected by the electric field across the Drain and Source as a drift current ($I_{drift} = \sigma E$, where σ is the conductivity of ZnO channel, and E is the electric field). The channel conductivity can vary depending on the contribution from the plasmonic induced hot electrons. Therefore, more plasmon induced hot electron will increase drift current. The stronger electric field that is produced by the Drain-Source voltage bias can increase the drift current (figure 5.20). However, this operation has a very poor spectral response because it only collects the intrinsic number of plasmon induced hot electrons, and there is recombination loss while they are traveling through the channel (between Drain and Source). As it can be seen in figure (5.20), with zero drain-source voltage the spectral response of plasmon FET is almost zero. Although the generated plasmon induced hot electrons could diffuse inside ZnO layer, they are most likely to recombine because there is no electric field. However, once the drain-source voltage increases the lateral electric filed increases which bring more electrons into the transistor current. This experimental result shows the importance of the gate voltage bias that enables the amplification of detected hot electrons.

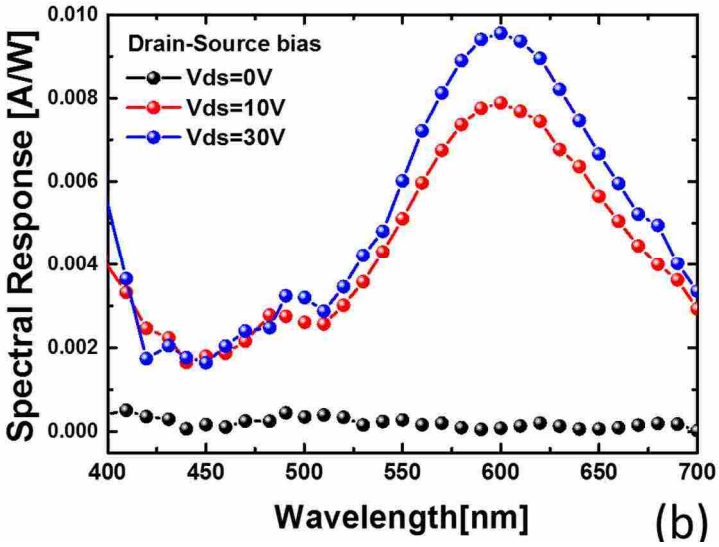

Figure 5.20 Spectral response of plasmon FET with zero gate voltage and Vds=0,10,30V (Vg=0V).

Plasmon FET under negative gate bias voltage

Under negative gate bias voltage condition, there is a slight photo response in shorter wavelength. But we did not observe any plasmonic response. There could be two reasons. First, by applying negative gate bias for an n-type thin film transistor, the accumulation region could not be formed. Hence, there is no current passing through the semiconductor layer. And the negative bias eventually blocks the hot electron transfer from metal to semiconductor. The slight increase in shorter wavelength needs further investigation.

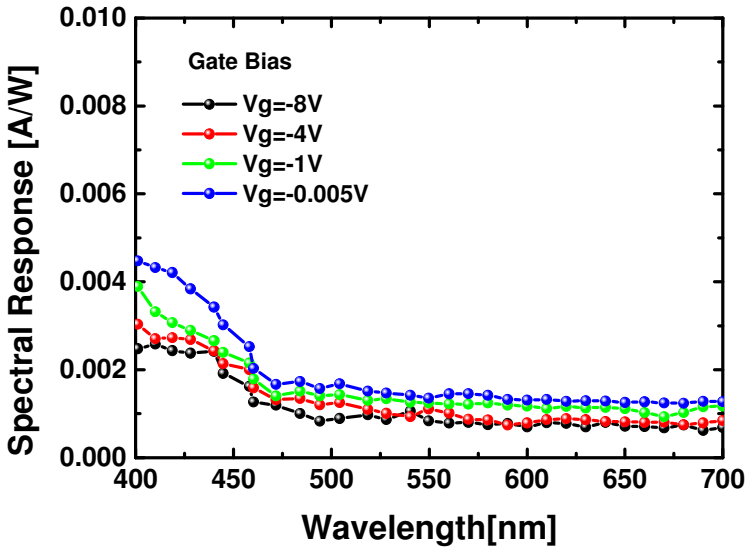

Figure 5.21 Spectral response of plasmon FET under negative gate bias voltage

Conclusion

In this chapter, we analyzed plasmon FET with several experiments. The plasmon FET shows very high spectral [A/W] response, and it implies the plasmon FET can produce more than one electrons from one photon excitation. These results show that the plasmon FET not only can directly detect the plasmon energy but also it can efficiently amplify the detected plasmon energy. Plasmon FET works based on two different mechanisms: fist, induced plasmonic hot electrons overcome the Schottky barrier and diffuse into the ZnO layer and second they can tunnel through Schottky barrier and migrate to ZnO layer. To confirm the suggested working principles for the plasmon FET, plasmon FETs with different thicknesses of ZnO and passivation layer between gold NPs and ZnO were fabricated. The extracted results from these devices confirm that the quantum tunneling effect is happening at plasmon resonance frequency because once the passivation layer becomes thicker, the spectral response of plasmon FET decreases. Also, once the ZnO layer

becomes thicker, the spectral response decreases because the chance of recombination of induced plasmon hot electrons becomes higher. As a result, they can no longer contribute to transistor current enhancement. Moreover, the plasmon FET can detect the changes in surrounding refractive index of gold NPs. After MPA coating on the gold nanoparticle surface, the device shows a 25nm red shift in its spectral response. The FDTD simulation results also confirm that the spectral response of plasmon FET follows the absorption spectrum of gold NPs on top of ZnO.

In summary, the plasmon FET is a novel device that can detect and amplify plasmon energy. As a LSPR sensor, it can detect the changes in surrounding refractive index of gold NPs. All these capabilities make the plasmon FET a unique device which could be used for different applications especially for biomedical purposes such antigen-antibody bonding detection.

Chapter 6

Plasmon FET for specific protein recognition

In this chapter, we will study the application of the Plasmon FET as a bio-sensing platform. Herein, we demonstrate that Plasmon FET can detect the binding of Specific proteins to a carbohydrate linkers. Attaching of proteins to the gold nanoparticles incorporated in Plasmon FET modifies the refractive index surrounding the gold NPs which broadens and redshifts the absorption spectrum of Au NPs. Plasmon FET can detect the induced plasmonic hot electrons in Au NPs as explained in the previous chapter. Therefore, the redshift and broadening effect in the absorption spectrum of Au NPs can also be revealed using Plasmon FET. In addition, we compared the Plasmon FET sensor with conventional LSPR sensors which shows Plasmon FET has higher sensitivity per concentration due to amplification process involved plasmonic hot electron detection.

We immobilized glycopolymers onto the surface of plasmonic field effect transistor (FET), and we could detect the recognition between lectins and surface-immobilized glycopolymers over a wide dynamic range (10^{-10} to 10^{-4} M) in an environment that resembles the glycocalyx. The binding to the sensor surface by various lectins was tested, and the selectivities and relative binding affinity trends observed in solution were maintained on the sensor surface, albeit with significantly higher avidities. The combination of polymer surface chemistry and optoelectronic output in this device architecture produces the highest reported detection sensitivity for ConA, and lends itself to fundamental biological studies and integration into point-of-use diagnostics and sensors.

The importance of glycan binding proteins (GBPs)

The binding events between glycan binding proteins, termed lectins, and cell-surface glycans – including glycopolymers, glycoproteins, and glycolipids – are the subject of increasing research focus because of their critical role in intercellular communication, immune response, and disease progression [81-83]. Glycan recognition within the glycocalyx – the 1 – 100 μm layer of glycans that coat the surface of every eukaryotic cell – is inherently interfacial and as a consequence, multivalency [84] and cooperativity [85] play an outsized role in determining binding strength and selectivity within this dense forest of carbohydrates. To mimic and understand how glycan-lectin recognition occurs in biology, these events must be studied on surfaces, where aspects of the 3D structure of the glycocalyx that influence the association between receptor and ligand can be reproduced. While many instruments for studying interfacial binding exist, the complexity of glycan recognition imposes stringent demands upon their detection sensitivity and ligand presentation. Firstly, these sensors must possess a wide dynamic range, and be able to detect binding at low lectin concentrations [86]. While many glycan-lectin interactions are strong ($K_a \sim 10^5 – 10^6$ M^{-1}) [87], they are usually far weaker than normal protein-substrate interactions, with K_a typically on the order of $10^3 – 10^1$ M^{-1} [88]. Secondly, lectins are typically promiscuous proteins, and bind most monosaccharides weakly in solution. Lectin-substrate specificity is achieved by accessing multivalent and cooperative interactions that occur in the dense matrix of the cell surface, which can increase K_a by up to 10^6 M^{-1} [84]. Thus, to understand lectin-glycan binding in biological systems, the glycans on a sensor surface must be presented with the appropriate valency, density, and orientation to capture dynamics that may occur within the glycocalyx [89]. Therefore, a

sensing platform that can detect binding between glycans and lectins that are present in nanomolar concentrations or quantify differences in binding affinities would be an important tool in advancing the rapidly developing fields of glycobiology [88] and carbohydrate nanotechnology [90].

Conventional colorimetric LSPR sensors

Current advances in the fabrication of nanostructures have contributed significantly to the development of materials with unique plasmonic properties, whose applications include photovoltaic devices [91, 92], biomedical sensors [93-95], and point of care diagnostics [96, 97]. One such plasmonic device that could contribute to studying glycan binding is the localized surface plasmon resonance (LSPR) sensor, which is a label-free tool that monitors molecular binding in real-time, in small-volume samples[18-22], and with picomolar sensitivity when K_a is high ($>10^7\ M^{-1}$) [98-102]. The biological systems that have been analyzed by LSPR include protein-substrate [103], nucleotide-nucleotide [104-112], antigen-antibody [106, 113-115], and glycan-lectin binding [116]. All of the aforementioned examples employ the conventional colorimetric LSPR architecture, where detecting binding involves monitoring changes of reflectance or transmittance of the plasmonic nanostructures. Despite the sensitivity of LSPR, a drawback of these devices is that they require optical detection, which precludes facile integration into microfabricated chips. Moreover, the measured transmittance or reflectance in LSPR sensors is also affected by the medium surrounding the nanostructures, which can produce false readings when the nanostructures and surrounding medium have an overlapping feature in their absorption spectrum.

Plasmon FET as a bio-sensing platform

The Plasmon Field Effect Transistor (FET) [117] detects plasmon shifts electronically, and, as a result of optoelectronic amplification, provides sufficiently high sensitivity to detect weak binding events at low analyte concentration. The plasmon FET monitors the plasmonic absorption of Au nanoparticles (NPs) on the device surface by converting the induced plasmonic hot electrons to electrical current, which is accompanied by an amplification of the hot plasmonic electrons that overcome the Schottky junction formed by Au and InGaZnO (IGZO) (Figure 6.1a(i)) [2]. Applying a gate voltage bias accelerates the entry of electrons into the n-channel of the plasmon FET (Figure 6.1a (ii)) by producing a vertical potential difference, which drives the electrons that must otherwise diffuse thermally through the IGZO film to reach to the n-channel. Thermal diffusion alone would result in decreased hot electron current as a result of recombination processes and the short mean-free-path of hot electrons in IGZO. Drain current enhancement occurs when excess plasmonic carriers enter the FET current channel (Figure 6.1a (iii)), and as a consequence of this current enhancement, the sensor is sensitively dependent to the changes in the plasmonic absorption. The distinction between the plasmonic FET platform and conventional LSPR is that the former uses light for excitation, but electronic detection, whereas the latter uses both optical excitation and detection. As a consequence the plasmon FET design obviates the need for an optical readout and associated instrumentation, reducing the device footprint, while improving simultaneously the detection sensitivity. In addition, the plasmon FET only detects the plasmonic signal from the nanostructure

absorption, which eliminates the parasitic signal from media that occurs in conventional LSPR sensors.

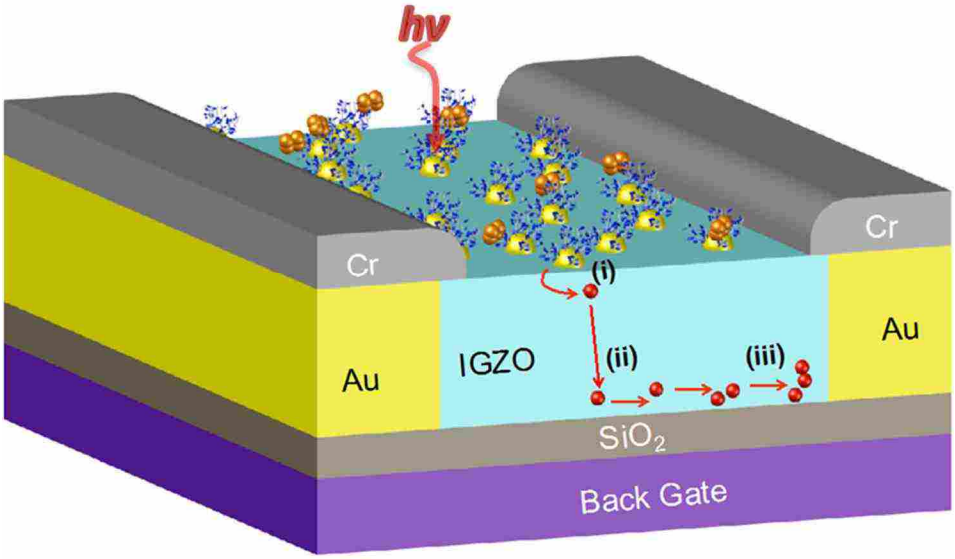

Figure 6.1 A plasmonic field effect transistor (FET) for sensing lectins is coated with a layer of Au NP-glycopolymer conjugates. Increases in plasmon absorption with the binding of lectins to the glycopolymers increase the electrical current (dimensions are not proportional): (i) Hot electron transfer from Au NPs to IGZO layer by overcoming the Schottky junction. (ii) The applied gate voltage assists the migration of hot electrons into the current channel of the plasmon FET. (iii) The number of charge carriers increases in the IGZO layer, thereby enhancing the detected signal.

As a result of these attributes, the plasmon FET offers 5-fold higher signal-to-noise ratio than conventional LSPR sensors, which makes them ideal for low noise applications – such as glycan-lectin recognition, where binding is inherently weak and complex. Thus, when combined with appropriate surface chemistry, the plasmon FET could lead to

breakthroughs in understanding cell-surface binding in an environment intended to mimic directly the interfacial structure of the glycocalyx.

Functionalization of plasmon FET surface

In this section, we report that this platform that can detect binding between glycopolymers appended to Au NPs on the plasmon FET surface and lectins in solution (Figure 6.1), even when the latter are present in only picomolar concentrations. The glycopolymer coating on the Au NPs is designed to mimic the glycan density and presentation in the glycocalyx so that the observed binding captures cooperative and multivalent dynamics that are more representative of cell surface recognition than would occur in glycan monolayers. The unique combination of electronic detection and polymer surface chemistry provides a sensing platform with high substrate specificity and that is two orders of magnitude more sensitive than conventional fluorescence detection on a surface composed of identical glycopolymers [118]. This increase in detection sensitivity is particularly important in the context of glycobiology, where binding interactions are weak and lectins are present at exceedingly low concentrations, and as such, this platform – that combines new device architectures with synthetic glycopolymers – has the potential to make important contributions to understanding cell-surface glycan recognition.

The construction of the lectin-binding plasmon FET involved microfabrication of the device followed by surface-functionalization with synthetic glycopolymers (Figure 6.2 a-d). The plasmon FET was fabricated by following previously explained in chapter 4, and the surface was functionalized by the photochemical synthesis of glycan brush polymers with pendant α-D-glucose residues from the Au NPs on the device surface, resulting in a dense carbohydrate forest that mimics the glycocalyx [118]. Briefly, a heavily doped n-

type Si substrate (the back gate) with 50 nm of the thermally grown SiO_2 film was prepared, and an n-type IGZO film, which serves as the active semiconductor channel (30 µm × 100 µm), was deposited and patterned on top of the SiO_2. The Au NPs are incorporated using a thermal reflow based self-assembly method [119] on top of the IGZO surface, such that they are physically separated from all three electrodes of the plasmon FET.

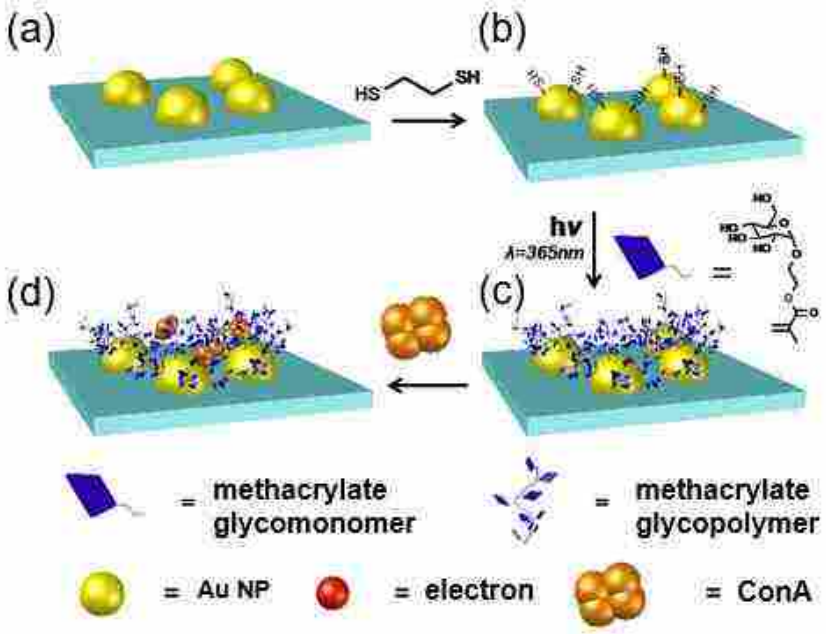

Figure 6.2 Sensor fabrication: a) Au NPs are self-assembled onto the plasmon FET; b) 1,2-ethanedithiol is adsorbed onto the Au NPs; c) glucosyloxyethyl methacrylate is incubated onto the Au NP under UV light (λ = 365 nm) in the presence of a photoinitiator for 2 h to form the glycopolymer via a thiol-acrylate photopolymerization; d) binding of the lectin ConA to the glycopolymers on the Au NP surfaces.

To make the plasmon FET specific towards glucose-binding lectins, the Au NPs were functionalized with methacrylate polymer brushes with pendant D-glucose residues at each repeat unit following a previously reported surface-polymerization approach [118].

Briefly, the sensors are cleaned in an oxygen plasma (Harrick Plasma Cleaner PDC-32G) at high RF level for 15 min. The surfaces were rinsed with acetone (10 mL), ethanol

(10 mL) and air dried. The samples were dehydrated on a hot plate at 300 °C for 10 min, and cooled down to RT. The samples were immersed in 1.5 mM 1,2-ethanedithiol (in ethanol) in a glovebox overnight. The 10 nm Cr layer limits the attachment of the thiols to the Au NPs. a drop of 1,2-ethanedithiol solution (1.5 mM in EtOH) was placed onto the IGZO surface to produce thiol-capped Au NPs (Figure 1b). After washing with EtOH (10 mL), the substrate was placed in a solution of glycosyloxyethyl methacrylate (1 mM in EtOH) along with the photoinitiator 2,2-dimethoxy-2-phenylacetophenone (1.56 mM), and the surfaces were exposed to 365 nm light for 2 h to grow the glycopolymers from the Au NPs by a thiol-methacrylate radical photopolymerization mechanism. The samples were immersed in 1 mM Glycosyloxyethyl methacrylate ethanolic solution with 1.56 mM DMPA for 2 h under 365 nm UV light excitation. The samples were rinsed with ethanol (10 mL), acetone (10 mL), water (10 mL), and air dried. The polymer-modified samples were immersed in 1% BSA in phosphate buffer (pH 7.1) at 4°C for 2 h to passivate the sensor surface and reduce nonspecific lectin adsorption[3]. The sample was rinsed with phosphate buffer (10 mL) three times and air-dried.

To demonstrate the ability to detect lectins in solution, the plasmon FETs with the α-D-glucose side-chain functionalized glycopolymers were exposed to solutions containing different concentrations of the glucose-binding lectin concanavalin A (ConA). The binding between ConA and glycans is a widely studied model system in glycobiology [120-122] that is often used to validate new lectin-sensing platforms because ConA is widely available, its specificity is well understood, and its K_a towards different monosaccharide substrates has been quantified.

Measurement setup for Plasmon FET as a sensor

To study the binding of ConA onto the plasmon FET, the monochromated input modulated light was delivered onto the sensor surface by an optical fiber with a 45° incident angle. The sensors were biased with 20 V of drain-source voltage and 25 V of gate voltage, which produced approximately 4 μA of drain-source current that is passed through a resistor in series with the plasmon FET. The resulting voltage across the resistor is read by the lock-in amplifier, and is used as the measure of binding between polymer and lectin because voltage increases with the association of the protein to the glyocpolymers on the sensor surface. Figure 6.3 shows the electrical circuit for the sensing measurements.

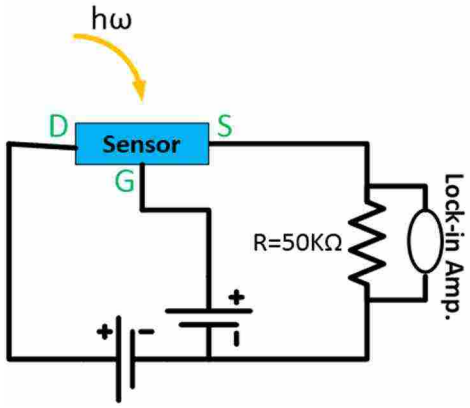

Figure 6.3 Electrical circuit to measure the plasmon FET based sensors.

To measure the voltage change upon binding, each sensor was mounted onto a probe station and a monochromatic light was channeled through a fiber-optic and delivered onto the sensor at a 45° angle. The optical measurement system consists of a quartz tungsten halogen lamp (250W, Oriel), a lock-in amplifier (SR830, Stanford Research) with a mechanical chopper, a monochromator (SP2300, Princeton Instruments), and appropriate optical filters to suppress the second harmonic light from the monochromator. The light power was measured using a NIST calibrated silicon photodetector (FDS-1010CAL, Thorlabs) and an optical power meter (PM100D with S120VC, Thorlabs). The optical light

power was kept constant during measurements of all sensors. A customized LabView program was utilized to control the monochromator, the lock-in amplifier and the picoammeter for the automated computerized measurements.Binding assays were run by immersing the sensor into the ConA solution in phosphate buffer saline (137 mM NaCl, 2.7 mM KCl, 10 mM Na_2HPO_4, 1.8 mM KH_2PO_4, 0.5 mM $CaCl_2 \bullet 2H_2O$, 0.5 mM $MnCl_2$) at 4 °C for 4 h. To study the plasmon FET response to the ConA solution, measurements were taken at two different excitation wavelengths (500 & 600 nm). Typical localized plasmonic based sensors measure the shifted plasmonic absorption to quantify the amount of analytes. We adopted a different approach in this work using two wavelengths that are located before and after the plasmonic absorption peak maximum.

The plasmon FET sensor uses two monochromatic light illumination wavelengths, and converts the strength of the plasmonic absorption to an electrical signal. Therefore, comparing changes in absorption in response to binding of these two sample points provide the plasmonic absorption shift indirectly. To measure the voltage signal generated by the sensor, the plasmon FETs were kept in the dark for 1 min, and then illuminated by 600 nm light for 1 min. Following another 2 min in the dark, the plasmon FET was exposed to 500 nm light for 1 min. The detected voltage signal levels at the two wavelengths are different because of the dependence of hot electron generation on the wavelength of the incident light as shown in Figure 6.4. The plasmonic absorption peak of the Au NPs is 560 nm before ConA binding, and the plasmonic absorption peak red shifts to 610 nm when ConA binds to the polymers on the Au NP surface because the presence of the protein increases the effective refractive index of the medium surrounding the Au NPs [123]. The change in the absorption spectrum of Au NPs at two wavelengths (ΔA_{600}, ΔA_{500}) due to ConA binding

represents the spectral shift of the plasmonic absorption and is an indicator of binding as illustrated in figure 6.5, where ΔA_{600nm} and ΔA_{500nm} are the change in absorption spectrum at 600 and 500 nm, respectively.

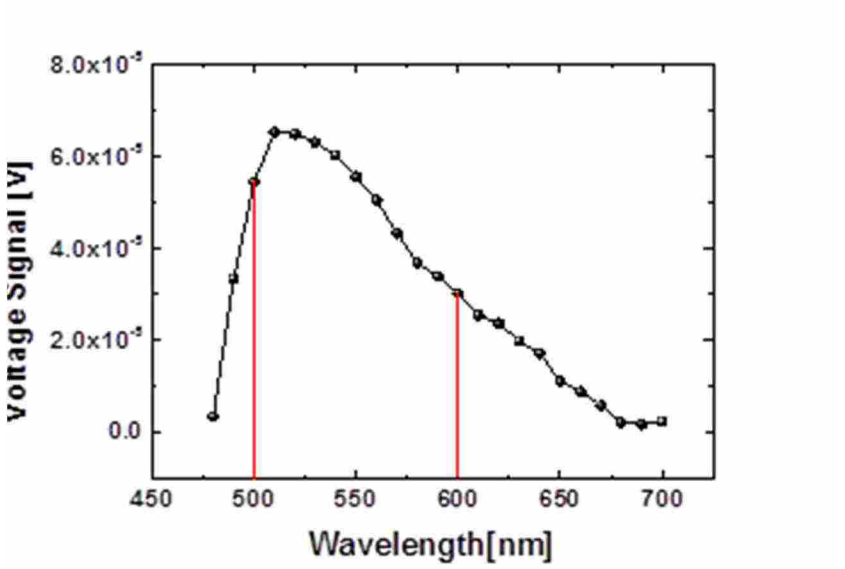

Figure 6.4 the reference sensor generated signal at each wavelength

Following confirmation that the glycopolymer-modified plasmon FET could detect the presence of ConA, the sensor was exposed to solutions with varying ConA concentration to determine the dynamic range and detection limit of this platform. The measured optical response of the sensor towards solutions with different concentrations of the ConA is shown in Figure 6.6. Higher concentration of ConA drives complexation, which increases the voltage signal, broadens and red-shifts the absorption spectrum, and ultimately increases signal current [115]. The observed detection limit of the plasmon FET towards ConA – below which no protein could be detected – is 1.0×10^{-10} M, and the sensor saturates at 2.1×10^{-5} M, indicating that the plasmon FET has a five-decade dynamic range.

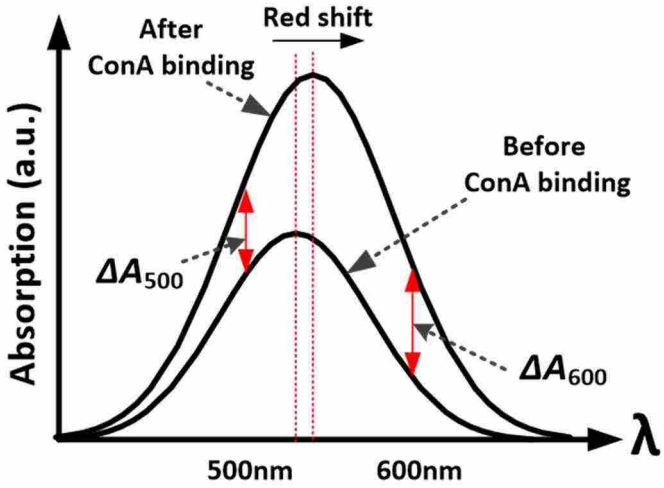

Figure 6.5 Absorption spectrum of the Au NPs in solution, before (bottom curve) and after (top curve) binding of the target analytes. After binding of the analyte to the NP surface, the absorption spectrum broadens, increases in intensity, and redshifts. ΔA_{600} and ΔA_{500} are the changes in absorption in response to binding at 600 and 500 nm, respectively

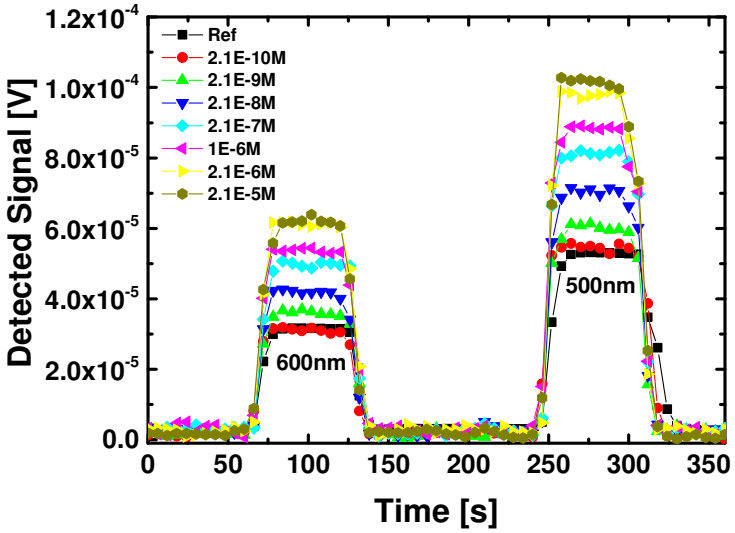

Figure 6.6 Detected voltage signal through the plasmon FET under two different color excitations (500 and 600 nm) with different concentrations of ConA (black line shows the reference plasmon FET before binding of ConA).

Comparison of Plasmon FET with LSPR sensor

To compare directly the sensitivity of the glycopolymer-modified plasmon FET to more conventional sensing platforms, we studied ConA binding to the same glycopolymers on a spectrometer-based LSPR sensor with optical detection. The LSPR surface was prepared by depositing Au NPs onto a glass substrate in the same reforming procedure used in the plasmon FET, and the optical absorption spectrum was measured using a conventional optical spectrometer. To measure the conventional LSPR architecture, where the change in absorption spectrum is used to indicate binding, the same Au NP-glycopolymer conjugates were patterned on top of a glass substrate. Using a white light source (Quartz Tungsten Halogen lamp (250W), Oriel) and an optical spectrometer (StellarNet, BLACK-Comet Concave Grating), the absorption spectrum of Au NPs was obtained. Figure 6.7 shows the experiment diagram for LSPR based sensor measurement. White light was brought to the LSPR sensor from a halogen lamp using an optical fiber and two objective lenses to collimate and focus the light onto the sample. Using another optical fiber, the transmitted light was brought to the spectrometer, and the absorption spectrum was calculated. Following the same protocols used to synthesize the glycopolymers and assess binding to the plasmon FET, absorption spectra were measured following exposure to solutions containing varying concentrations of ConA (2.1×10^{-9} M – 2.1×10^{-6} M) and results are shown in figure 6.8.

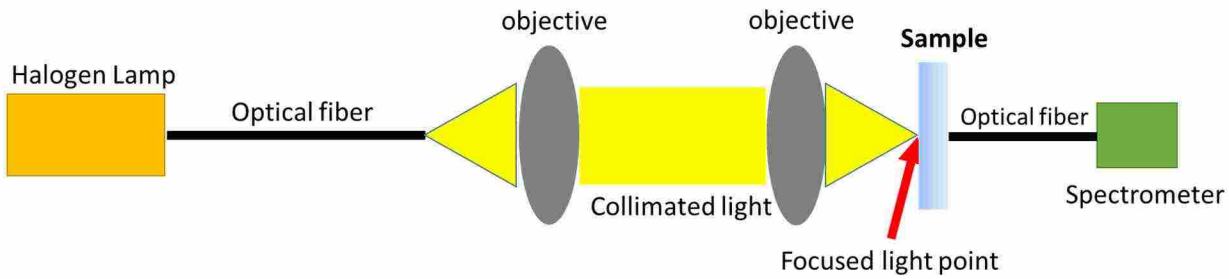

Figure 6.7 LSPR based sensor measurement diagram. Two objective lenses were used to collimate the light and focus on top of the sample. The fiber optic tip behind the sample gathered the transmitted light through the sample and brought light into the spectrometer.

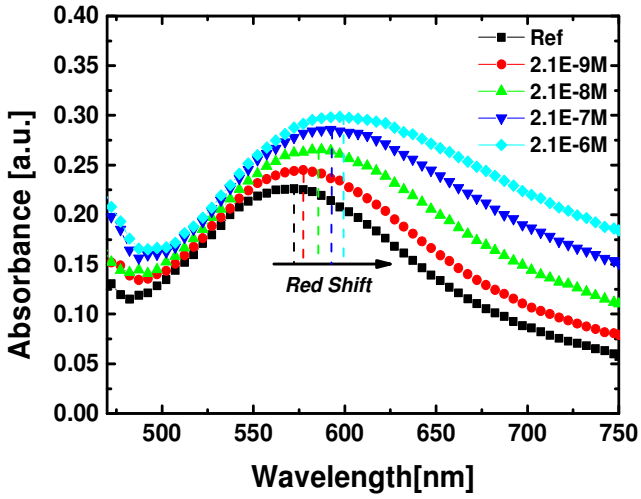

Figure 6.8 Absorption spectra using the conventional spectrometer LSPR-based sensing (control experiment) with different concentrations of ConA (the dashed lines show the redshift upon increasing ConA concentration).

By comparing the signal change at each wavelength with increasing ConA concentration for the plasmon FET and the LSPR sensors, we observed that the plasmon FET generates a larger signal response than the LSPR at the same protein concentration as shown in figure 6.9. The calculated slope of the least squares regression of the relationship between ConA concentration and signal response at 500 nm (Figure 6.9a) indicates that the plasmon FET induces a 5 times larger signal response than the spectrometer-based LSPR sensor. At 600

nm (Figure 6.9b) where the control LSPR sensor shows the highest level of sensitivity, the plasmon FET presents a two-fold larger signal response. Therefore, the plasmon FET, as a consequence of its amplified electrical readout, offers an enhanced sensitivity towards lectin concentration changes than conventional, spectrometer-based LSPR sensors.

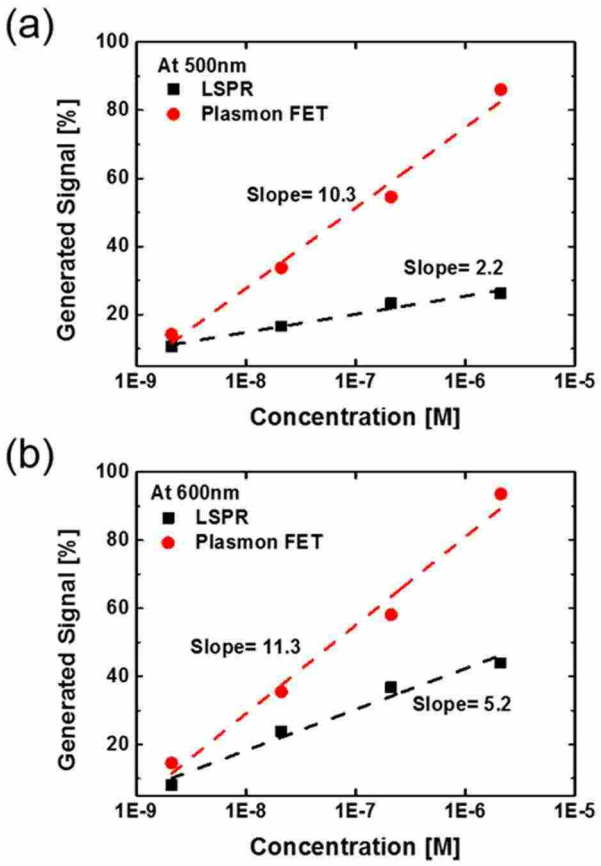

Figure 6.9 The normalized signal (%) of the plasmon FET sensor vs. LSPR based sensor with different concentrations of ConA a) under 500 nm, and b) 600 nm illumination. The normalized signal for the plasmon FET-based sensor was obtained by dividing the voltage change in sensor response as a result of binding of the ConA at each concentration by the reference sensor voltage level (initial voltage signal before sensing).

Selectivity of Plasmon FET over different range of GBPs

The glycopolymer-modified plasmon FET was also exposed to solutions containing different lectins to demonstrate that the variations in binding affinities between these proteins for glucose known from solution studies would manifest as differences in signal response at equivalent concentrations as shown in the following the figure.

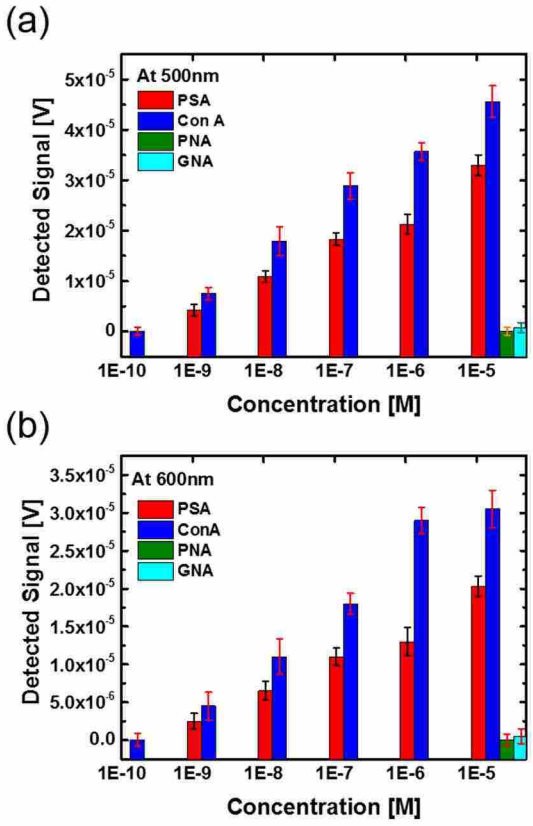

Figure 6.10 Plasmon FET voltage change signal with different target proteins (ConA, PSA, PNA and GNA) at a) 500 nm and b) 600 nm excitation at varying protein concentrations. The error bars are a standard deviation from the mean.

In addition to ConA, the plasmon FET was exposed to solutions containing peanut agglutinin (PNA), galanthus nivalis agglutinin (GNA), and pisum sativum agglutinin (PSA). While ConA is known to possess the strongest binding towards glucose of the lectins analyzed [124], PSA also binds glucose[48], albeit with lower affinity, whereas neither PNA nor GNA bind glucosides [125]. A lower signal current was observed for PSA compared to ConA for all concentrations. No increase in signal current was observed when the sensor was exposed to PNA and GNA solutions at the high concentration of 2.1×10^{-5} M (Figure 6.11), and these observations are consistent with expectations based on previously known binding trends.

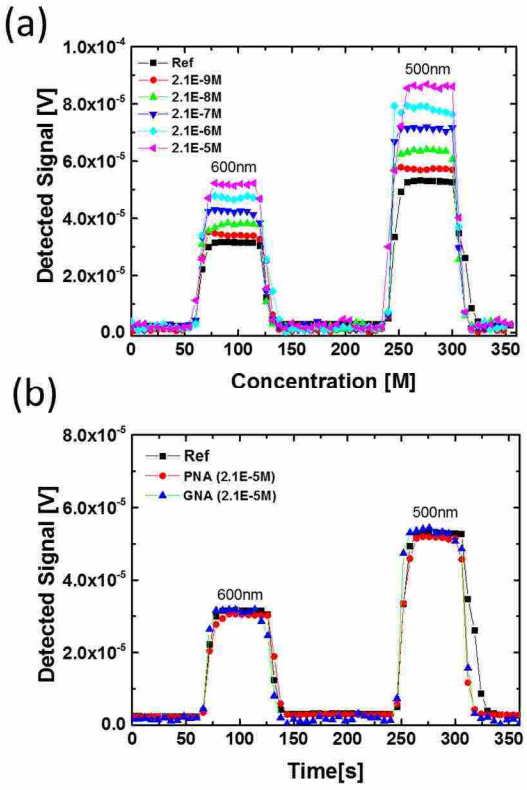

Figure 6.11 The measured sensor response under 500 nm and 600 nm with a) PSA and b) GNA and PNA proteins.

Calculation of binding association constant (K_a)

To determine quantitatively the K_as between the lectins and the glycopolymers on the plasmon FET surface, the current response for each lectin solution was fit to the Langmuir isotherm [126, 127] (6-1),

$$\Delta R/\Delta R_{max} = (K_a[P])/(1+K_a[P]) \quad (6\text{-}1)$$

where ΔR is the device response (the change in detected voltage), ΔR_{max} is the maximum response (maximum change in detected voltage), K_a is the binding constant, and $[P]$ is the lectin concentration. The Langmuir isotherm is the widely accepted method for determining the strength of association between glycans and lectins in microarray-[128, 129] and SPR-based [130, 131] sensors, and applying this model provides numbers that can be compared across platforms. To obtain the K_a values, the data points were plotted against lectin concentration; the points were fitted according to Eq. 1; K_as are reported as averages from all concentrations; and errors are presented as a standard deviation from the mean value. The K_a for the binding between ConA on the glycopolymer on the plasmon FET surface was determined to be $1.66 \pm 0.14 \times 10^7$ M^{-1} at 500 nm excitation and $1.28 \pm 0.1 \times 10^7$ M^{-1} at 600 nm excitation. The K_a for the binding of PSA onto the plasmon FET surface was $6.53 \pm 0.58 \times 10^6$ M^{-1} at 600 nm excitation, and $5.81 \pm 0.43 \times 10^6$ M^{-1} at 500 nm. The larger value of the K_a for ConA than for PSA is consistent with the trend observed for solution binding. For PNA and GNA, no shifting in the absorption spectrum or increased current was observed, which was expected because neither of these two lectins are known to bind glucose in solution. This control experiment confirms that the observed voltage changes in the sensor are the direct result of lectin-carbohydrate binding rather than

nonspecific adsorption. Importantly, the K_a value for the binding between ConA and the glycopolymers on the plasmon FET surface exceeds by nearly four orders-of-magnitude the K_a value of 2.3 x 10^3 M^{-1} for the association between ConA and α-D-methoxyglucopyranoside in aqueous solution, and to the best of our knowledge is stronger than any previously reported binding of ConA to glucosides [132, 133].

Why is this glycopolymer-modified plasmon FET so sensitive towards lectins, and how does this platform provide insight into how multivalency of the glycopolymers contribute to the observed binding dynamics? The binding of ConA to surface immobilized ligands has been studied extensively [132, 133], and the increased avidity with increasing glycan density and valency is well-established. Using octomeric-dendritic mannoside ligands, for example, a two-fold enhancement in binding was observed compared to monovalent surfaces, resulting in K_as of 2 x 10^6 M^{-1} and a detection limit of 10 nM (0.26 μg mL^{-1}) [128]. The binding of ConA to α-glucose on the surface is highly dependent on carbohydrate spacing, and using microarrays the K_a was found to be as high as 8.8 x 10^6 M^{-1} [122] when the glucosides were immobilized in a multivalent fashion on the protein BSA and at high BSA surface density. The K_a of 1.66 ± 0.14×10^7 M^{-1} that we observed between ConA and the glycopolymers on the plasmon FET are higher than these previously reported values, and this unprecedented avidity can be understood by considering the mechanism of ConA binding to multivalent ligands. The four binding sites of ConA are separated by 6.5 nm, and binds multivalent ligands in solution with negative cooperativity as a result of diminishing entropy with each subsequent binding event [134]. As a consequence, the increase in avidity between multivalent ligands and ConA is sensitively dependent on ligand structure. It has been observed previously that ConA attaches to

multivalent brush polymers through a bind-and-jump mechanism, where the protein attaches and detaches as it works its way along the polymer backbone towards the surface [135]. Thus, with increasing surface density, avidity increases because of cross-linking between chains. In addition, when studying ConA binding to multivalent polymers, K_a increased with increasing polymer length because sufficiently long polymers could simultaneously interact with the different subunits of the protein [121]. We have shown previously that the glycopolymers prepared under these thiol-acrylate radical photopolymerization conditions are ~1 μm in length [118], and are therefore sufficiently long to bridge multiple binding sites simultaneously, although the possibility of cross-linking cannot be excluded. These interactions with multiple binding sites simultaneously likely prevent the bind-and-slide behavior observed with shorter polymers [135] or multivalent ligands that cannot bind multiple subunits of ConA simultaneously [134] – like dendrimers [122] or BSA conjugates – thereby leading to the significant avidity enhancement. Thus, the picomolar detection sensitivity towards ConA of this glycopolymer-plasmon FET compared to previously used SPR and microarray methods is the result of a combination of the amplified detection signal and enhanced surface avidity.

Summary

In conclusion, the recently developed plasmon field effect transistor was combined with multivalent glycopolymer brushes, resulting in the most sensitive binding reported between ConA and glucosides. The increased sensitivity relative to conventional optical LSPR or fluorescence sensors occurs because of electronic amplification enabled by the plasmon-to-electric conversion, which eliminates the need for the optical read-out, in combination with the high avidity to the long polymers. As a result, the plasmon FET is a promising

candidate for biological applications where specific, low-concentration detection is important. In addition, the electric readout obviates the need for optical detection and facilitates integration into miniaturized electronics. In the future, plasmon excitation can be realized using light emitting devices, which could make the sensing system simpler and cost effective, and incorporating plasmon FETs into multiplexed architectures could provide high-throughput, highly-sensitive platforms for glycobiology.

Chapter 7

Summary and Future Works

In this project, we tried to solve the current technology problem regarding the localized surface plasmon detectors. After reviewing the current research trends and reports, we addressed current issues with the LSPR detection technology that uses bulky optical instrumentation. Recently, there have been several demonstrations of LSPR detection without the bulky optical instrumentation. A common approach for this direct LSPR detection is the use of metal-semiconductor Schottky junction based detector. However, these Schottky junction based devices show a poor quantum efficiency. Moreover plasmon absorber, the metal nanostructure, was usually used as an electrode in such devices. This is an important drawback because this device structure is not suitable for biomedical applications that require the functionalization of the metal nanostructures. To address the issues discussed above, we developed a novel device structure, named plasmon field effect transistor.

Plasmon field effect transistor is a new device with the capability of direct detection and efficient amplification of plasmon energy. In addition, the plasmon FET is capable of working inside a liquid which makes this sensor a great candidate for bio-applications. In this way, gold nanoparticles, which are electrically isolated from transistor contacts, could be functionalized with specific antigens or antibodies. The functionalized gold nanoparticles could capture their secondary antigens-antibodies and plasmon FET can detect this attachment process. This novel device could be fabricated with standard micro fabrication methods. Fabrication procedures are very straight forward and simple which is

important for mass production and cost reduction. The optical response of the plasmon FET is quiet robust which is very vital in the sensing applications. Depending on the nanostructures shape, size and composition, plasmon FET optical response could be from the visible region to IR frequencies.

Plasmon FET uses a thin film transistor structure to detect and amplify the LSPR signal. We did several studies to find out the working principle of plasmon FET. We fabricated Plasmon FET with different thicknesses, length and material of transistor channel. As we explained in chapter 5, depending on the gate bias voltage, the spectral response of plasmon FET shows different values. Also, we deposited different thicknesses of passivation layers between transistor channel layer and gold NPs. Briefly, we understood that the induced generated hot electrons in gold NPs migrate to the transistor channel through either quantum tunneling or jumping over the Schottky barrier. Once electrons diffuse to ZnO layer, they increase the conductivity of the ZnO channel. This increased conductivity in the transistor channel leads to higher drain-source current level.

Due to the attractive optical property of metallic nanostructures, there have been many sensing applications reported using LSPR technology. Many of them have focused on using LSPR in biomedical assays. There have been several reports of the biotin-streptavidin interaction detection by LSPR assay with sensitivity variously reported to range from picomolar to micromolar concentration. LSPR utility is also shown for protein biomarkers in whole blood or serum samples [98, 102, 136-138]. LSPR has also been used in an immunoassay platform to detect antibody-antigen interaction with an equilibrium constant (K_{eq}) ranging from 10^9 to 10^{10} M^{-1} [103, 106, 113]. In other studies, LSPR sensing has been used to detect interactions for other biomolecules, such as nucleic acid hybridization,

protein–carbohydrate, cytochrome–inhibitor, aptamer–protein, and toxin–receptor interactions [95, 111, 112, 139-141]. LSPR has been widely used as a chemical sensor to detect gas, volatile organic compounds, pH, and ammonia [104, 107, 130]. All the above applications use LSPR in a typical colorimetric format, by detection of reflectance or transmittance of the metallic nanostructures. Therefore, it requires relatively simple instrumentation such as a spectrometer and a light source combination, compared to bulky SPR sensor devices. In addition, lack of need for temperature control enables quick diagnosis using LSPR without pre-calibration and provides a point-of-care device capability. In order to take advantage of all these features, there have been several attempts to reduce the sensor size and modify the instrumentation to allow multiplexing capability [102, 103, 109, 111]. The smallest sensing area was achieved using an optical-fiber based system by embedding nanoparticles at the tip of fiber-optic cable [94]. Despite successful demonstration, the device size is not small enough to maximize the advantage of its detection capability, because one needs to compensate for the bulk dielectric sensitivity and signal-to-noise ratio. Also, the reduction in sensing surface does not obviate the use of external optical instruments such as a light source and a spectrometer, aside from the fact that the smaller sensing area requires sophisticated optics to detect the target. Thus, it is still a challenging problem to make a handheld, integrated system with optics and a chip level LSPR sensor possessing a wide dynamic range of sensitivity.

Plasmon FET also shows that it can detect the changes of refractive index around gold NPs. In the experiment that we carried out, gold nanoparticles were functionalized with 3-MPA. Plasmon FET showed 25nm redshift in spectral response in compare with the sample which didn't have 3-MPA molecule. This result shows the feasibility of the plasmon FET

as a biosensing platform. Targeting specific biomarkers could be achieved by plasmon FET. Once the gold nanoparticles on plasmon FET functionalized with specific linkers, target molecules could be attached to those linkers resulting a change in average surrounding refractive index of gold NPs which is detectable by plasmon FET.

In this dissertation, we proposed a new bio-sensing platform for specific protein detection. The specific interactions of antigen-antibody are useful in the clinical laboratory for diagnostic purposes. As discussed earlier in chapter 6, the LSPR sensors are successfully demonstrated as a sensing platform for the antigen-antibody interaction [83]. As illustrated in figure (7.1), this is a well-known phenomenon in localized surface plasmon sensors that each step of functionalization on metal NPs causes a red shift in absorption spectrum because of change in host refractive index matrix of NPs. Here, we want to apply the same concept on our plasmon FET. We want to immobilize the first antibody on gold NPs in plasmon FET structure. If the first antibody could capture the secondary antigen, then we expect to see red shift in our spectral response.

First we replaced the ZnO layer in plasmon FET structure with IGZO layer to gain more stability upon exposing to different liquids. We started to find out a suitable protocol to functionalize gold NPs on top of IGZO layer. In this way, we used the already developed protocol with carbohydrates linkers and tried to capture a target protein (ConA) specifically as we explained the details in chapter 6. The conducted experiments in Chapter 6 showed that the plasmon FET can detect the target protein. Moreover it can distinguish between different glycan protein bindings. This exciting fact is important in biological applications such as diagnosis and treatment. The developed sensor using plasmon FET showed higher sensitivity per concentration than LSPR based colorimetric sensor. Along with the

elimination of optical read out system in comparison with colorimetric sensors, plasmon FET could be a perfect candidate for integration and multi protein analysis. Figure 7.2, shows the sensing mechanism using plasmon FET.

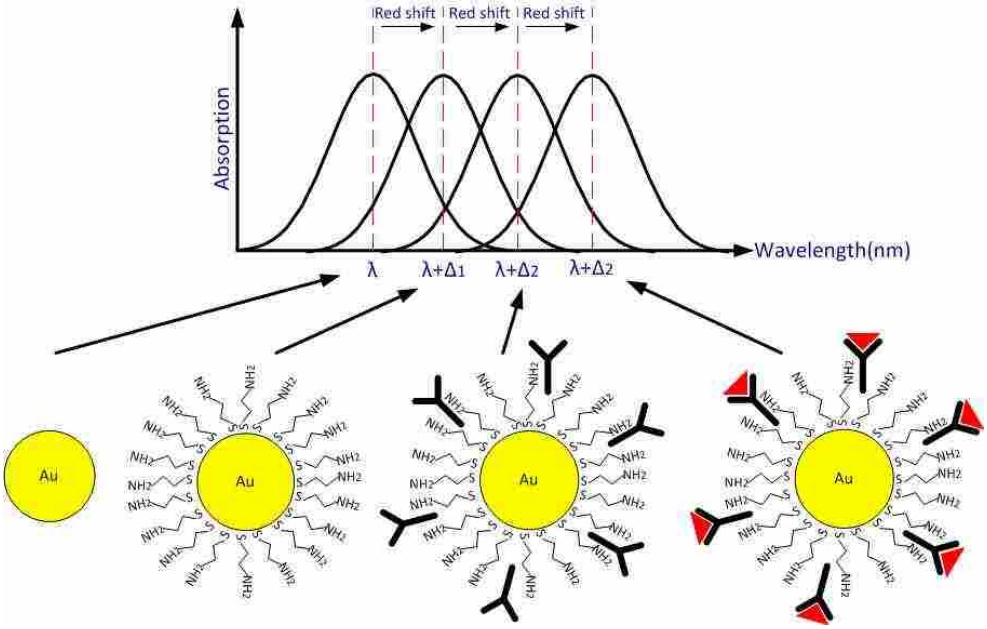

Figure 7.1 red shift of the absorption spectrum due to increasing in surrounding refractive index of Au NP

To study antigen-antibody binding, we tried to use a protocol that could create a covalent binding between the fist antigen and the linker. Its is important to have the linkers as short as possible. Therefore, we choose the MPA as a linker. Then to prove that the protocol will attach the fist antigen to the linker, the following control experiment was done.

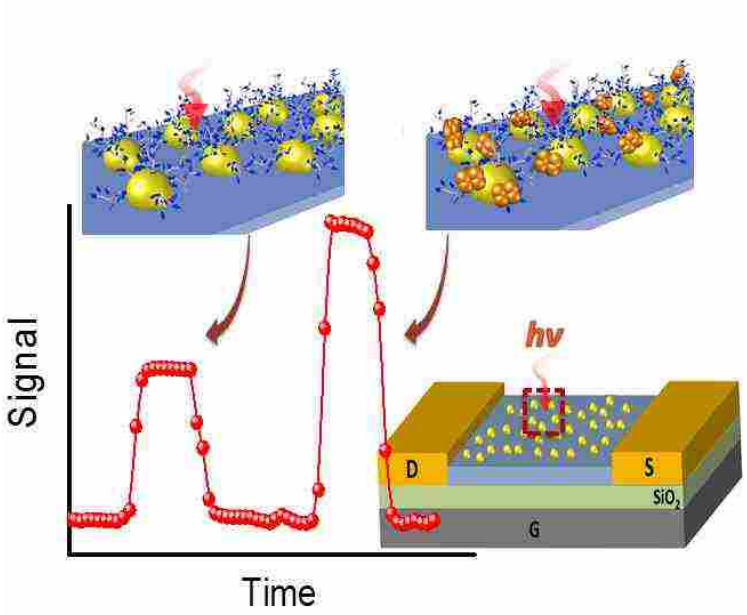

Figure 7.2 Schematic of sensing mechanism using Plasmon FET

We prepaid a substrate shown in figure (7.3a). Our substrate consists of glass/Cr/Au. Using thermal evaporation of gold (5nm) and following heat treatment (300^{o}C for 10min), gold NPs formed on top of the Cr layer. Figure (7.3b) shows the functionalization steps for Antibody (Ab) immobilization on the gold surface. In this experiment, we used four different samples as it shown in fig 7-3b. The surface is initially treated with 3-Mercaptopropronic Acid (MPA) where the thiol group binds to the gold leaving the carboxylic ends available for attaching the Ab. Using EDC/S-NHS the carboxylic ends are activated to allow binding of Ab through their amine groups. Once the Ab are immobilized the sensor was used to detect the antigen. UV-Vis measurement shows a red shift after as each component (MPA, Antibody, Antigen) is added on the gold surface confirming that functionalization (MPA), immobilization (Ab), and detection (Antigen) is occurring (figure 7.7).

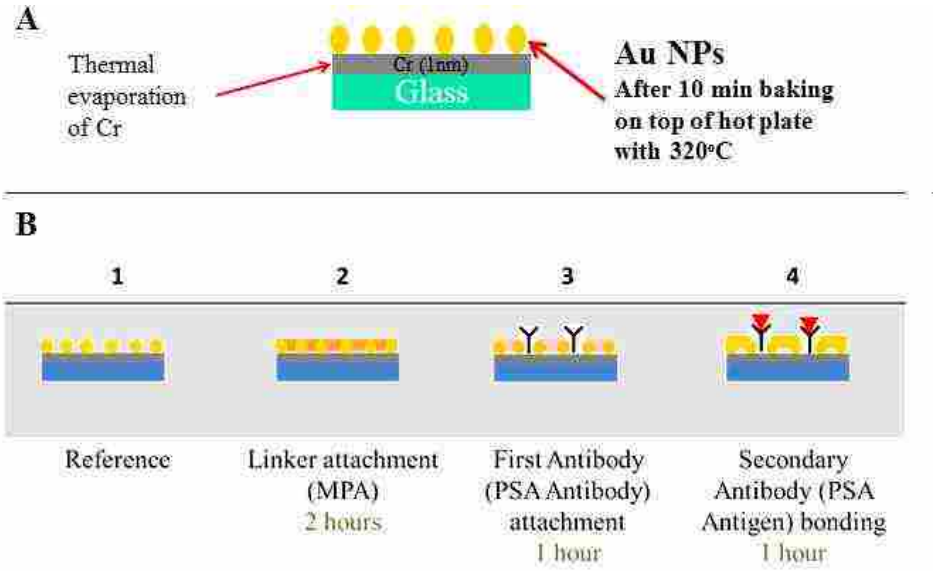

Figure 7.3 a) Prior to functionalizing the gold surface. The chip is baked at 320˚C to allow the formation of a self-assembled monolayer (SAM) of Au NP. B) Shows the functionalization steps for Antibody (Ab) immobilization on the gold surface.

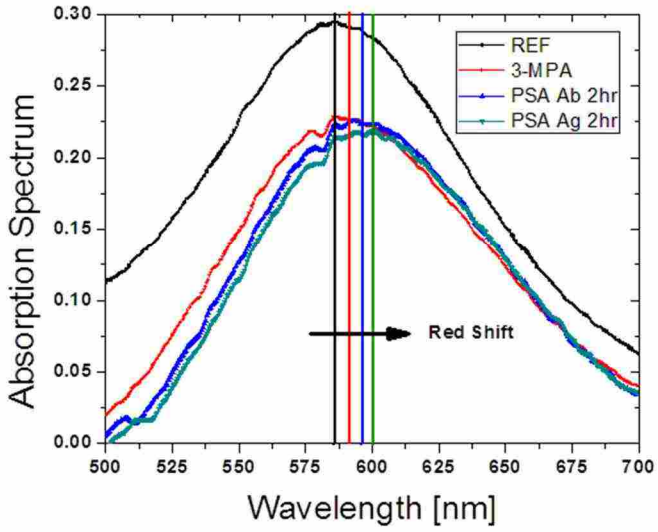

Figure 7.4 UV-Vis measurement. Red shift is clear after as each component (MPA, Antibody, Antigen) is added on the gold surface

The above protocol can be used in the plasmonic sensor shown in figure (7.5a). The structure of this sensor is different form plasmon FET. This sensor consists of metal/semiconductor/metal structure. The microfluidic channel is used to bring molecules on top of the sensor. Single LED (550nm) along with lock-in amplifier system can be used to monitor antigen-antibody interaction in real time (Figure 7.5b).

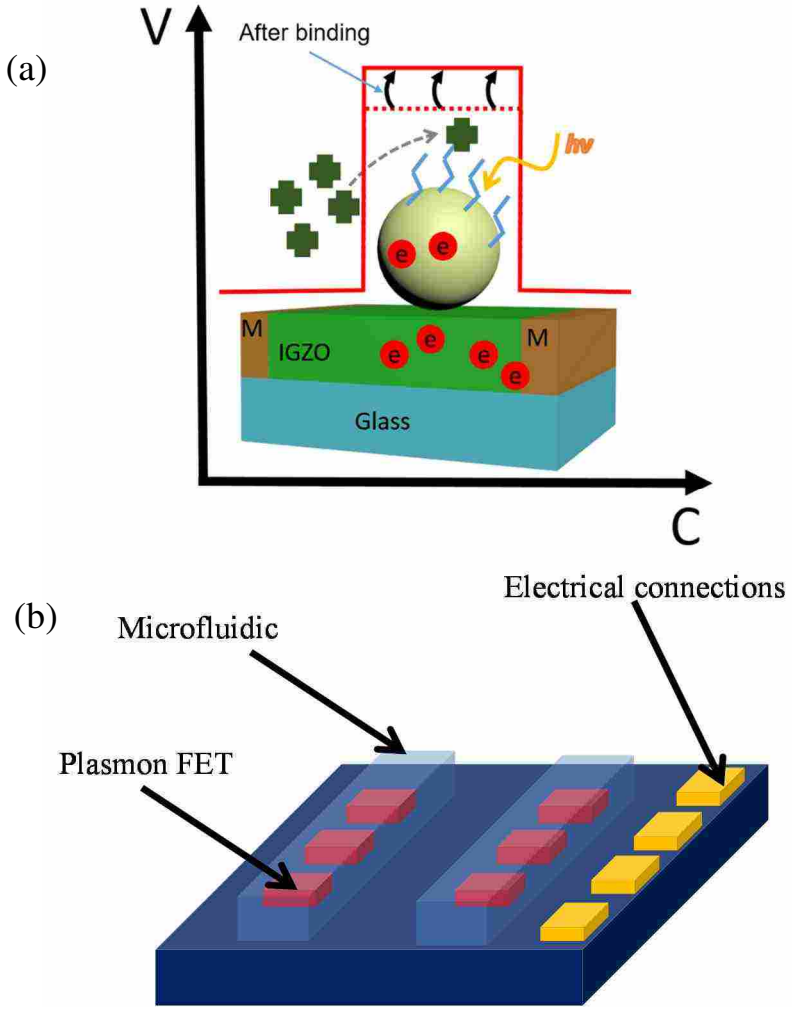

Figure 7.5 a) real time sensing concept b) schematic of proposed chip which is able to detect antigen-antibody attachment

For the future work, the whole plasmon FET sensing system could be integrated into USB device connected to a computer system and controlled by a costume software. Using the serial communication a single LED could be turned on/off at a certain frequency. By implementing the signal processing program, the read-out current of the sensors can be analyzed, and binding of antigen-antibody could be detected. This small sensing system could work with the USB power. Therefore it does not need any external power system. In addition, its portable system which could be used anywhere with minimal supervision.

WORKS CITED

[1] A. M. Gobin, M. H. Lee, N. J. Halas, W. D. James, R. A. Drezek, and J. L. West, "Near-infrared resonant nanoshells for combined optical imaging and photothermal cancer therapy," *Nano Letters,* vol. 7, pp. 1929-1934, Jul 2007.

[2] M. W. Knight, H. Sobhani, P. Nordlander, and N. J. Halas, "Photodetection with active optical antennas," *Science,* vol. 332, pp. 702-704, 2011.

[3] S. Lal, S. Link, and N. J. Halas, "Nano-optics from sensing to waveguiding," *Nat Photon,* vol. 1, pp. 641-648, 2007.

[4] B. Saleh and M. Teich, *Fundamentals of photonics (Wiley Series in Pure and Applied Optics)*: John Wiley & Sons, 1991.

[5] J. Homola, S. S. Yee, and G. Gauglitz, "Surface plasmon resonance sensors: review," *Sensors and Actuators B: Chemical,* vol. 54, pp. 3-15, 1999.

[6] R. H. Ritchie, "Plasma losses by fast electrons in thin films," *Physical Review,* vol. 106, pp. 874-881, 1957.

[7] K. M. Mayer and J. H. Hafner, "Localized surface plasmon resonance sensors," *Chemical Reviews,* vol. 111, pp. 3828-3857, 2011.

[8] H. A. Atwater and A. Polman, "Plasmonics for improved photovoltaic devices," *Nat Mater,* vol. 9, pp. 205-213, 2010.

[9] M. L. Juan, M. Righini, and R. Quidant, "Plasmon nano-optical tweezers," *Nat Photon,* vol. 5, pp. 349-356, 2011.

[10] Y. B. Zheng, B. Kiraly, P. S. Weiss, and T. J. Huang, "Molecular plasmonics for biology and nanomedicine," *Nanomedicine,* vol. 7, pp. 751-770, 2012/05/01 2012.

[11] V. E. Ferry, L. A. Sweatlock, D. Pacifici, and H. A. Atwater, "Plasmonic nanostructure design for efficient light coupling into solar cells," *Nano Letters,* vol. 8, pp. 4391-4397, 2008/12/10 2008.

[12] E. Kasper and M. Oehme, "High speed germanium detectors on Si," *physica status solidi (c),* vol. 5, pp. 3144-3149, 2008.

[13] C.-H. Lin and C. W. Liu, "Metal-insulator-semiconductor photodetectors," *Sensors,* vol. 10, pp. 8797-8826, 2010.

[14] S. Pillai, K. R. Catchpole, T. Trupke, and M. A. Green, "Surface plasmon enhanced silicon solar cells," *Journal of Applied Physics,* vol. 101, pp. 093105-8, 2007.

[15] J. Vuckovic, M. Loncar, and A. Scherer, "Surface plasmon enhanced light-emitting diode," *Quantum Electronics, IEEE Journal of,* vol. 36, pp. 1131-1144, 2000.

[16] F. P. García de Arquer, A. Mihi, D. Kufer, and G. Konstantatos, "Photoelectric energy conversion of plasmon-generated hot carriers in metal–insulator–semiconductor structures," *ACS Nano,* vol. 7, pp. 3581-3588, 2013.

[17] Y. K. Lee, C. H. Jung, J. Park, H. Seo, G. A. Somorjai, and J. Y. Park, "Surface plasmon-driven hot electron flow probed with metal-semiconductor nanodiodes," *Nano Letters,* vol. 11, pp. 4251-4255, 2011/10/12 2011.

[18] L. Tang, S. E. Kocabas, S. Latif, A. K. Okyay, D.-S. Ly-Gagnon, K. C. Saraswat*, et al.*, "Nanometre-scale germanium photodetector enhanced by a near-infrared dipole antenna," *Nat Photon,* vol. 2, pp. 226-229, 2008.

[19] N. Yu, J. Fan, Q. J. Wang, C. Pflugl, L. Diehl, T. Edamura*, et al.*, "Small-divergence semiconductor lasers by plasmonic collimation," *Nat Photon,* vol. 2, pp. 564-570, 2008.

[20] A. G. Brolo, "Plasmonics for future biosensors," *Nat Photon,* vol. 6, pp. 709-713, 2012.

[21] T. Chung, S.-Y. Lee, E. Y. Song, H. Chun, and B. Lee, "Plasmonic nanostructures for nano-scale bio-sensing," *Sensors,* vol. 11, pp. 10907-10929, 2011.

[22] N. Liu and A. Pucci, "Plasmonic biosensors: know your molecules," *Nat Mater,* vol. 11, pp. 9-10, 2012.

[23] S. Mubeen, G. Hernandez-Sosa, D. Moses, J. Lee, and M. Moskovits, "Plasmonic photosensitization of a wide band gap semiconductor: converting plasmons to charge carriers," *Nano Letters,* vol. 11, pp. 5548-5552, 2011.

[24] K. M. Byun, S. M. Jang, S. J. Kim, and D. Kim, "Effect of target localization on the sensitivity of a localized surface plasmon resonance biosensor based on subwavelength metallic nanostructures," *JOSA A,* vol. 26, pp. 1027-1034, 2009.

[25] A. J. Haes and R. P. V. Duyne, "Preliminary studies and potential applications of localized surface plasmon resonance spectroscopy in medical diagnostics," *Expert Review of Molecular Diagnostics,* vol. 4, pp. 527-537, 2004.

[26] K. Ma, D. J. Kim, K. Kim, S. Moon, and D. Kim, "Target-localized nanograting-based surface plasmon resonance detection toward label-free molecular biosensing," *Selected Topics in Quantum Electronics, IEEE Journal of,* vol. 16, pp. 1004-1014, 2010.

[27] Y. Shao, S. Xu, X. Zheng, Y. Wang, and W. Xu, "Optical fiber LSPR biosensor prepared by gold nanoparticle assembly on polyelectrolyte multilayer," *Sensors,* vol. 10, pp. 3585-3596, 2010.

[28] T. A. Gschneidtner, S. Chen, J. B. Christensen, M. Käll, and K. Moth-Poulsen, "Toward plasmonic biosensors functionalized by a photoinduced surface reaction," *The Journal of Physical Chemistry C,* 2013.

[29] D. Mortazavi, A. Z. Kouzani, A. Kaynak, and D. Wei, "Nano-plasmonic biosensors: a review," in *Complex Medical Engineering (CME), 2011 IEEE/ICME International Conference on*, 2011, pp. 31-36.

[30] H. A. Atwater, "The promise of plasmonics," *Scientific American,* vol. 296, pp. 56-62, 2007.

[31] S. A. Maier, *plasmonics: fundamentals and applications: fundamentals and applications*: Springer, 2007.

[32] D. Bohm and T. Staver, "Application of collective treatment of electron and ion vibrations to theories of conductivity and superconductivity," *Physical Review,* vol. 84, p. 836, 1951.

[33] W. L. Barnes, A. Dereux, and T. W. Ebbesen, "Surface plasmon subwavelength optics," *Nature,* vol. 424, pp. 824-830, 2003.

[34] M. Specht, J. Pedarnig, W. Heckl, and T. Hänsch, "Scanning plasmon near-field microscope," *Physical Review Letters,* vol. 68, p. 476, 1992.

[35] C.-G. Blatchford, J. Campbell, and J. A. Creighton, "Plasma resonance—enhanced Raman scattering by absorbates on gold colloids: the effects of aggregation," *Surface Science,* vol. 120, pp. 435-455, 1982.

[36] C. F. Bohren and D. R. Huffman, *Absorption and scattering of light by small particles*: John Wiley & Sons, 2008.

[37] K. Catchpole and A. Polman, "Plasmonic solar cells," *Optics Express,* vol. 16, pp. 21793-21800, 2008.

[38] T. W. Ebbesen, H. Lezec, H. Ghaemi, T. Thio, and P. Wolff, "Extraordinary optical transmission through sub-wavelength hole arrays," *Nature,* vol. 391, pp. 667-669, 1998.

[39] M. Lahav, A. Vaskevich, and I. Rubinstein, "Biological sensing using transmission surface plasmon resonance spectroscopy," *Langmuir,* vol. 20, pp. 7365-7367, 2004.

[40] Y. Wang, "Voltage-induced color-selective absorption with surface plasmons," *Applied Physics Letters,* vol. 67, pp. 2759-2761, 1995.

[41] S. Enoch, R. Quidant, and G. Badenes, "Optical sensing based on plasmon coupling in nanoparticle arrays," *Optics Express,* vol. 12, pp. 3422-3427, 2004.

[42] U. Kreibig and M. Vollmer, "Optical properties of metal clusters," 1995.

[43] J. M. Petroski, Z. L. Wang, T. C. Green, and M. A. El-Sayed, "Kinetically controlled growth and shape formation mechanism of platinum nanoparticles," *The Journal of Physical Chemistry B,* vol. 102, pp. 3316-3320, 1998.

[44] I. Romero, J. Aizpurua, G. W. Bryant, and F. J. García De Abajo, "Plasmons in nearly touching metallic nanoparticles: singular response in the limit of touching dimers," *Optics Express,* vol. 14, pp. 9988-9999, 2006.

[45] A. K. Azad and W. Zhang, "Resonant terahertz transmission in subwavelength metallic hole arrays of sub-skin-depth thickness," *Optics Letters,* vol. 30, pp. 2945-2947, 2005.

[46] H. Bethe, "Theory of diffraction by small holes," *Physical Review,* vol. 66, p. 163, 1944.

[47] P. B. Johnson and R.-W. Christy, "Optical constants of the noble metals," *Physical Review B,* vol. 6, p. 4370, 1972.

[48] H. Raether, *Surface plasmons on smooth surfaces*: Springer, 1988.

[49] E. Kretschmann and H. Raether, "Radiative decay of non radiative surface plasmons excited by light(Surface plasma waves excitation by light and decay into photons applied to nonradiative modes)," *Zeitschrift Fuer Naturforschung, Teil A,* vol. 23, p. 2135, 1968.

[50] A. Otto, "Excitation of nonradiative surface plasma waves in silver by the method of frustrated total reflection," *Zeitschrift für Physik,* vol. 216, pp. 398-410, 1968.

[51] D. Qu, D. Grischkowsky, and W. Zhang, "Terahertz transmission properties of thin, subwavelength metallic hole arrays," *Optics Letters,* vol. 29, pp. 896-898, 2004.

[52] M. Pelton, J. Aizpurua, and G. Bryant, "Metal-nanoparticle plasmonics," *Laser & Photonics Reviews,* vol. 2, pp. 136-159, 2008.

[53] P. A. Hobson, s. Wedge, j. A. Wasey, i. Sage, and w. L. Barnes, "Surface plasmon mediated emission from organic light-emitting diodes," A*dvanced Materials,* vol. 14, pp. 1393-1396, 2002.

[54] S. Kawata, Y. Inouye, and P. Verma, "Plasmonics for near-field nano-imaging and superlensing," *Nature Photonics,* vol. 3, pp. 388-394, 2009.

[55] S. Zhang, D. A. Genov, Y. Wang, M. Liu, and X. Zhang, "Plasmon-induced transparency in metamaterials," *Physical Review Letters,* vol. 101, p. 047401, 2008.

[56] J. Z. Zhang, "Biomedical applications of shape-controlled plasmonic nanostructures: a case study of hollow gold nanospheres for photothermal ablation therapy of cancer," *The Journal of Physical Chemistry Letters,* vol. 1, pp. 686-695, 2010.

[57] A. O. Govorov, H. Zhang, H. V. Demir, and Y. K. Gun'ko, "Photogeneration of hot plasmonic electrons with metal nanocrystals: Quantum description and potential applications," *Nano Today,* vol. 9, pp. 85-101, 2014.

[58] J. Hofmann and W. Steinmann, "Plasma resonance in the photoemission of silver," *physica status solidi (b),* vol. 30, pp. K53-K56, 1968.

[59] L. Marsal, I. Martin, J. Pallares, A. Orpella, and R. Alcubilla, "Annealing effects on the conduction mechanisms of p+-amorphous-Si0. 8C0. 2: H/n-crystalline-Si diodes," *Journal of Applied Physics,* vol. 94, pp. 2622-2626, 2003.

[60] J. Endriz and W. Spicer, "Surface-plasmon-one-electron decay and its observation in photoemission," *Physical Review Letters,* vol. 24, p. 64, 1970.

[61] R. H. Fowler, "The analysis of photoelectric sensitivity curves for clean metals at various temperatures," *Physical Review,* vol. 38, p. 45, 1931.

[62] S. M. Sze and M. K. Lee, *Semiconductor Devices: Physics and Technology*: Wiley, 2012.

[63] I. H. El-Sayed, X. Huang, and M. A. El-Sayed, "Surface plasmon resonance scattering and absorption of anti-EGFR antibody conjugated gold nanoparticles in cancer diagnostics: applications in oral cancer," *Nano Letters,* vol. 5, pp. 829-834, 2005.

[64] J. Zhang, H. Liu, Z. Wang, and N. Ming, "Shape-selective synthesis of gold nanoparticles with controlled sizes, shapes, and plasmon resonances," *Advanced Functional Materials,* vol. 17, pp. 3295-3303, 2007.

[65] M. W. Knight, Y. Wang, A. S. Urban, A. Sobhani, B. Y. Zheng, P. Nordlander*, et al.*, "Embedding plasmonic nanostructure diodes enhances hot electron emission," *Nano Letters,* vol. 13, pp. 1687-1692, 2013/04/10 2013.

[66] Y. Taur and T. H. Ning, *Fundamentals of modern VLSI devices* vol. 2: Cambridge University Press Cambridge, 1998.

[67] S. M. Sze and K. K. Ng, "Physics of semiconductor devices . Creator/Author, Sze, sm. Publication Date, 1981 Jan 01. OSTI Identifier, OSTI ID: 5381484," 1981.

[68] S. Link and M. A. El-Sayed, "Size and temperature dependence of the plasmon absorption of colloidal gold nanoparticles," *The Journal of Physical Chemistry B,* vol. 103, pp. 4212-4217, 1999/05/01 1999.

[69] H. Chen, X. Kou, Z. Yang, W. Ni, and J. Wang, "Shape- and size-dependent refractive index sensitivity of gold nanoparticles," *Langmuir,* vol. 24, pp. 5233-5237, 2008/05/01 2008.

[70] R. F. Pierret, "Semiconductor device fundamentals," 1996.

[71] G. Raschke, S. Kowarik, T. Franzl, C. Sönnichsen, T. A. Klar, J. Feldmann*, et al.*, "Biomolecular recognition based on single gold nanoparticle light scattering," *Nano Letters,* vol. 3, pp. 935-938, 2003/07/01 2003.

[72] H. Liao, C. L. Nehl, and J. H. Hafner, "Biomedical applications of plasmon resonant metal nanoparticles," *Nanomedicine (London, England),* vol. 1, pp. 201-208, 2006.

[73] K. A. Willets and R. P. Van Duyne, "Localized surface plasmon resonance spectroscopy and sensing," *Annual Review of Physical Chemistry,* vol. 58, pp. 267-297, 2007.

[74] F. Wang and N. A. Melosh, "Plasmonic energy collection through hot carrier extraction," *Nano Letters,* vol. 11, pp. 5426-5430, 2011.

[75] Mayer, Kathryn M., and Jason H. Hafner. "Localized surface plasmon resonance sensors." *Chemical Reviews* 111.6 (2011): 3828-3857.

[76] B. Razavi, Design of analog cmos integrated circuits. *McGraw-Hill:* 2001.

[77] S. M. Sze, *Semiconductor devices, physics and technology*: Wiley, 1985.

[78] J. C. Ranuárez, M. J. Deen, and C.-H. Chen, "A review of gate tunneling current in MOS devices," *Microelectronics Reliability,* vol. 46, pp. 1939-1956, 2006.

[79] Z. Li, R. Ye, R. Feng, Y. Kang, X. Zhu, J. M. Tour*, et al.*, "Graphene quantum dots doping of MoS2 monolayers," *Advanced Materials,* vol. 27, pp. 5235-5240, 2015.

[80] S. O. Kasap, *Principles of electronic materials and devices*: McGraw-Hill, 2006.

[81] R. Ballerstadt, C. Evans, R. McNichols, and A. Gowda, "Concanavalin A for in vivo glucose sensing: A biotoxicity review," *Biosens. Bioelectron.,* vol. 22, pp. 275-284, Aug 15 2006.

[82] T. B. H. Geijtenbeek and S. I. Gringhuis, "Signalling through C-type lectin receptors: shaping immune responses," *Nat. Rev. Immunol.,* vol. 9, pp. 465-479, Jul 2009.

[83] Y. van Kooyk and G. A. Rabinovich, "Protein-glycan interactions in the control of innate and adaptive immune responses," *Nat. Immunol.,* vol. 9, pp. 593-601, Jun 2008.

[84] J. J. Lundquist and E. J. Toone, "The cluster glycoside effect," *Chem. Rev.,* vol. 102, pp. 555-578, 2002.

[85] K. Godula and C. R. Bertozzi, "Synthesis of glycopolymers for microarray applications via ligation of reducing sugars to a poly (acryloyl hydrazide) scaffold," *J. Am. Chem. Soc.,* vol. 132, pp. 9963-9965, 2010.

[86] J. Q. Gao, D. J. Liu, and Z. X. Wang, "Microarray-based study of carbohydrate-protein binding by gold nanoparticle probes," *Anal. Chem.,* vol. 80, pp. 8822-8827, Nov 15 2008.

[87] W. P. Hall, S. N. Ngatia, and R. P. Van Duyne, "LSPR biosensor signal enhancement using nanoparticle-antibody conjugates," *J. Phys. Chem. C,* vol. 115, pp. 1410-1414, Feb 10 2011.

[88] A. Varki, R. D. Cummings, J. D. Esko, H. H. Freeze, P. Stanley, J. D. Marth*, et al.*, "Symbol nomenclature for glycan representation," *Proteomics,* vol. 9, pp. 5398-5399, 2009.

[89] K. Godula and C. R. Bertozzi, "Density variant glycan microarray for evaluating cross-linking of mucin-like glycoconjugates by lectins," *J. Am. Chem. Soc.,* vol. 134, pp. 15732-15742, Sep 26 2012.

[90] X. Han, Y. Zheng, C. J. Munro, Y. Ji, and A. B. Braunschweig, "Carbohydrate nanotechnology: hierarchical assembly using nature's other information carrying biopolymers," *Curr. Opin. Biotechnol.,* vol. 34, pp. 41-47, 2015.

[91] V. E. Ferry, L. A. Sweatlock, D. Pacifici, and H. A. Atwater, "Plasmonic Nanostructure design for efficient light coupling into solar cells," *Nano Lett.,* vol. 8, pp. 4391-4397, 2008/12/10 2008.

[92] R. A. Pala, J. White, E. Barnard, J. Liu, and M. L. Brongersma, "Design of plasmonic thin-film solar cells with broadband absorption enhancements," *Adv. Mater.,* vol. 21, pp. 3504-3509, 2009.

[93] A. V. Kabashin, P. Evans, S. Pastkovsky, W. Hendren, G. A. Wurtz, R. Atkinson*, et al.*, "Plasmonic nanorod metamaterials for biosensing," *Nat. Mater.,* vol. 8, pp. 867-871, 2009.

[94] S. Lal, S. Link, and N. J. Halas, "Nano-optics from sensing to waveguiding," *Nat. Photon.,* vol. 1, pp. 641-648, 2007.

[95] M. Svedendahl, S. Chen, A. Dmitriev, and M. Käll, "Refractometric sensing using propagating versus localized surface plasmons: a direct comparison," *Nano Lett.,* vol. 9, pp. 4428-4433, 2009/12/09 2009.

[96] X. Huang, I. H. El-Sayed, W. Qian, and M. A. El-Sayed, "Cancer cell imaging and photothermal therapy in the near-infrared region by using gold nanorods," *J. Am. Chem. Soc.,* vol. 128, pp. 2115-2120, 2006/02/01 2006.

[97] E. J. R. Vesseur, R. de Waele, M. Kuttge, and A. Polman, "Direct observation of plasmonic modes in au nanowires using high-resolution cathodoluminescence spectroscopy," *Nano Letters,* vol. 7, pp. 2843-2846, 2007/09/01 2007.

[98] H. M. Kim, S. M. Jin, S. K. Lee, M.-G. Kim, and Y.-B. Shin, "Detection of biomolecular binding through enhancement of localized surface plasmon resonance (lspr) by gold nanoparticles," *Sensors,* vol. 9, pp. 2334-2344, 2009.

[99] W.-S. Liao, X. Chen, T. Yang, E. Castellana, J. Chen, and P. Cremer, "Benchtop chemistry for the rapid prototyping of label-free biosensors: Transmission localized surface plasmon resonance platforms," *Biointerphases,* vol. 4, pp. 80-85, 2009/12/01 2009.

[100] S. M. Marinakos, S. Chen, and A. Chilkoti, "Plasmonic detection of a model analyte in serum by a gold nanorod sensor," *Anal. Chem.,* vol. 79, pp. 5278-5283, 2007/07/01 2007.

[101] J. McPhillips, A. Murphy, M. P. Jonsson, W. R. Hendren, R. Atkinson, F. Höök*, et al.*, "High-performance biosensing using arrays of plasmonic nanotubes," *ACS Nano,* vol. 4, pp. 2210-2216, 2010/04/27 2010.

[102] Y. Wang, W. Qian, Y. Tan, and S. Ding, "A label-free biosensor based on gold nanoshell monolayers for monitoring biomolecular interactions in diluted whole blood," *Biosens. Bioelectron.,* vol. 23, pp. 1166-1170, 2008.

[103] K. Fujiwara, H. Watarai, H. Itoh, E. Nakahama, and N. Ogawa, "Measurement of antibody binding to protein immobilized on gold nanoparticles by localized surface plasmon spectroscopy," *Anal. Bional. Chem.,* vol. 386, pp. 639-644, 2006.

[104] A. Das, J. Zhao, G. C. Schatz, S. G. Sligar, and R. P. Van Duyne, "Screening of type i and ii drug binding to human cytochrome p450-3a4 in nanodiscs by localized surface plasmon resonance spectroscopy," *Anal. Chem.,* vol. 81, pp. 3754-3759, 2009/05/15 2009.

[105] W. J. Galush, S. A. Shelby, M. J. Mulvihill, A. Tao, P. Yang, and J. T. Groves, "A nanocube plasmonic sensor for molecular binding on membrane surfaces," *Nano Lett.,* vol. 9, pp. 2077-2082, 2009/05/13 2009.

[106] A. J. Haes, L. Chang, W. L. Klein, and R. P. Van Duyne, "Detection of a biomarker for alzheimer's disease from synthetic and clinical samples using a nanoscale optical biosensor," *J. Am. Chem. Soc.,* vol. 127, pp. 2264-2271, 2005/02/01 2005.

[107] A. J. Haes, S. Zou, J. Zhao, G. C. Schatz, and R. P. Van Duyne, "Localized surface plasmon resonance spectroscopy near molecular resonances," *J. Am. Chem. Soc.,* vol. 128, pp. 10905-10914, 2006/08/01 2006.

[108] C. Li, C. Wu, J. Zheng, J. Lai, C. Zhang, and Y. Zhao, "LSPR sensing of molecular biothiols based on noncoupled gold nanorods," *Langmuir,* vol. 26, pp. 9130-9135, 2010/06/01 2010.

[109] T.-J. Lin, K.-T. Huang, and C.-Y. Liu, "Determination of organophosphorous pesticides by a novel biosensor based on localized surface plasmon resonance," *Biosens. Bioelectron.,* vol. 22, pp. 513-518, 2006.

[110] S. Morokoshi, K. Ohhori, K. Mizukami, and H. Kitano, "Sensing capabilities of colloidal gold modified with a self-assembled monolayer of a glucose-carrying polymer chain on a glass substrate," *Langmuir,* vol. 20, pp. 8897-8902, 2004/09/01 2004.

[111] S. Y. Yoo, D.-K. Kim, T. J. Park, E. K. Kim, E. Tamiya, and S. Y. Lee, "Detection of the most common corneal dystrophies caused by bigh3 gene point mutations using a multispot gold-capped nanoparticle array chip," *Anal. Chem.,* vol. 82, pp. 1349-1357, 2010/02/15 2010.

[112] J. Zhao, A. Das, G. C. Schatz, S. G. Sligar, and R. P. Van Duyne, "Resonance localized surface plasmon spectroscopy: sensing substrate and inhibitor binding to cytochrome p450," *J. Phys. Chem. C,* vol. 112, pp. 13084-13088, 2008/08/01 2008.

[113] P. Englebienne, "Use of colloidal gold surface plasmon resonance peak shift to infer affinity constants from the interactions between protein antigens and antibodies specific for single or multiple epitopes," *Analyst,* vol. 123, pp. 1599-1603, 1998.

[114] S. Lee, K. M. Mayer, and J. H. Hafner, "Improved localized surface plasmon resonance immunoassay with gold bipyramid substrates," *Anal. Chem.,* vol. 81, pp. 4450-4455, 2009/06/01 2009.

[115] K. M. Mayer, S. Lee, H. Liao, B. C. Rostro, A. Fuentes, P. T. Scully*, et al.*, "A label-free immunoassay based upon localized surface plasmon resonance of gold nanorods," *ACS Nano,* vol. 2, pp. 687-692, 2008/04/01 2008.

[116] S. Szunerits, J. Niedziółka-Jönsson, R. Boukherroub, P. Woisel, J.-S. b. Baumann, and A. Siriwardena, "Label-free detection of lectins on carbohydrate-modified boron-doped diamond surfaces," *Anal. Chem.,* vol. 82, pp. 8203-8210, 2010.

[117] H. Shokri Kojori, J.-H. Yun, Y. Paik, J. Kim, W. A. Anderson, and S. J. Kim, "Plasmon field effect transistor for plasmon to electric conversion and amplification," *Nano Letters,* vol. 16, pp. 250-254, 2016/01/13 2016.

[118] S. D. Bian, S. B. Zieba, W. Morris, X. Han, D. C. Richter, K. A. Brown*, et al.*, "Beam pen lithography as a new tool for spatially controlled photochemistry, and its utilization in the synthesis of multivalent glycan arrays," *Chem. Sci.,* vol. 5, pp. 2023-2030, 2014.

[119] Y. K. Lee, C. H. Jung, J. Park, H. Seo, G. A. Somorjai, and J. Y. Park, "Surface plasmon-driven hot electron flow probed with metal-semiconductor nanodiodes," *Nano Lett.,* vol. 11, pp. 4251-4255, 2011.

[120] P. H. Liang, S. K. Wang, and C. H. Wong, "Quantitative analysis of carbohydrate-protein interactions using glycan microarrays: determination of surface and solution dissociation constants," *JACS,* vol. 129, pp. 11177-84, Sep 12 2007.

[121] D. A. Mann, M. Kanai, D. J. Maly, and L. L. Kiessling, "Probing low affinity and multivalent interactions with surface plasmon resonance: ligands for concanavalin A," *J. Am. Chem. Soc.,* vol. 120, pp. 10575-10582, 1998.

[122] Y. Zhang, Q. Li, L. G. Rodriguez, and J. C. Gildersleeve, "An array-based method to identify multivalent inhibitors," *J. Am. Chem. Soc.,* vol. 132, pp. 9653-9662, 2010.

[123] J. N. Anker, W. P. Hall, O. Lyandres, N. C. Shah, J. Zhao, and R. P. Van Duyne, "Biosensing with plasmonic nanosensors," *Nat. Mater.,* vol. 7, pp. 442-453, 06//print 2008.

[124] H. J. Gabius, H. C. Siebert, S. Andre, J. Jimenez-Barbero, and H. Rudiger, "Chemical biology of the sugar code," *ChemBioChem,* vol. 5, pp. 740-764, Jun 7 2004.

[125] F. P. Schwarz, K. D. Puri, R. Bhat, and A. Surolia, "Thermodynamics of monosaccharide binding to concanavalin A, pea (Pisum sativum) lectin, and lentil (Lens culinaris) lectin," *J. Biol. Chem.,* vol. 268, pp. 7668-7677, 1993.

[126] A. J. Haes and R. P. Van Duyne, "A nanoscale optical biosensor: sensitivity and selectivity of an approach based on the localized surface plasmon resonance spectroscopy of triangular silver nanoparticles," *J. Am. Chem. Soc.,* vol. 124, pp. 10596-10604, 2002.

[127] J. C. Riboh, A. J. Haes, A. D. McFarland, C. R. Yonzon, and R. P. Van Duyne, "A nanoscale optical biosensor: Real-time immunoassay in physiological buffer enabled by improved nanoparticle adhesion," *J. Phys. Chem. B,* vol. 107, pp. 1772-1780, Feb 27 2003.

[128] H. M. Branderhorst, R. Ruijtenbeek, R. M. Liskamp, and R. J. Pieters, "Multivalent carbohydrate recognition on a glycodendrimer-functionalized flow-through chip," *ChemBioChem,* vol. 9, pp. 1836-1844, 2008.

[129] O. Oyelaran, Q. Li, D. Farnsworth, and J. C. Gildersleeve, "Microarrays with varying carbohydrate density reveal distinct subpopulations of serum antibodies," *J. Proteome Res.,* vol. 8, pp. 3529-3538, 2009.

[130] E. Duverger, N. Frison, A.-C. Roche, and M. Monsigny, "Carbohydrate-lectin interactions assessed by surface plasmon resonance," *Biochimie,* vol. 85, pp. 167-179, 2003.

[131] Y. Shinohara, H. Sota, F. Kim, M. Shimizu, M. Gotoh, M. Tosu*, et al.*, "Use of a biosensor based on surface plasmon resonance and biotinyl glycans for analysis of sugar binding specificities of lectins," *J. Biochem.,* vol. 117, pp. 1076-1082, 1995.

[132] M. Ambrosi, N. R. Cameron, and B. G. Davis, "Lectins: tools for the molecular understanding of the glycocode," *Org. Biomol. Chem.,* vol. 3, pp. 1593-1608, 2005.

[133] F. P. Schwarz, K. D. Puri, R. G. Bhat, and A. Surolia, "Thermodynamics of monosaccharide binding to concanavalin-a, pea (pisum-sativum) lectin, and lentil (lens-culinaris) lectin," *J. Biol. Chem.,* vol. 268, pp. 7668-7677, Apr 15 1993.

[134] T. K. Dam, R. Roy, D. Pagé, and C. F. Brewer, "Negative cooperativity associated with binding of multivalent carbohydrates to lectins. Thermodynamic analysis of the “multivalency effect”," *Biochemistry,* vol. 41, pp. 1351-1358, 2002.

[135] T. K. Dam, T. A. Gerken, B. S. Cavada, K. S. Nascimento, T. R. Moura, and C. F. Brewer, "Binding studies of α-GalNAc-specific lectins to the α-GalNAc (Tn-antigen) form of porcine submaxillary mucin and its smaller fragments," *J. Biol. Chem.,* vol. 282, pp. 28256-28263, 2007.

[136] S. M. Marinakos, S. Chen, and A. Chilkoti, "Plasmonic detection of a model analyte in serum by a gold nanorod sensor," *Analytical Chemistry,* vol. 79, pp. 5278-5283, 2007/07/01 2007.

[137] C. Wendeln, A. Heile, H. F. Arlinghaus, and B. J. Ravoo, "Carbohydrate microarrays by microcontact printing," *Langmuir,* vol. 26, pp. 4933-4940, 2010.

[138] C. R. Yonzon, X. Zhang, and R. P. Van Duyne, "Localized surface plasmon resonance immunoassay and verification using surface-enhanced Raman spectroscopy," in *Optical Science and Technology, SPIE's 48th Annual Meeting*, 2003, pp. 78-85.

[139] N. Nath and A. Chilkoti, "A colorimetric gold nanoparticle sensor to interrogate biomolecular interactions in real time on a surface," *Analytical Chemistry,* vol. 74, pp. 504-509, 2002.

[140] A. Schenk and G. Heiser, "Modeling and simulation of tunneling through ultra-thin gate dielectrics," *Journal of Applied Physics,* vol. 81, pp. 7900-7908, 1997.

[141] B. Sepúlveda, P. C. Angelomé, L. M. Lechuga, and L. M. Liz-Marzán, "LSPR-based nanobiosensors," *Nano Today,* vol. 4, pp. 244-251, 2009.